APPLICATION OF MULTIFREQUENCY ELECTRON SPIN RESONANCE SPECTROSCOPY TO STUDY DYNAMICS OF T4 LYSOZYME

A Dissertation

Presented to the Faculty of the Graduate School

of Cornell University

in Partial Fulfillment of the Requirements for the Degree of

Doctor of Philosophy

by

Ziwei Zhang

May 2010

APPLICATION OF MULTIFREQUENCY ELECTRON SPIN RESONANCE SPECTROSCOPY TO STUDY DYNAMICS OF T4 LYSOZYME

Ziwei Zhang, Ph.D.

Cornell University 2010

An extensive set of ESR spectra was obtained over a wide range of frequencies (9, 95, 170 and 240 GHz) and temperatures (2 to 32^{o}C) to explore the dynamic modes of nitroxide-labeled T4 lysozyme in solution. A commonly used nitroxide side chain (R1), or a methylated analogue with hindered internal motion (R2), was substituted for the native side chain at solvent-exposed helical sites, 72 or 131. The spectra at all four frequencies were simultaneously fit with the slowly relaxing local structure (SRLS) model. Good fits were achieved at all the temperatures. Two principle dynamic modes are included in the SRLS model: the global tumbling of the protein and the internal motion consisting of backbone fluctuations and side chain isomerizations. Three distinct spectral components were required for R1 and two for R2 to account for the spectra at all temperatures. One is a highly ordered and slow motional component, which is observed in the spectra of both R1 and R2; it may correspond to conformers stabilized by interaction with the protein surface. The fraction of this component decreases with increasing temperature, and is more populated in the R2 spectra, possibly arising from stronger interaction of the nitroxide ring with the protein surface due to the additional methyl group. The other two components of R1 and the second component of R2, are characterized by fast anisotropic diffusion and relatively low ordering, most likely corresponding to conformers having little or no interactions with nearby residues. Comparison of the motion of R1 and R2 at sites 72 and 131 makes it unclear whether backbone dynamics or differences in side chain internal motion is the major contribution to the spectral differences at these sites. Ficoll of different

concentrations was added to increase the solution viscosity, thereby slowing down the global tumbling of the protein. A significant effect of Ficoll on the internal motion of an immobilized component was apparent in R2 but not in R1. The ability of such multifrequency studies to separate the effects of faster internal modes of motion from slower overall motions is clearly demonstrated, and its utility in future studies is considered.

BIOGRAPHICAL SKETCH

Ziwei Zhang was born on May 18, 1980 in the city of Changchun, the capital of Jilin Province, located in the northeast portion of China. She was the only child of the family. 1986-1992 she attended the Primary School attached to Jilin University, 1992-1995 the Middle School attached to Jilin University, and 1995-1998 the High School attached to Northeast Normal University. In 1998, she started her undergraduate study in the College of Life Science at Jilin University, majoring in Biochemistry. She received a Bachelor of Science degree in 2002. For bachelor dissertation, she worked with Prof. Yongge Wu in the College of Life Science at Jilin University on his study of two mutants of human pyruvate dehydrogenase (PDH). 2002-2003 she worked as a part-time assistant editor for a high school journal in Changchun publishing house as well as worked with Prof. Honggui Zhang in the College of Pharmaceutical Science at Jilin University on his study of the effective constituents from Chinese herbal medicine. In 2003, she began her graduate study in the Department of Molecular Biology and Genetics at Cornell University, majoring in Biophysics. After the first-year rotations, she joined Prof. Jack Freed's lab to study the dynamics of T4 lysozyme by multifrequency ESR. After completion of Ph.D. degree, she will continue to work with Prof. Freed as a postdoctoral fellow on the multifrequency ESR study of protein dynamics.

To My Mother and My Grandma

ACKNOWLEDGEMENTS

I would like to sincerely thank my advisor, Dr. Jack Freed, for his guidance, patience, and support during my graduate studies. He is the most intelligent person I have ever known. He gave me the most important advice when I was in need of help, as well as encouraged me to think independently. I would also like to thank my committee members, Dr. Linda Nicholson and Dr. Robert Oswald, for their guidance, precious advice, and assistance in my research.

I would like to express my deep gratitude to Dr. Dmitriy Tipikin, Keith Earle, Zhichun Liang, and Jozef Moscicki, who put their valuable efforts in this project. I also thank our collaborators from UCLA, Dr. Wayne Hubbell and Mark Fleissner, for their assistance and discussions.

I thank Dr. Wulf Hofbauer, Mingtao Ge, Yun-Wei Chiang, Boris Dzikovski, Jaya Bhatnagar, and Petr Borbat for their professional assistance in experiments, instruments and simulations. I thank Curt Dunnam for his help with the 95-GHz spectrometer, as well as Joanne Trutko for her help in editing the manuscript.

I thank Dr. Gerald Feigenson for his help as the director of graduate studies in the field of biophysics. I thank Dr. Andrew Smith, Chang Shin, Elka Georgieva, and Aritro Sinharoy for their help and friendship.

I would like to thank my family especially my mother and grandma as they pray for me everyday during these years.

TABLE OF CONTENTS

LIST OF TABLES

LIST OF FIGURES

CHAPTER 1

INTRODUCTION

1.1 ELECTRON SPIN RESONANCE (ESR) SPECTROSCOPY AND PROTEIN DYNAMICS

Proteins have been recognized to be dynamic, not static, molecules. There are a variety of motions with different amplitude and time scales within a protein molecule. The dynamics of proteins are important to their functions. To explore and characterize the dynamics of proteins is crucial for understanding the relation between dynamics and function.

Electron spin resonance (ESR) spectroscopy, as a sensitive technique to probe molecules containing unpaired electrons, has been widely used in the study of protein dynamics (1, 2, 3, 4, 5, 6, 7). Most protein molecules do not have unpaired electrons. Therefore, so far, most studies on protein dynamics using ESR spectroscopy are coupled with the site-directed spin labeling (SDSL) technique, with which the site or sites of interest can be labeled with the free radical where the unpaired electron is localized. The nitroxide group is usually selected as the spin label to label proteins. Detailed information regarding the motion of the spin labeled protein can be obtained by spectral simulation (8, 9).

1.2 MOTIONS WITHIN THE PROTEIN MOLECULE STUDIED BY ESR SPECTROSCOPY

The motion of the spin label is considered to be influenced by its interaction

with its surrounding atoms. Therefore, the mobility of the spin label is supposed to be site specific, resulting in a relationship between the dynamics of spin labels at various sites and the structure and function of the protein. Some examples of ESR studies on protein dynamics at different time scales, which include side chain motions, backbone fluctuations, loop motions, domain motions, coil-helix transition, folding/unfolding transition, and the global tumbling, were published (10, 11, 12, 13, 14, 15, 16, 17, 18). Many of them are related to water soluble proteins (19).

In this dissertation, we are most interested in the motions of side chains, backbone fluctuations, and the global tumbling. The motions of side chains in the α-helix of T4 lysozyme (T4L), in the β-sheet of T4L as well as annexin 12, and in the loop region of cellular retinol-biding protein (CRBP) were studied by Hubbell and coworkers at specific amino acid sites substituted with spin labeled cysteines. The motion of the side chain is mainly affected by the motion of its backbone and the motion of its tether, which is constrained by the interaction between this side chain and other amino acid residues surrounding it. When there is no interaction between the side chain exposed to the solvent in an α-helix and residues in the same helix but belonging to different turns, the motion of the tether is same at residues in different helices. Thus, the motion of the side chain can represent the motion of its backbone. If this were the case, ESR spectroscopy together with the SDSL technique may be very useful for mapping backbone dynamics in protein. However, our results in this work show that the motion of the backbone may not be the only contribution to the different mobility of side chains at two solvent exposed sites in different helices.

The main challenge in the study of protein dynamics is to decompose various dynamic modes in a protein. For proteins with molecular weight larger than 50 kD, the global tumbling is too slow to contribute to the X-band ESR spectra (10). For smaller proteins, such as T4 lysozyme (T4L) with the molecular weight of $\sim$ 19 kD, the effect

of the global tumbling can be reduced either by recording spectra in solution with viscogen (e.g. in sucrose solution) or collecting data on high frequency ESR spectrometers. Thus, the effects of backbone fluctuations and the conformational transitions within the side chain can be determined from the ESR spectra. Once the internal motion is determined, the global tumbling can be obtained from the conventional X-band spectra (i.e. ~ 9 GHz) in water solution.

1.3 A COMPARISON OF VIRTUES OF ESR AND NMR METHODS

Nuclear magnetic resonance (NMR) spectroscopy is another widely used technique to study the dynamics of proteins (20, 21, 22). Compared to NMR spectroscopy, the virtues of ESR spectroscopy are: (1) ESR is much more sensitive per spin; (2) ESR's time scale is nanoseconds (NMR's is micro- to milliseconds for chemical exchange, i.e. the sampling of different chemical environments by a spin); (3) The spin-label spectrum is simple, and can focus on a limited number of spins; (4) ESR spectra change dramatically as the tumbling motion of the probe slows, thereby providing great sensitivity to local "fluidity" (in NMR nearly complete averaging occurs, so only residual rotational effects are observed by T1 and T2) (4).

At present, the applications of NMR methods to study the structure and dynamics of membrane proteins, high molecular weight proteins in solution, and protein intermediate states are more problematic. ESR has been successfully applied to approach these problems and characterize the structure and dynamics of both soluble and membrane proteins of arbitrary molecular weight (1, 7, 10, 16).

1.4 VIRTUES FOR MULTIFREQUENCY ESR METHOD

1.4.1 Sensitivity to Motions at Different Time Scales

Protein motions over the 10^{-6} to 10^{-12} s time scales can be investigated by continuous-wave ESR spectroscopy at various frequencies (23, 24, 25). ESR spectra at different microwave frequencies are sensitive to motions at different time scales. ESR at lower frequencies is more sensitive to the slower motions, whereas ESR at higher frequencies is more sensitive to the faster motions (26). For example, the slower motions, easily observed in the low frequency ESR spectra, may be frozen at the high frequency time scale. On the other hand, the faster motions, completely averaged out in the low frequency ESR spectra, can be well resolved at the high frequency time scale. Therefore, the combination of ESR spectroscopy at a series of frequencies enables one to decompose various motional modes in a protein according to their time scales (26). Until now, ESR at only two frequencies has been used to study the dynamics of proteins (6, 17, 27, 28, 29, 30, 31, 32).

1.4.2 Sensitivity to *g* and *A* Tensors

Another virtue of the multifrequency ESR approach is the ability to determine accurately the principal values of the magnetic tensors (the hyperfine $\boldsymbol{A}$ tensor and $\boldsymbol{g}$ tensor) from the rigid limit spectra (33). With conventional ESR spectroscopy, only single crystal studies give accurate values for these parameters. Compared to the single crystal method, by means of the high frequency method, the magnetic tensors are determined when the protein is in its real environment (i.e. in aqueous solution). Also, it is much easier to perform the experiments since: (1) a crystal sample is not necessary; (2) With the single crystal method, many ESR spectra have to be collected by rotating the crystal around three orthogonal axes arbitrarily fixed on the crystal. High frequency ESR has a better $\boldsymbol{g}$ tensor resolution than ESR at lower frequencies

(see Figure 1-1), because the electron Zeeman interaction term becomes dominant in the Hamiltonian at very high frequencies; while ***A*** tensor components can be more precisely measured from ESR spectra at low or conventional frequency (~ 9 GHz).

1.4.3 Better Orientational Resolution

In addition, high frequency (i.e. high field) ESR has a better orientational resolution so that one can discern more clearly about which axis the motion occurs (4, 25). As shown in Figure 1-1, which is the powder spectrum of ESR where the samples are randomly distributed in different orientations, the regions corresponding to rotational diffusion around axes parallel to the *x*-axis, *y*-axis, and *z*-axis of the ***g*** tensor are well separated in the high frequency (i.e. 250 GHz) spectrum due to the dominance of the ***g*** tensor. Thus, the principal values for the rotational diffusion tensor corresponding to its principal axes can be determined by simulating the high frequency spectrum.

1.4.4 Development of More Sophisticated Dynamic Models

The use of the slowly relaxing local structure (SRLS) model was stimulated by the presence of multifrequency experimental data. The more extensive experimental spectra for the same sample collected at various frequencies can supply enough data for the more sophisticated models for the protein dynamics so that more dynamic modes can be separated.

1.5 SITE-DIRECTED SPIN LABELING (SDSL) TECHNIQUE

For ESR spectroscopy, a nitroxide spin label is covalently attached to the protein by site-directed spin labeling (SDSL) (1). In SDSL, a cysteine residue is

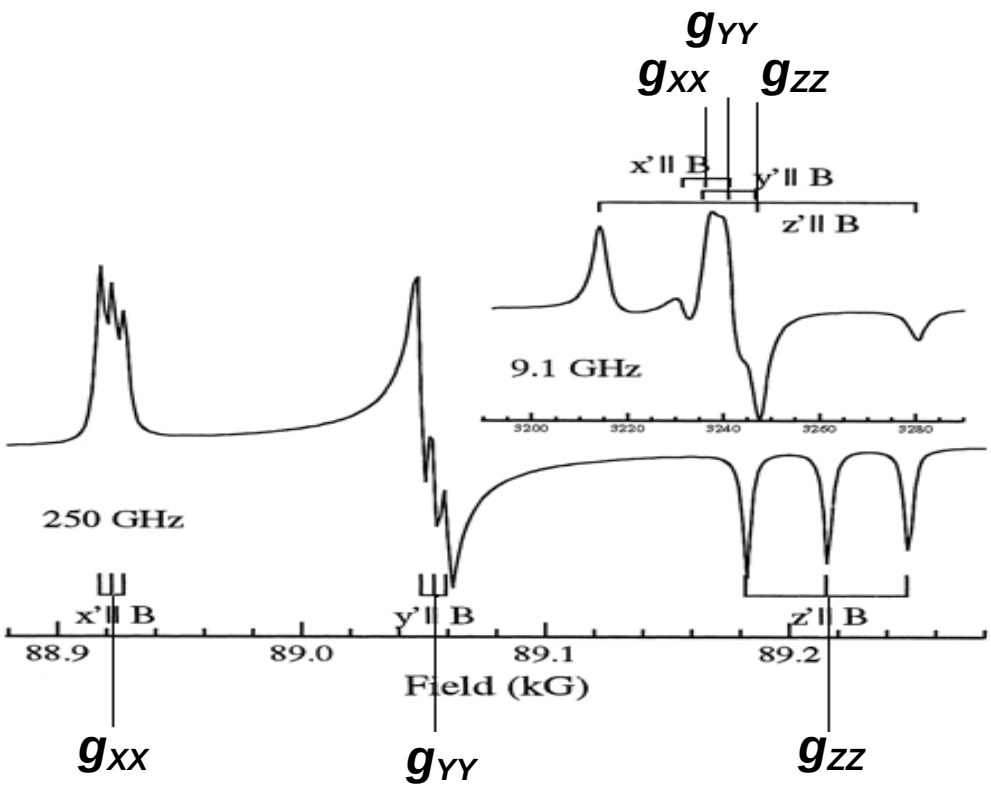

Figure 1-1. (cf. Biophysical Journal, Volume 75, Page 2538) Comparison of two powder ESR spectra (9 and 250 GHz) showing the better orientational resolution in the high frequency spectrum (250 GHz).

introduced at the site of interest by site-directed mutagenesis and modified with a nitroxide reagent to generate the spin labeled side chain (see Figure 1-2A) (10). The most commonly used nitroxide side chain is R1 (MTSSL), which structure is shown in Figure 1-2B (34).

For a spin labeled protein, the global motion of the spin label can be decomposed into the overall tumbling of the protein, backbone fluctuations, and the conformational transitions of the spin labeled side chain. More rigid or less mobile spin labels such as 4-derivative-R1 were produced to better understand the backbone dynamics since the motion of backbone is slower compared to the diffusion of R1 labeled side chain. The modified R1 will reduce the mobility of side chain and make backbone fluctuations dominant and better distinguished.

It has been shown that the incorporation of the spin label generally does not perturb the structure or the function of the protein. At solvent exposed sites, amino acid substitution has little effect on the stability and structure of the protein; while at buried sites, only the hydrophobic core is repacked and the backbone level fold is still mostly preserved (9, 10, 35).

Most spin labels used so far are nitroxide radicals because of its stability, flexibility, and sensitivity to its local environment (36). The chemistry and molecular structures of the nitroxide spin labels can be found in Chapter 5 and 6 of the "Spin Labeling" book (36).

Besides R1, other derivatives of R1 were also synthesized to modify one of the dynamic modes. For example, the 4-derivatives of R1 have been proved to constrain the isomerizations around the last two bonds (χ_4 and χ_5; see Figure 1-2B). Even more rigid spin label, e.g. TOAC, was also constructed to make other modes such as the backbone fluctuations even more pronounced. In this dissertation, we also work with R2 (4-methyl-MTSSL; see Figure 1-2B) besides R1.

A.

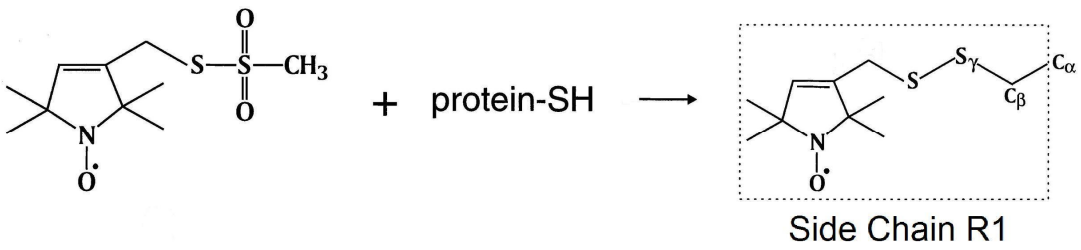

B.

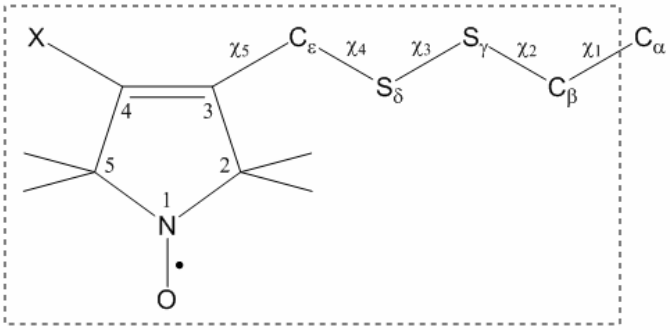

Side Chain R1 (R2)

X = H for R1 (MTSSL)

X = CH_3 for R2 (4-methyl-MTSSL)

Figure 1-2. The site-directed spin labeling (SDSL) technique.

1.6 χ_4 / χ_5 MODEL

As seen in Figure 1-2B, the rotations about χ_1 and χ_2 are constrained by the interaction between the disulfide bond and C_α. The energy potential for the conformational transition about χ_3 is too high so that the rotation about χ_3 is too slow for ESR time scale (10, 34, 35). Thus, the last two bonds χ_4 and χ_5 are the major contributions to the ESR spectral lineshape. This so called χ_4 / χ_5 model has been shown by X-ray crystallography, simulation of the X-band ESR spectra, as well as the modulation of R1 to other spin labels (10, 34, 35).

The rotation about χ_4 is relatively unconstrained but rotation about χ_5 is restricted by the steric clash of the disulfide bond with the ring of R1 or its derivatives (35). Such restriction for rotation about χ_5 is the basis for the ordered motion of the spin label. This allows for the simulation of the experimental data with either the MOMD or SRLS model, which will be introduced in the following two sections (37).

1.7 THE SLOWLY RELAXING LOCAL STRUCTURE (SRLS) MODEL

1.7.1 Theoretical Background

The slowly relaxing local structure (SRLS) model, in conjunction with the stochastic Liouville equation (SLE), was developed to decompose the global tumbling of the protein, and the internal motion consisting of backbone fluctuations and side chain isomerizations (26, 38). In this model, the reorientation of the spin label is restricted by its local environment which relaxes on a longer time scale (26, 39). ESR spectra recorded at a series of frequencies are fit simultaneously using the SRLS model with a common set of dynamic and ordering parameters, yielding a large number of fitting parameters including the rotational diffusion tensor for the global

tumbling ($\boldsymbol{R}^{\mathbf{c}}$), the rotational diffusion tensor for the internal motion ($\boldsymbol{R}^{\mathbf{o}}$), as well as the order parameters (S_{20} and S_{22}) for the internal motion. The multifrequency approach supplies adequate experimental data for reliably determining these fitting parameters.

In a spin labeled protein, for example, T4 lysozyme in water, both the internal motion of the spin labeled side chain and the global motion of the protein as a whole can be detected by ESR spectroscopy. For T4 lysozyme in water at room temperature, the global rotational diffusion rate of the lysozyme is about 10^7 s^{-1}, which is in the slow motional regime of X-band (9.3~9.4 GHz) spectrometer but in the rigid limit regime of 250 GHz spectrometer (6, 28). For the internal motion of T4 lysozyme at room temperature, the fast motion mode has a diffusion rate of about $5*10^8$ s^{-1}, which is almost in the slow motional regime of X-band spectrometer and deep in the slow motional regime of 250 GHz spectrometer. Therefore, the global motion of a small protein like T4 lysozyme should be included in the dynamical model for spectrum simulation. The SRLS model is for this purpose. In this model, the motion of the spin label is separated into two parts, the internal motion and the global motion. Both parts have their own diffusion rates, represented respectively by $\boldsymbol{R}^{\mathbf{o}}$ (internal) and $\boldsymbol{R}^{\mathbf{c}}$ (global). All the reference frames related to this model are shown in Figure 1-3 (12, 26). The *z*-axis of the laboratory frame is parallel to the applied magnetic field. The cage frame has the principle axes of the protein molecule as its axes. The global motion can be anisotropic (for example, $\boldsymbol{R}^{\mathbf{c}}$ can be axially symmetric), depending on the molecular shape and the symmetry of the protein. For a protein in water, there is no orienting potential for the global motion, therefore, the global director frame is neglected in this model. The internal director frame has one of its axes parallel to the direction of the equilibrium orienting potential for the internal motion. The internal

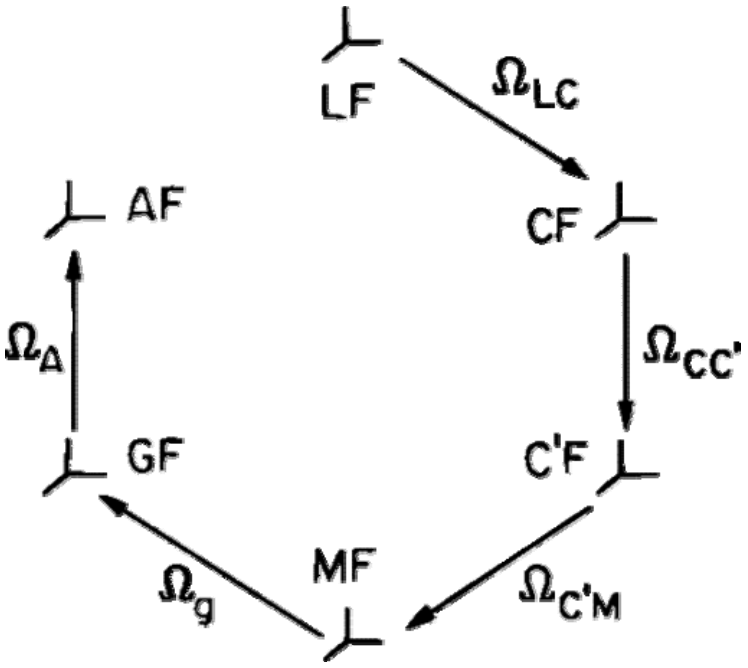

LF = Laboratory Frame,

CF = Cage Frame,

C'F = Internal Director Frame,

MF = Internal Diffusion Frame,

GF = ***g*** Tensor Frame,

AF = ***A*** Tensor Frame.

Figure 1-3. (i.e. Figure 3 in Reference 26) Reference frames for the SRLS model.

diffusion frame has the principal axes of the internal side chain motion as its axes. The ***g*** tensor frame and ***A*** tensor frame have their axes parallel respectively to the principal axes of these two magnetic tensors, which are related to the symmetry of the nitroxide group. Usually, these two magnetic tensor frames are set to be identical since for most nitroxide spin labels, the three principal axes of the ***g*** tensor and the ***A*** tensor coincide (40, 41). In Figure 1-3, Ω_{AB} represent the Euler angles that transform frame A to frame B. $\Omega_{CC'}$, Ω_A and Ω_{MG} (i.e. Ω_g in Figure 1-3) are time-independent, while Ω_{LC} and $\Omega_{C'M}$ are time-dependent. The stochastic Liouville equation (SLE)

$$\partial\rho(\Omega, t) / \partial t = [\, -i\hat{H}(\Omega) + \Gamma_\Omega \,]\, \rho(\Omega, t)$$

is applied with the SRLS model to simulate spectra. In this equation, $\rho(\Omega, t)$ is the combined orientational distribution function and the spin density matrix operator. The spin Hamiltonian $\hat{H}(\Omega)$ is

$$\hat{H}_{\mathrm{SRLS}} = \sum_{\mu=g,A} \sum_{l=0,2} \sum_{m=-l}^{l} \sum_{m'=-l}^{l} \sum_{m''=-l}^{l} \sum_{m'''=-l}^{l} \sum_{m''''=-l}^{l} \hat{A}^{(l,m)}_{\mu,L}$$
$$\mathscr{D}^{l}_{mm'}(\Omega_{LC})\mathscr{D}^{l}_{m'm''}(\Omega_{CC'})\mathscr{D}^{l}_{m''m'''}(\Omega_{C'M})\mathscr{D}^{l}_{m'''m''''}(\Omega_{MG})F^{(l,m'''')*}_{\mu,G}$$

The diffusion operator Γ_Ω is

$$\hat{\Gamma}_{\mathrm{SRLS}} = \hat{\Gamma}^{\mathrm{o}}(\Omega_{LM}) + \hat{\Gamma}^{\mathrm{c}}(\Omega_{LC}) + F^{\mathrm{o}}(-\Omega_{C'M}) + F^{\mathrm{c}}(-\Omega_{C'M})$$

In this diffusion operator equation, the first two terms on the right are from the rotation when there is no orienting potential for both the internal and global motions. The other two terms are related to the orienting potential for the internal motion and $\Omega_{C'M}$ are the Euler angles between the internal diffusion frame and the internal director

frame. Brownian diffusion is assumed as the diffusion model for both internal and global motions in this SRLS model. If the protein molecule can be regarded as an approximate sphere, then

$$\hat{\Gamma}^{c}(\Omega_{LC}) = R^{c}\hat{\mathbf{J}}^{c2}$$

.

If the protein is rod-like and has axial symmetry,

$$\hat{\Gamma}^{\text{global}}(\Omega_{LC}) = R_{\perp}^{c}\hat{\mathbf{J}}^{c2} + (R_{\parallel}^{c} - R_{\perp}^{c})\hat{\mathbf{J}}_{z}^{c2}$$

,

where $R_{\perp}^{c}$ and $R_{\parallel}^{c}$ are the rates for diffusion respectively perpendicular and around the uniaxial symmetry axis of the rod-like protein molecule. Similarly, if the internal motion is anisotropic but axially symmetric,

$$\hat{\Gamma}^{o}(\Omega_{LM}) = R_{\perp}^{o}\,\hat{\mathbf{J}}^{o2} + (R_{\parallel}^{o} - R_{\perp}^{o})\hat{\mathbf{J}}_{z}^{o2}$$

.

Here, $R_{\perp}^{o}$ and $R_{\parallel}^{o}$ are diffusion rates for diffusion perpendicular and around the symmetry axis for the internal motion. The dimensionless orienting potential for the internal motion $u(\Omega_{C'M})$ satisfies

$$-u(\Omega_{C'M}) \equiv -U(\Omega_{C'M})/k_{b}T = c_{20}\mathscr{D}_{00}^{2}(\Omega_{C'M}) + c_{22}[\mathscr{D}_{02}^{2}(\Omega_{C'M}) + \mathscr{D}_{0-2}^{2}(\Omega_{C'M})]$$

,

in which $U(\Omega_{C'M})$ is the orienting potential. Then two orientational ordering parameters for the internal motion, S_{20} and S_{22}, are defined respectively as

$$S_{20} = \langle \mathscr{D}_{00}{}^{2}[\Omega_{C'M}(t)] \rangle$$

and

$$S_{22} = \langle \mathscr{D}_{02}{}^{2}[\Omega_{C'M}(t)] \rangle + \langle \mathscr{D}_{0-2}{}^{2}[\Omega_{C'M}(t)] \rangle$$

Finally, three (R^{c}, $R^{c}_{\perp}$ and $R^{c}_{\parallel}$) or four ($R^{c}_{\perp}$, $R^{c}_{\parallel}$, $R^{c}_{\perp}$ and $R^{c}_{\parallel}$) diffusion rates, depending on whether the global rotation of the protein is isotropic, two orienting ordering parameters (S_{20} and S_{22}) for the internal motion, and two Euler angles ($\Omega_{CC'}$ and Ω_{MG}) can be determined to describe the dynamics of a protein by simulating spectra with SRLS model.

1.7.2 Application of the SRLS Approach to NMR Studies of Protein Dynamics

Currently, the model-free (MF) approach is most popular in analyzing ^{15}N NMR relaxation data (42, 43, 44). In the model-free approach, it has been assumed that: (1) The global diffusion of the protein and the internal motion of the ^{15}N-H bond are independent (not coupled); (2) The local ordering and magnetic tensor frames are axially symmetric and collinear (42, 43, 45).

The slowly relaxing local structure (SRLS) approach has also been developed for NMR, and can be regarded as a generalized version of the MF approach (45, 46, 47, 48) : (1) The SRLS approach accounts for the coupling of the global diffusion and the internal motion of the N-H bond by the local ordering potential; (2) The general (axial or rhombic) geometry of the local ordering is considered in the SRLS approach.

1.8 THE MICROSOPIC ORDER MACROSCOPIC DISORDER (MOMD) MODEL

The microscopic order macroscopic disorder (MOMD) model has been developed by Freed and coworkers (49). When the global tumbling motion is slow

enough, the SRLS model reduces to MOMD model, where the spin labels are randomly distributed in all orientations, and the local motion occurs but is constrained by an ordering potential. The MOMD model can be used to simulate spectra of proteins larger than 50 kD or small proteins in highly viscous solution or at low temperature so that the global tumbling is reduced and can be regarded as frozen. The parameters derived from the program based on the MOMD model are the rotational diffusion rates and the order parameters of the internal motion [The global tumbling is slow enough and has negligible effect].

1.9 T4 LYSOZYME

T4 lysozyme, a member of the lysozyme family, plays an important role in the lysis of bacteria such as *Escherichia coli* B infected by phage T4 (50). The cell wall of bacteria is built by oligosaccharides cross-linked together by the peptide chains extended from the lactyl groups of N-acetylmuramyl residues. Both T4 lysozyme and hen egg white lysozyme, another member of the lysozyme family, catalyze the hydrolysis of the glycosidic bond in oligosaccharides so that the cell wall can be broken. However, T4 lysozyme, different from hen egg white lysozyme, hydrolyzes only the glycosidic bond connecting to C-1 of the N-acetylmuramyl peptide residue when acting on the peptidoglycan which is a major component of the cell wall (51, 52). With Tsugita's research, Asp20, Gln105 and Trp138 are essential amino acid residues for T4 lysozyme's catalytic function (53).

T4 lysozyme is a monomeric enzyme composed of 164 amino acid residues with a molecular weight of 18700 daltons. The secondary structure (see Figure 1-4) has already been determined by NMR spectroscopy by Zuiderweg and coworkers (54) as well as by X-ray crystallography by Matthews and coworkers (55). Its tertiary

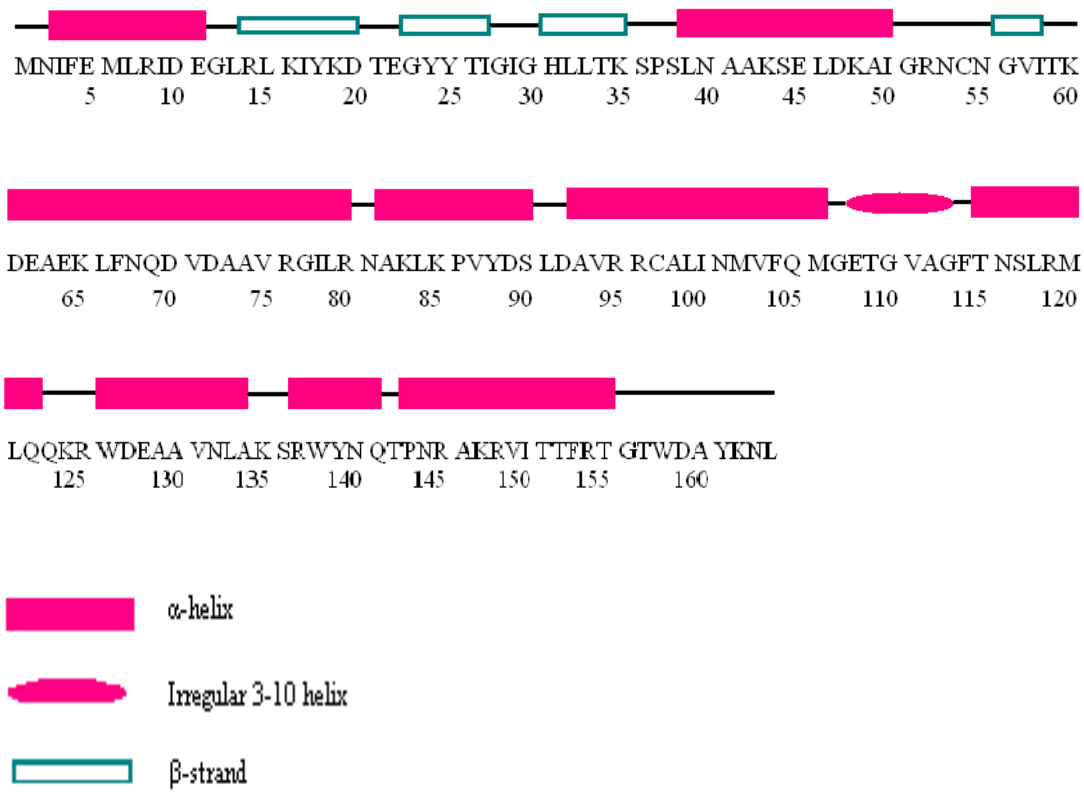

Figure 1-4. The secondary structure of T4 lysozyme from N-terminus to C-terminus.

structure has been determined by X-ray crystallography at 2.5 Å resolution by Matthews and coworkers in 1974 (56), and refined at 2.4 Å resolution in 1978 (55) as well as at 1.7 Å resolution in 1987 (15) by X-ray crystallography. Its body dimensions are 50*30*30 Å.

T4L is a well documented protein and thus used as a model system to test ESR method including the multifrequency ESR method in the study of protein dynamics. In the future, less well known protein can be characterized based on the method developed with the help of T4L (10).

T4L consists of N- and C- terminal domains connected by a long interdomain helix (cf. Figure 2-1). The C-terminal domain is larger and ranges from approximately residue 75 to the C-terminus (i.e. residue 164) (57). The N-terminal domain is smaller and ranges from approximately residue 13 to residue 65. The first ten N-terminal residues are not statically part of the N- or C- terminal domain, but fluctuate with either of the two domains. The transition between the N- and C- terminal domains ranges from residue 65 to residue 75, in the middle of the interdomain helix. The two domains undergo hinge-bending motion about the long interdomain helix and such conformational mobility is important in allowing access of substrates to the active site cleft of the enzyme formed between two domains (58).

1.10 MOTIVATION FOR THIS WORK

This project was undertaken to test the application of multifrequency ESR for studying the dynamics of proteins. Thus, T4 lysozyme (T4L), a protein that has been extensively studied by the conventional ESR spectroscopy at X-band (9.3~9.4 GHz), and has a well-known structure from crystallography was selected as the model system to show that multifrequency ESR is a useful tool for studying protein dynamics.

Based on carefully performed experiments and quantitative analyses in this work, we focus on three types of motion within a protein: (1) The first one is the global tumbling of T4L. Previous to this research, the global tumbling of T4L was determined by NMR based on the ^{15}N T1/T2 ratio (59). The global tumbling of proteins less than 50 kD can be observed by cw (continuous-wave) ESR at X-band. (2) The second type of motion is backbone fluctuations. To study such motion, two solvent exposed residues which are connected to helices with different length and rigidity were individually spin labeled and studied in this work. It was expected that any observed spectral difference could be attributed to the different mobility of the backbone at these two sites, since the motion of the nitroxide tether should be similar in both cases. It has been shown by Columbus et al. that ESR is a useful tool for identifying the backbone fluctuations at sites attached to highly flexible backbone segments (60). In addition, Columbus et al. did suggest that the spectral difference at two sites attached to different helices results from their backbone motion, thus the mobility of ordered backbone segments (e.g. helices) should be distinguished by ESR (34). To further verify this assumption that the mobility of two helices on a globular protein can be distinguished by ESR, we extended the study on sites 72 and 131 of T4L performed by Columbus et al. with X-band ESR (34) by continuing to study these two sites with multifrequency ESR and quantitative simulations. Site 72 is on a long 5-turn rigid helix whereas site 131 is on a short 2.5-turn flexible helix. Also, compared to site 72, site 131 has higher Debye-Waller factors and hydrogen exchange rates, indicating larger amplitude backbone fluctuations (34). (3) The third type of motion is the modes of motion of the nitroxide tether. These modes are closely related to the environment that each site is exposed to at the tertiary level. The study of these modes can be very useful when a specific site (e.g. an active site) on a protein is studied for any change in spectral lineshape after binding to the substrate or inhibitor of this

protein, as well as when studying the solvent accessibility and the mobility of the side chain at consecutive sites so that the secondary structure can be identified based on the periodicity along the sequence.

Recently, besides R1 (MTSSL), some newly developed spin labels have been used in order to suppress the side chain motion about its tether so that the contribution from the backbone motion is more clearly discerned. In this work, we studied a second spin label R2 (4-CH_3-MTSSL; cf. Chapter 2). R2 is a more rigid spin label and has been suggested by Columbus et al. to be a better spin label for identifying the backbone fluctuations (34).

Sucrose has been widely used as the viscogen in previous ESR studies to slow down the global tumbling of proteins smaller than 50 kD so that the global tumbling is reduced and only internal motion including the backbone fluctuations and the side chain isomerizations are observed. For example, T4L has been studied in 30% sucrose solution at X-band so that the global tumbling of T4L is mostly suppressed. It has been revealed recently that Ficoll is a better viscogen than sucrose, since the osmotic pressure in Ficoll solution is much lower than that in sucrose solution with comparable viscosities for slowing down the modest size proteins such as T4L (61). Thus, we used Ficoll as the viscogen and studied samples in Ficoll solutions (cf. Chapter 3): (1) to show that with the help of the multifrequency experiments and the SRLS-model simulations, there is no necessity for adding either sucrose or Ficoll into the solution for proteins smaller than 50 kD and the modest size proteins such as T4L can be studied in water solution; (2) to test whether the previous assumption that the internal motion will not be affected in viscous solution is strict.

Finally, the reason for studying T4L in 65% sucrose solution (cf. Chapter 4) is: (1) We needed accurate values for magnetic tensor components; (2) We wanted to have an idea about the residual motion of the tether at lower temperatures.

1.11 INSTRUMENTS

The home built high field (high frequency) spectrometers at 95, 170 and 240 GHz have been developed by Freed and coworkers (62, 63). The high field spectrometers need superconducting magnets. The 170 and 240 GHz spectrometers use a common bridge and quasi-optics but different frequency sources and different resonator meshes.

CHAPTER 2

APPLICATION OF MULTIFREQUENCY ELECTRON SPIN RESONANCE SPECTROSCOPY TO STUDY DYNAMICS OF T4 LYSOZYME IN WATER SOLUTION

2.1 INTRODUCTION

In this chapter, we report the utilization of the multifrequency ESR approach to study the dynamics of T4 lysozyme (T4L) in water solution. T4L is a globular protein composed of 164 amino acid residues with a molecular weight of 18700 daltons. Its crystal structure has been well determined, as well as many sites of T4L have been spin labeled and studied by ESR (10, 64, 65). The crystal structure of T4L is given in Figure 2-1. In the case of T4L, the slower dynamic mode, i.e. the global tumbling, is almost frozen at high frequency (e.g. 240 GHz), but affects the low frequency (~ 9 GHz) spectra. In contrast, the faster dynamic modes, i.e. backbone fluctuations and side chain isomerizations, affect spectra at both low and high frequencies. To explore the dynamics of the spin label linked to T4L at two solvent exposed helical sites, 72 and 131, we collected 57 multifrequency ESR spectra over a temperature range of 2 to 32 ^{o}C in water solution. Compared to our previous two-frequency study on these two sites of T4L (28), we made the following improvements: (1) We extended the multifrequency study to four frequencies consisting of 9, 95, 170 and 240 GHz; (2) Great care was taken to ensure that the spectra taken at all four frequencies, necessarily on several spectrometers, were on the same sample and at the same temperature; (3) The newer and improved high frequency ESR spectrometers utilized in this study provided order-of-magnitude improvement in signal-to-noise over the

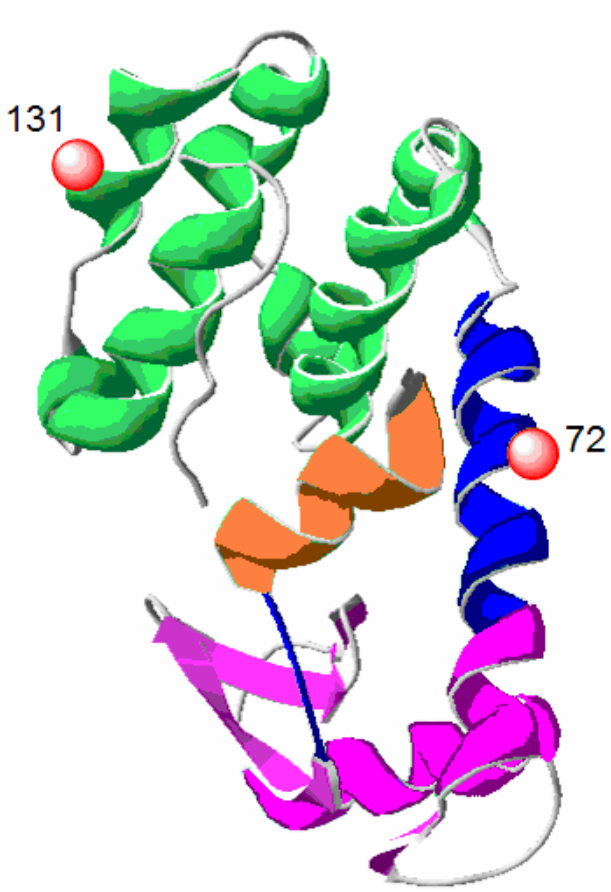

Figure 2-1. Ribbon diagram of the crystal structure of T4 lysozyme. (Sites 72 and 131 are identified as spheres.) The colors indicate the different domains (green for C-terminal domain, purple for N-terminal domain) and the interdomain regions (blue). The helix in orange fluctuates with either the N- or C- terminal domain.

previous study and thereby enabled more reliable spectral fitting, especially with respect to distinguishing more than one spectral component; (4) An additional nitroxide spin label, R2 (4-methyl-MTSSL) with structure shown in Figure 2-2, was also used in order to constrain conformational transitions of the side–chain, so that contributions from any backbone fluctuations could be enhanced. We simulated these extensive experimental spectra with the SRLS model and very good fits were achieved to all the data. Analyzing the fitting parameters, in addition to comparing our results with previous studies, provided further insight into the various dynamic modes of T4L (10, 34, 37, 66, 67, 68).

2.2 EXPERIMENTAL

Four nitroxide labeled T4L mutants − 72R1, 131R1, 72R2, and 131R2, were prepared and purified according to methods previously described (10). The concentration of protein in each sample was between 1 and 2 mM.

The 9 GHz ESR spectra were obtained on a commercial Bruker spectrometer at a frequency of 9.34 GHz. High field ESR spectra were obtained on home-built spectrometers. The microwave frequencies for the 95, 170, and 240 GHz spectrometers were calibrated, respectively, to be 95.00, 171.10, and 236.64 GHz.

Great efforts were made to ensure that the multifrequency data collected on the different spectrometers were consistent. First, the same sample was used in experiments performed on spectrometers at all frequencies. 17-mm-diameter quartz coverslips (ESCO products) were used as sample holders. About 2 μl of sample was placed between a flat quartz coverslip and an etched quartz coverslip with a circular concavity in the middle. The diameter of the concavity to hold the sample is about 1 cm. A thin layer of vacuum grease (Dow Corning) was applied on the edge to create a

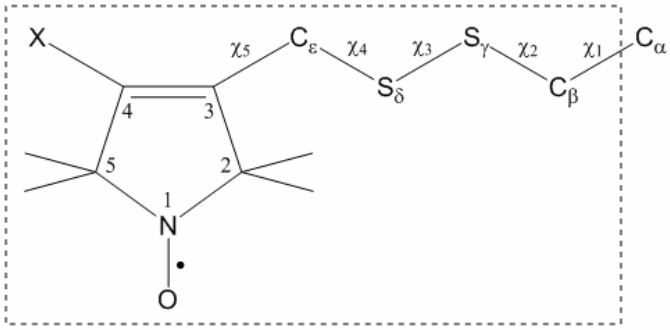

Side Chain R1 (R2)

X = H for R1 (MTSSL)

X = CH_3 for R2 (4-methyl-MTSSL)

Figure 2-2. Structure of the R1 (R2) side chain.

seal between the two coverslips. Such a sample holder was discussed in detail elsewhere (69). This same sample and sample-holder was utilized for all three high frequencies. For most experiments performed at 9 GHz it was more convenient to use samples of identical solutions, but sealed in glass capillaries. However in these cases, we first compared the room temperature 9 GHz spectra of the sealed glass-capillary samples with those taken at 9 GHz with the quartz-plate samples utilized at high frequencies. We confirmed that samples in these two types of sample holders yielded identical spectra. For the glass capillary samples, 5 μl of solution was placed in a 0.8 mm i.d. capillary, which was then sealed with fast epoxy.

The temperature at the sample was well calibrated on all spectrometers. In order to calibrate the temperature, for samples placed between quartz coverslips, a very thin copper-constantan thermocouple was incorporated into the aqueous sample through the vacuum grease; for the sample sealed in the glass capillary, a copper-constantan thermocouple was placed outside the capillary in the airflow and very close to the sample. The accuracy of the temperature was within $\pm$ 1^{o}C.

To avoid lineshape distortion, when collecting data at all the frequencies, we paid special attention to ensure that (1) the modulation amplitude was low enough; (2) the time constant was small enough relative to the field sweep rate; (3) the microwave power was low enough to prevent saturation. The experimental parameters for the data collected at four frequencies are listed in Appendix.

The phase of the experimental spectra at 95, 170, and 240 GHz was adjusted to correct for a small admixture of dispersion signal, according to the procedure described previously (70).

2.3 METHODS

2.3.1 Multifrequency Fitting Using the Slowly Relaxing Local Structure (SRLS) Model

Nonlinear least squares (NLLS) fits were performed to simulate the multifrequency spectra of the four samples listed in Table 2-1 at temperatures from 2 to 32°C using the fitting program based on the SRLS model. Two dynamic modes of T4L, the global tumbling and the internal motion, are decomposed in the SRLS model. Rotational diffusion tensors for these two modes are represented respectively by $\boldsymbol{R}^{\mathbf{c}}$ (global) and $\boldsymbol{R}^{\mathbf{o}}$ (internal). The theoretical foundation for this model, the definitions of fitting parameters and the fitting procedures are described elsewhere (28). Fitting parameters, including rotational diffusion tensors $\boldsymbol{R}^{c}$ and $\boldsymbol{R}^{o}$, potential coefficients (c_{20} and c_{22}), a structural parameter (β_d), and the Lorentzian broadening $\boldsymbol{W}$ are obtained from the best fits. Spectra at different frequencies were fit simultaneously. That is, the same set of fitting parameters was used to fit the spectra at all four frequencies, except that $\boldsymbol{W}$ the residual width (taken as isotropic W) is allowed to be different at the different frequencies. The observed frequency dependence of W is likely due to local variations in aqueous polarity which affect the $\boldsymbol{g}$ and $\boldsymbol{A}$ tensors, with the role of the former increasing with frequency (6, 28, 68, 71, 72).

Four coordinate frames are introduced for the simulation. The first is the magnetic tensor frame, in which the $\boldsymbol{A}$ and $\boldsymbol{g}$ tensors are defined. For most nitroxide spin labels, the three principal axes of the $\boldsymbol{A}$ tensor and the $\boldsymbol{g}$ tensor coincide (40, 41), and our rigid limit simulations at 9 and 170 GHz are consistent with this. Thus, the Euler angles between the $\boldsymbol{A}$ tensor frame and the $\boldsymbol{g}$ tensor frame were set to zero in all simulations. The x-axis is parallel to the N-O bond of the nitroxide and the z-axis is parallel to the p^z orbital of the nitrogen. The second axis frame is the internal diffusion frame for the rotational motion of the spin labeled tether (including possible local

Table 2-1. The nitroxide labeled T4 lysozyme samples for multifrequency ESR study in water solution

Sample No.	Mutant Site	Spin Label	Frequency (GHz)			
			9	95	170	240
1	72	R1	√ [a]	√	√	√
2	131	R1	√	√	√	√
3	72	R2	√	√	√	
4	131	R2	√	√	√	√

[a] A √ indicates the ESR spectrum has been recorded.

backbone motions). The diffusion of the tether may be taken to be axially symmetric around the z-axis, a matter discussed further below. Thus, the rotational diffusion tensor components, R^{o}_{x}, R^{o}_{y} and R^{o}_{z}, become $R^{o}_{x} = R^{o}_{y} = R^{o}_{\perp}$ and $R^{o}_{z} = R^{o}_{\parallel}$. The three Euler angles (α_d, β_d and γ_d) that describe the transformation between the internal diffusion frame and the magnetic tensor frame (i.e. diffusion tilt angles), are related to the conformation of the nitroxide labeled tether (73, 74). Among the three diffusion tilt angles, β_d is the angle between the main (z) axis of the internal diffusion frame and the z-axis of the magnetic tensor frame, and is used as a fitting parameter. Given the assumed axial symmetry of $\boldsymbol{R^o}$, $\alpha_d = 0$, and γ_d is set to zero for convenience (28).

The orienting potential for the diffusion of the tether is referred to the third axis system, the internal director frame, which is taken as axially-symmetric for convenience. The reorientation of the spin labeled tether is restricted by interaction with its local neighborhood, and the tether tends to align itself into the direction of minimum potential energy. The principal axes of alignment of the spin labeled tether are taken as coincident with the internal diffusion frame, again for convenience. The degree of restriction of the local motion is characterized by the order parameter S_{20}, and S_{22} measures the asymmetry of this ordering (i.e. its non-axiality). S_{20} and S_{22} are obtained from the coefficients (c_{20} and c_{22}) in the expansion of the local potential energy function. The fourth coordinate frame is for the tumbling of the protein and is defined as the global diffusion frame. The tumbling of T4L is assumed to be isotropic and there is no orienting potential for the tumbling. The assumption of isotropic $\boldsymbol{R^c}$ has been found in a NMR study on T4L (59, 75).

2.3.2 Global Nonlinear Least Squares (NLLS) Fitting

In the fitting program, most of the fitting parameters are obtained from the global NLLS fits to the series of spectra obtained at multiple frequencies. The fitting

parameters are varied until the sum of the differences between the best fits and the experiments at the various frequencies is minimized. The quality of the global fits is estimated by the reduced χ^2, which is calculated by (28)

$$\chi^2_{\text{NLLS}} = \frac{1}{N_{\text{total}} - N_{\text{parameter}}} \sum_{j=1}^{N_{\text{frequency}}} \sum_{i=1}^{N_{\text{data}}} \left[\frac{(\text{data}_i - \text{simulation}_i)^2}{\sigma^2} \right]_j$$

(1)

where N_{data} is the number of data points in a spectrum, N_{total} is the total number of data points of all frequencies, $N_{parameter}$ is the total number of fitting parameters. In this equation, σ is the standard deviation of the spectral noise, which is assumed to be constant throughout a spectrum but can be different for spectra at the different frequencies (73). σ is obtained from the variance of a linear fit to the two baseline segments at either end of the spectrum that comprise 4%, 6%, 8%, or 6% of the sweep width respectively of the spectrum obtained at 9, 95, 170, or 240 GHz (73). In a global NLLS fitting, it is desirable that contributions to the reduced χ^2 from the spectral fits at each frequency should be weighted equally. For this purpose, first, a preliminary fitting to the multifrequency spectra was performed and the experimental data set was fit approximately with a set of fitting parameters. Then, some normally distributed noise was added at either end of the spectrum to adjust σ, so that the contributions to the reduced χ^2 from the preliminary fits at all frequencies are the same, before the final fitting. This guarantees that the spectra for the different frequencies are equally weighted in the fitting.

2.3.3 Global Linear Least Squares (LLS) Fitting

The presence of more than one component, i.e. two or three components, is allowed in the NLLS fitting. Unlike other fitting parameters, the relative population of

each component in the multi-component fitting is a parameter sought by LLS, and thus, cannot be preset to an initial value, but is determined at each iterative stage (73). The linear least squares fit minimizes the sum of squares of the residuals

$$\frac{\sigma_{9\ \mathrm{GHz}}}{\sigma_j}\left(\mathrm{data}_i - \sum_{k=1}^{N_{\mathrm{component}}} \mathrm{spc}_{ik} * \mathrm{population}_k\right)_j ,$$

(i = 1 to N_{data} and j = 1 to $N_{\mathrm{frequency}}$)

(2)

where $N_{\mathrm{component}}$ is the number of components, and spc is the simulated spectrum of the k_{th} component. We introduce the same weighting factor ($1/\sigma^2$) in the LLS fitting as in the NLLS fitting, so that all frequency spectra are equally weighted in the LLS process for estimating the relative population of each component. The original SRLS program was modified (cf. the modified subroutine in Appendix) by introducing $\sigma_{9\ \mathrm{GHz}} / \sigma_j$ in Equation (2), which is tabularized in Appendix. Generally, the population of a given component from the global fits to the multifrequency dataset is within 5% from the average population of this component from a group of single-frequency fits.

Overall, by using good weighting factors for both NLLS and LLS minimization, in a global analysis, spectra at various frequencies can be regarded as approximately equally important when searching for the best fit parameters.

2.4 RESULTS

2.4.1 Summary

The experimental data and the best fits to spectra of the four mutants in water solution (samples 1 to 4 in Table 2-1) collected at 2, 12, 22, and 32^{o}C are displayed in Figure 2-3 and the best fit parameters are listed in Table 2-2. The diffusion tilt angle

Figure 2-3.

The multifrequency ESR spectra of 72R1, 131R1, 72R2, and 131R2 recorded in water solution at 2, 12, 22, and 32 ^{o}C; experimental data (solid line), simulations (dashed line).

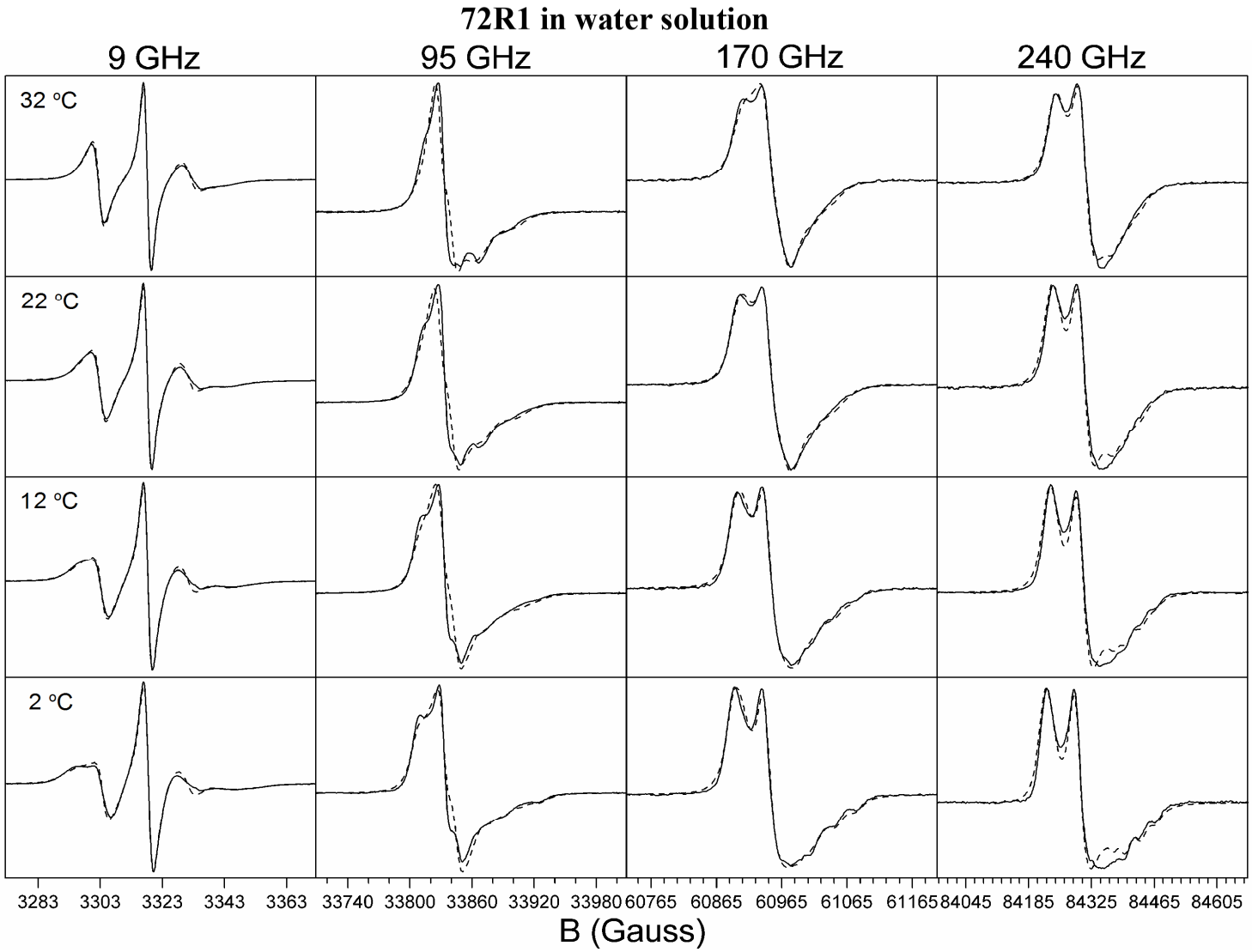
72R1 in water solution
9 GHz
95 GHz
170 GHz
240 GHz
32 °C
22 °C
12 °C
2 °C
3283 3303 3323 3343 3363
33740 33800 33860 33920 33980
60765 60865 60965 61065 61165
84045 84185 84325 84465 84605
B (Gauss)

Figure 2-3 (Continued)

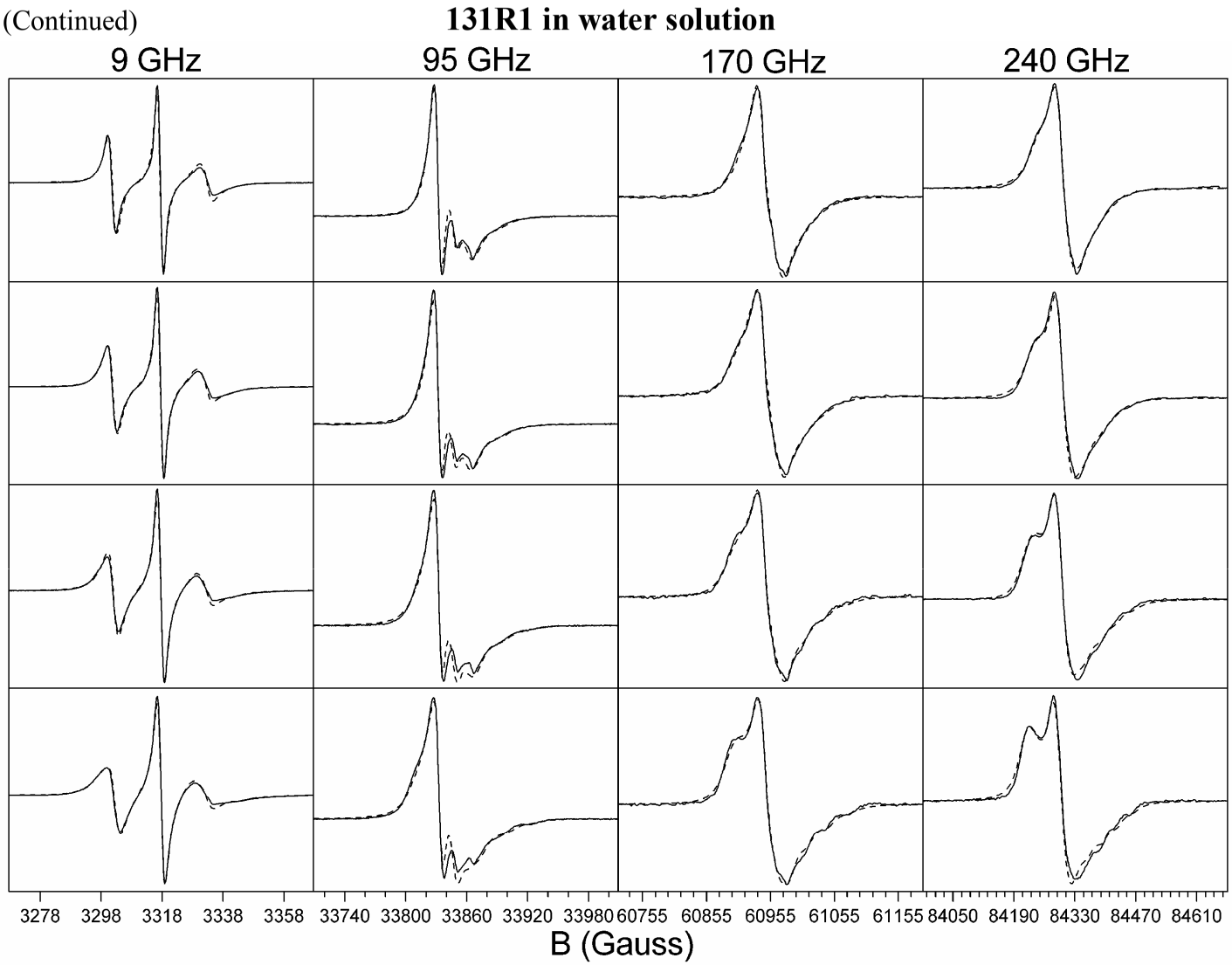

Figure 2-3 (Continued)

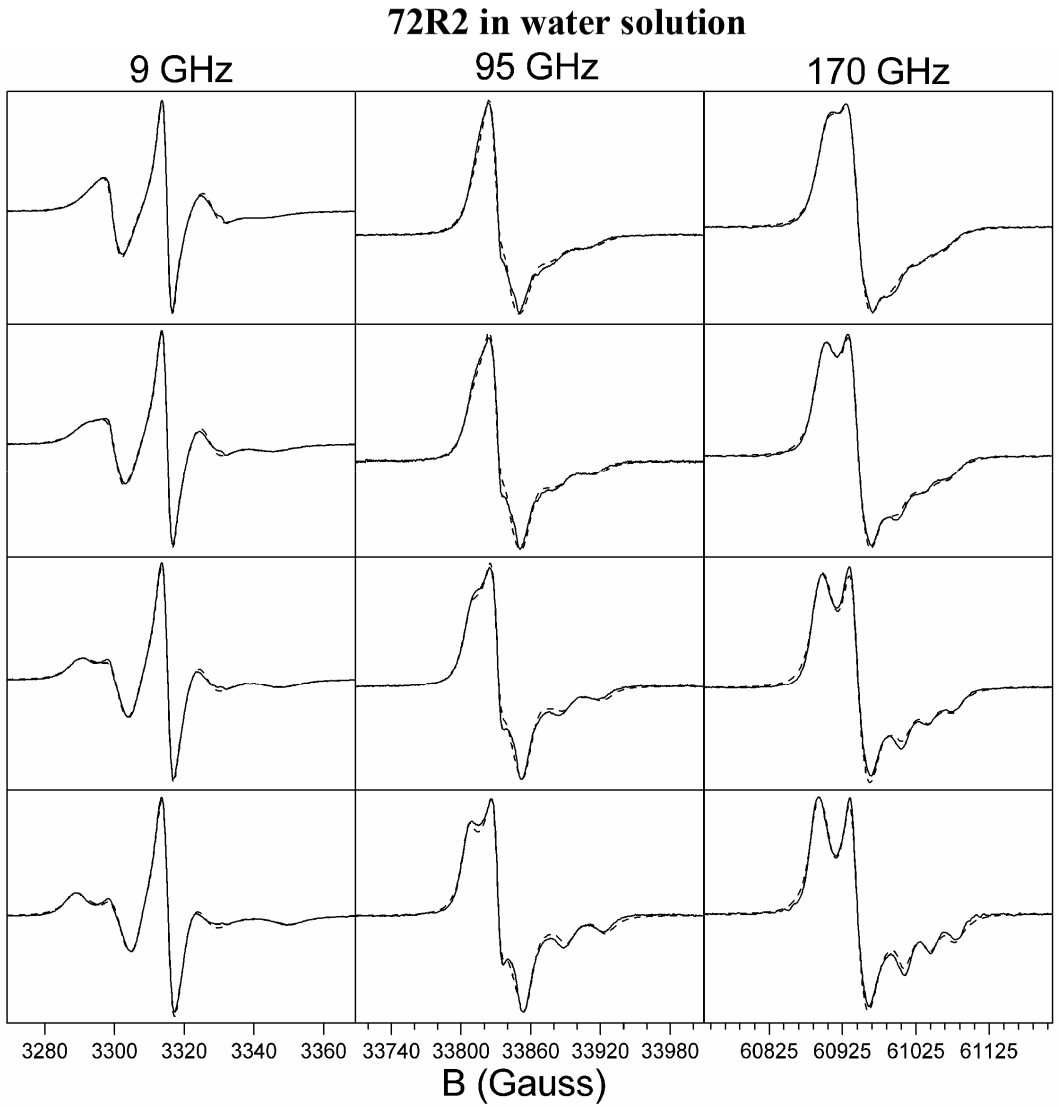

Figure 2-3 (Continued)

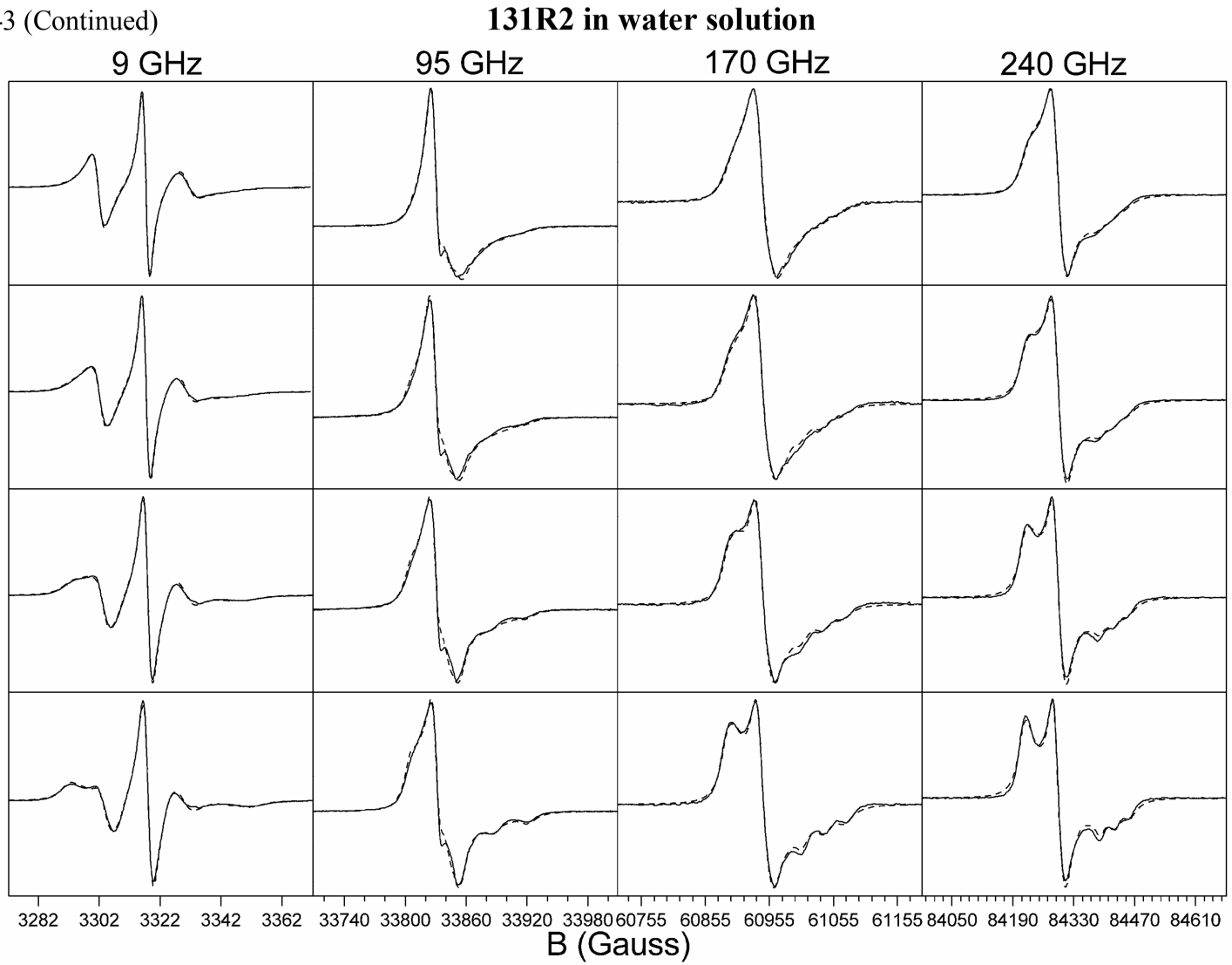

Table 2-2.

Best fit parameters of nitroxide labeled T4 lysozyme in water solution

Mutant	T (°C)	Comp.	$R^{o}_{\perp}$ (10^{7} s^{-1})	$R^{o}_{\parallel}$ (10^{7} s^{-1})	c_{20}	c_{22}	S_{20}	S_{22}	Popu.	R^{e} (10^{7} s^{-1})	W_{9} (G)	W_{95} (G)	W_{170} (G)	W_{240} (G)
72 R1	2	1	3.98	2.88	3.30	0.05	0.64	0.00	0.32	0.68	0.73	1.02	1.92	1.47
		2	40.7	0.16	3.49	-1.86	0.59	-0.16	0.38					
		3	49.0	0.42	3.21	-2.73	0.43	-0.31	0.30					
	12	1	5.62	3.47	3.30	0.18	0.64	0.01	0.22	1.00	0.76	1.50	1.30	1.56
		2	44.7	0.20	3.37	-1.75	0.58	-0.15	0.44					
		3	57.5	0.50	2.79	-1.98	0.45	-0.25	0.34					
	22	1	7.08	4.07	3.22	0.25	0.63	0.02	0.09	1.29	0.75	1.38	1.12	1.25
		2	49.0	0.19	3.31	-1.67	0.58	-0.15	0.48					
		3	63.1	0.63	2.62	-1.66	0.45	-0.22	0.43					
	32	2	57.5	0.22	3.24	-1.66	0.57	-0.16	0.50	1.62	0.79	1.32	1.94	0.88
		3	67.6	0.79	2.30	-1.30	0.43	-0.20	0.50					
131 R1	2	1	3.47	5.01	3.00	-0.16	0.60	-0.02	0.16	0.81	0.92	2.52	3.29	3.89
		2	47.9	1.66	2.85	-1.64	0.50	-0.19	0.54					
		3	37.2	0.63	1.31	1.34	0.20	0.32	0.30					
	12	1	4.07	5.89	3.00	-0.11	0.60	-0.01	0.14	1.29	0.86	2.16	2.61	2.37
		2	52.5	2.34	2.56	-1.55	0.45	-0.21	0.59					
		3	43.7	0.98	1.28	1.14	0.21	0.28	0.27					
	22	1	4.79	5.01	2.85	-0.03	0.58	0.00	0.06	1.51	0.79	1.82	3.87	1.94
		2	58.9	1.74	2.37	-1.23	0.45	-0.18	0.64					
		3	56.2	0.85	1.29	0.79	0.25	0.19	0.30					
	32	2	63.1	2.40	2.21	-0.98	0.44	-0.15	0.61	1.91	0.81	2.30	3.99	4.87
		3	60.3	1.07	1.24	0.77	0.24	0.19	0.39					

Table 2-2 (Continued)

	2	1	4.27	3.89	3.41	-0.09	0.65	-0.01	0.73	0.69	0.60	0.19	1.88	
		2	33.1	2.14	2.91	-0.87	0.57	-0.09	0.27					
	12	1	5.62	5.13	3.40	-0.08	0.65	-0.01	0.61	1.02	0.57	1.11	1.67	
72		2	39.8	2.51	2.94	-0.66	0.58	-0.07	0.39					
R2	22	1	8.71	6.03	3.40	0.02	0.65	0.00	0.51	1.29	0.60	0.34	1.30	
		2	46.8	4.57	2.96	-0.79	0.58	-0.08	0.49					
	32	1	11.7	8.13	3.30	-0.27	0.64	-0.02	0.45	1.78	0.55	0.36	0.93	
		2	51.3	6.03	2.91	-0.64	0.58	-0.07	0.55					
	2	1	9.12	1.66	3.73	-0.74	0.68	-0.05	0.56	0.68	0.76	1.55	3.22	3.67
		2	42.7	3.02	2.81	0.43	0.57	0.05	0.44					
	12	1	11.0	1.86	3.70	-0.91	0.67	-0.06	0.44	0.98	0.68	1.49	2.38	3.95
131		2	50.1	3.89	2.80	0.44	0.57	0.05	0.56					
R2	22	1	12.9	2.45	3.65	-1.23	0.65	-0.09	0.37	1.23	0.68	1.67	1.96	3.77
		2	60.3	6.31	2.75	0.51	0.56	0.06	0.63					
	32	1	15.8	6.76	3.60	-0.76	0.66	-0.05	0.35	1.78	0.58	1.17	2.98	3.30
		2	69.2	7.41	2.75	0.77	0.55	0.09	0.65					

Estimated errors: $R^{o}_{\perp} \leq 7\%$, $R^{o}_{\parallel} \leq 17\%$; $c_{20} \leq 5\%$; $S_{20} \leq (\pm 0.02)$, $S_{22} \leq (\pm 0.05)$; Popu $\leq (\pm 0.05)$; $R^{c} \leq 7\%$.

Table 2-3. The best fit diffusion tilt angle (β_d)

Mutant	β_d (o)
72 R1	21
131 R1	20
72 R2	30
131 R2	35

(β_d) for each mutant was set to the value listed in Table 2-3 after having been determined as described below. As shown in Figure 2-3, very good agreement is obtained between the experimental data and the simulations. We first summarize the main features revealed from the fitting. For R1, three components with different dynamic and ordering parameters for the internal motion are present in most cases. Based on their mobilities, they are referred to as the (relatively) "immobile component", the "intermediate component", and the (relatively) "mobile component", which respectively correspond to components 1, 2, and 3 in Table 2-2. The "immobile component" has almost isotropic rotational local diffusion with $R^o_\perp$ close to $R^o_\parallel$. This component is characterized by having a higher ordering and a much slower $R^o_\perp$ when compared to the other two components. Unlike the immobile component, the local rotational diffusion of the intermediate and the mobile components is highly anisotropic, with $R^o_\perp$ more than an order of magnitude larger than $R^o_\parallel$. The values of $R^o_\perp$ in these two components are about 7 to 14 times those in the immobile component. The mobile component, as compared to the intermediate component, has comparable rotational diffusion rates but much lower ordering.

For R2, the spectra were satisfactorily fit to the superposition of two spectral components. The mobilities of these two components are comparable to those of the

immobile and the intermediate components of R1. Thus, for consistency, the two components of R2 are also referred to as the "immobile component" and the "intermediate component". For the intermediate component of R2, $R^o_\perp$ is about an order of magnitude larger than $R^o_\parallel$, and the values of $R^o_\perp$ are about 4 to 8 times those in the immobile component. For all the components of R1 and R2, S_{20} remains almost constant over the whole temperature range. (This is consistent with the previous 9 GHz results obtained by Columbus et al. (34). In their study in 30% sucrose solution at various temperatures, S_{20} was however fixed in all simulations and only the rotational diffusion rates were varied using the MOMD model.) The immobile spectral components of the four mutants have similar lineshapes, whereas the mobilities of the intermediate and the mobile components are mutant-dependent. The best fit results for the four mutants are described in detail below.

2.4.2 Temperature Dependence of the Internal Motion

2.4.2.1 Simulations of spectra of 72R1

The variation of $R^o_\perp$, S_{20} and the fractions of the three components with temperature for 72R1 are displayed in subplots 1a through 1c of Figure 2-4. At 2°C, the fractions of the three components are comparable. As the temperature increases, the fraction of the immobile component decreases from 32% at 2°C to 0% at 32°C, so that the fractions of the intermediate and the mobile components increase with increasing temperature. Thus at 32°C, the spectrum is composed of just two components with the same population. The immobile component, characterized by the three peaks in the g_{zz} region of the high field spectra, can be observed in the experimental spectra at 95, 170, and 240 GHz, when the temperature is below 22°C. However, it cannot be observed by eye in the experimental 9 GHz spectra even at 2°C.

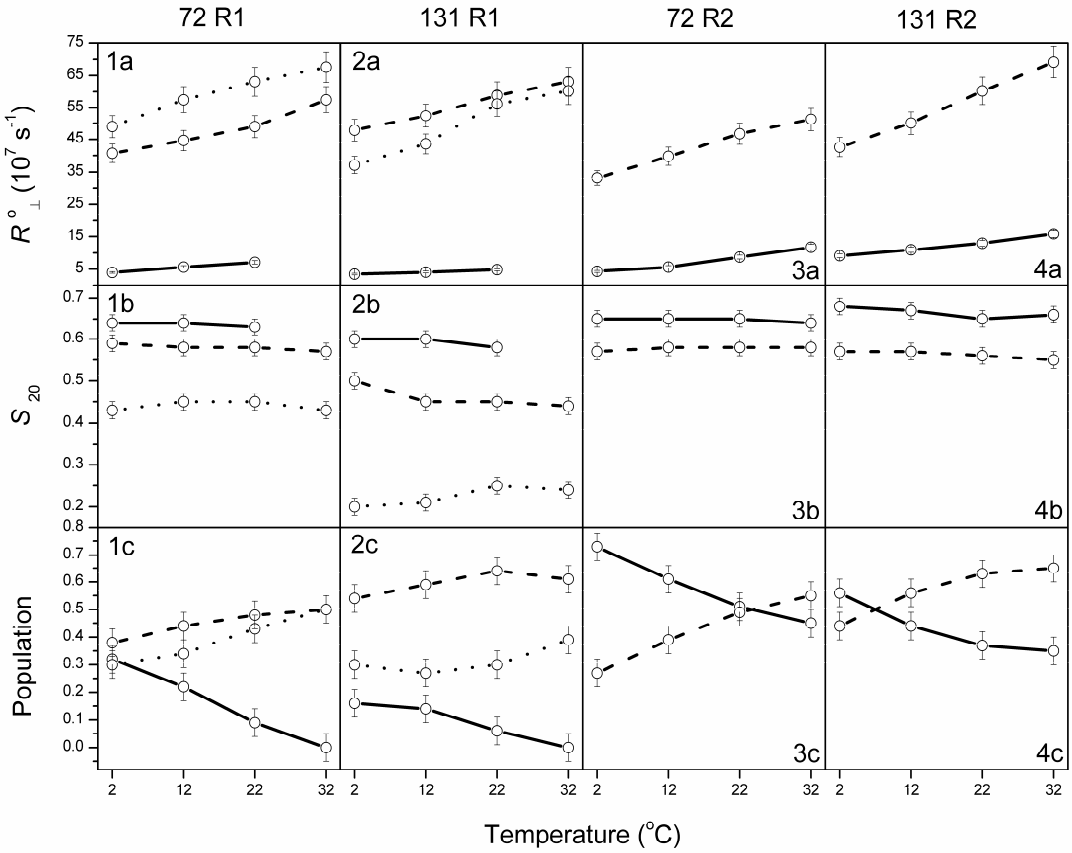

Figure 2-4. The best fit parameters of $R^{o}\perp$, S_{20}, and the relative populations vs temperature from analysis of spectra recorded in water solution (with error bars added); the immobile component (solid line), the intermediate component (dashed line), the mobile component (dotted line).

As shown in Figure 2-4, for the immobile component $R^o_\perp$ increases from $4.0*10^7$ s^{-1} at 2°C to $7.1*10^7$ s^{-1} at 22°C. $R^o_\perp$ ranges from $4.1*10^8$ s^{-1} at 2°C to $5.8*10^8$ s^{-1} at 32°C in the intermediate component, and from $4.9*10^8$ s^{-1} at 2°C to $6.8*10^8$ s^{-1} at 32°C in the mobile component. The values of $R^o_\perp$ for the intermediate and mobile components are comparable, with that for the former case somewhat smaller at the corresponding temperature. However, $R^o_\perp$ for the immobile component is nearly an order of magnitude smaller than for either of the other two components. The values of S_{20} remain almost constant with temperature at 0.64, 0.58, and 0.44, respectively in the immobile, the intermediate, and the mobile components. The values of S_{22} for the immobile component are very close to zero, indicative of the axial symmetry of the ordering, whereas the values of S_{22} in the intermediate and the mobile components are negative (-0.31 ~ -0.15), the implications of which are noted in the next sub-section.

2.4.2.2 Simulations of spectra of 131R1

Variations of $R^o_\perp$, S_{20}, and the populations of the three components with temperature for 131R1 are displayed in subplots 2a through 2c of Figure 2-4. Over the whole temperature range, the intermediate component is the most abundant, with a fraction larger than 50%. As the temperature increases, the fraction of the immobile component decreases from 16% at 2°C to 0% at 32°C, whereas those of the intermediate and the mobile components increase. Thus at 32°C, the immobile component finally disappears with the spectrum being composed of just two components. For the immobile component, the value of $R^o_\perp$, varying from $3.5*10^7$ s^{-1} at 2°C to $4.8*10^7$ s^{-1} at 22°C, is somewhat smaller than that for 72R1 at the corresponding temperature. $R^o_\perp$ ranges from $4.8*10^8$ s^{-1} at 2°C to $6.3*10^8$ s^{-1} at 32°C for the intermediate component, and ranges from $3.7*10^8$ s^{-1} at 2°C to $6.0*10^8$ s^{-1} at 32°C for the mobile component. Unlike 72R1, the value of $R^o_\perp$ of 131R1 for the

intermediate component is larger than that for the mobile component at the corresponding temperature. The values of S_{20} remain almost constant at 0.59, 0.46, and 0.23, respectively for the immobile, the intermediate, and the mobile components. These order parameters of 131R1 for the three components are all lower than those of 72R1, especially for the intermediate and the mobile components. The values of S_{22} in the immobile component are very close to zero, whereas the values of S_{22} in the intermediate and the mobile components are respectively negative (-0.21 to -0.15) and positive (0.19 to 0.32). [Note

$$S_{22} = \sqrt{\frac{2}{3}}\left(S_{xx} - S_{yy}\right)$$

indicating a switch in the non-axial preference in ordering from y to x.]

Columbus et al. (34) fit (by MOMD), using just a single component, the 9 GHz spectra of 72R1 and 131R1 with the same rotational diffusion rates but different order parameters. Our results show that the population distributions as well as the rotational diffusion rates at site 72 and site 131 are somewhat different. But, the difference in lineshapes at these two sites is still found to be primarily from the difference in ordering.

2.4.2.3 Simulations of spectra of 72R2

Variations of $R^o_\perp$, S_{20}, and the populations of the two components with temperature for 72R2 are displayed in subplots 3a through 3c of Figure 2-4. The immobile component is the dominant component with a percentage larger than 60% when the temperature is below 22°C, whereas it is approximately equal in percentage to the intermediate component when the temperature is at or above 22°C. The immobile component decreases by about 9% when the temperature increases by 10°C from 2 to 32°C. For this component, the value of $R^o_\perp$, varying from $4.3*10^7$ s^{-1} at 2°C

to $1.2*10^8$ s^{-1} at 32°C, is slightly larger than that of 72R1 at the corresponding temperature. The value of $R^o_\perp$ ranges from $3.3*10^8$ s^{-1} at 2°C to $5.1*10^8$ s^{-1} at 32°C in the intermediate component, which is smaller than that of 72R1. The values of S_{20} remain nearly unchanged at 0.65 and 0.58, respectively in the immobile and the intermediate components. These order parameters of 72R2 are almost the same as those of 72R1 for the corresponding components. The values of S_{22} in the two components are close to zero, indicative of axial symmetry.

Based on the fitting results, 72R1 and 72R2 have substantially different population distributions. The immobile component of 72R2 is about 40% greater than that of 72R1 at the corresponding temperature, as will be discussed in Discussion.

2.4.2.4 Simulations of spectra of 131R2

Variations of $R^o_\perp$, S_{20}, and the populations of the two components with temperature for 131R2 are displayed in subplots 4a through 4c of Figure 2-4. The immobile and the intermediate components are evenly distributed when the temperature is below 22°C. When the temperature increases up to 22°C, the intermediate component becomes more abundant with a percentage greater than 60%. The population of the immobile component decreases about 7% for every 10°C increase. $R^o_\perp$ increases from $9.1*10^7$ s^{-1} at 2°C to $1.6*10^8$ s^{-1} at 32°C in the immobile component, and increases from $4.3*10^8$ s^{-1} at 2°C to $6.9*10^8$ s^{-1} at 32°C in the intermediate component. The values of S_{20} remain nearly unchanged with temperature at 0.66 and 0.56, respectively in the immobile and the intermediate components. The values of S_{22} in the two components are close to zero.

Unlike for the case of R1, where the mobilities of the intermediate and the mobile components at site 72 differ from those at site 131 mostly in their ordering, 72R2 and 131R2 have similar S_{20} for the intermediate component (0.58 at site 72 vs

0.56 at site 131). Compared to 72R2, the intermediate component of 131R2 has faster $R^o_\perp$ and is about 15% more abundant.

The higher ordering of 131R2 in the intermediate component compared to that of 131R1 in either the intermediate or the mobile component can be explained by a steric clash of the 4-methyl group with the disulfide bond as suggested by Columbus et al. (cf. Discussion Section) (34). With regard to the population distribution, the comparison between 131R1 and 131R2 is similar to that between 72R1 and 72R2. 131R2 has about 35% higher percentage of immobile component than does 131R1.

2.4.3 Three Components for R1 and Two Components for R2

2.4.3.1 72R1

We found that the multifrequency spectra of 72R1 recorded at either 2 or 12^{o}C could not be simultaneously fit with just one or two components using the same set of fitting parameters. Liang et al. (28) succeeded in fitting these spectra with two components using the same set of fitting parameters, but they required the populations of the two components to be different in the fitting of spectra at different frequencies; they were not able to adequately justify this. The improved S/N, and the fact that four frequencies were used, enabled us to distinguish that in addition to the two components found in the study by Liang et al. (28), a slow motional component (i.e. the "immobile component") was discerned in our study. The three peaks corresponding to the immobile component can be observed by eye in the g_{zz} region of the high field spectra (see Figure 2-5A) with the help of the sensitivity improvement of the spectrometers, whereas these peaks could not be resolved in the previously published 250 GHz spectra.

In fact, some preliminary analyses were performed with two components present in the fitting: an immobile component and a relatively mobile component (the parameters for the two component fits to the multifrequency spectra of 72R1 recorded at 2^{o}C are listed in Table 2-4). However, satisfactory fits cannot be achieved at all frequencies: (1) Two small outer peaks, which are not present in the experimental data, appear in the simulated 9 GHz spectrum (see Figure 2-5B); (2) The fit to the 240 GHz spectrum is very poor (see Figure 2-5B). To merge the two outer peaks in the simulated 9 GHz spectrum, we tried to increase the linewidth or vary R^{c} in the fitting process, and neither attempt was helpful. The possibility of conformational exchange between the two components was suggested by Liang et al. (28) to address the problem that spectra at 9 GHz and at 250 GHz could not be fitted simultaneously when two components exist. To fit the multifrequency spectra of 72R1 at 2^{o}C, we tested this idea using a version of SRLS allowing for such exchange, and it was found that the two outer peaks that appear in the simulated 9 GHz spectrum, but which are not observed in the experimental data, were merged when the conformational exchange rate is increased to $6.3*10^{7}$ s^{-1} (see Figure 2-5C). However, this exchange rate is too slow on the 240 GHz ESR time scale, so that the fit to the 240 GHz spectrum cannot be improved (see Figure 2-5D) and is still poor. Consequently, the multifrequency spectra of 72R1 at lower temperatures, i.e. 2 or 12^{o}C, could not be simultaneously fit with two components even with conformational exchange included in the simulation.

In the present study, we allowed the presence of a third component in the simulations. We found consistently that the introduction of another relatively mobile component as the third component leads to good fits at all frequencies. Thus, for example, the two outer peaks in the simulated 9 GHz spectra are merged when three components with different mobilities exist (see Figure 2-5E). In all, the presence of

Table 2-4. The parameters for the two component fits to the multifrequency spectra of 72R1 and 131R1 recorded at 2°C, and for the single component fits to the multifrequency spectra of 72R2 and 131R2 recorded at 2°C

Mutant	Comp.	$R^{o}_{\perp}$ (10^7 s^{-1})	$R^{o}_{\parallel}$ (10^7 s^{-1})	c_{20}	c_{22}	S_{20}	S_{22}	Popu.	R^{e} (10^7 s^{-1})	W_9 (G)	W_{95} (G)	W_{170} (G)	W_{240} (G)
72R1	immobile	3.31	3.47	3.23	-0.09	0.63	-0.01	66	0.66	0.87	1.55	2.71	1.90
	mobile	33.9	0.09	2.45	-1.15	0.47	-0.16	34					
131R1	immobile	6.03	4.79	3.00	-0.13	0.60	-0.01	32	0.81	0.88	1.84	3.54	3.90
	mobile	33.9	0.10	1.50	0.04	0.33	0.01	68					
72R2	single	4.79	4.37	2.69	0.94	0.53	0.11	100	0.69	0.22	0.09	2.90	
131R2	single	7.24	6.17	3.88	2.91	0.54	0.24	100	0.68	0.10	0.48	4.06	5.29

Figure 2-5.

A: The 9 and 240 GHz experimental data of 72R1 recorded at 2 ^{o}C. The dashed rectangle shows the immobile component features that can be observed by eyes in the 240 GHz spectrum, but not in the 9 GHz spectrum.

B: The two component fits to the 9 and 240 GHz spectra of 72R1 recorded at 2 ^{o}C; experimental data (solid line), simulations (dashed line). The arrows point to the two outer peaks present in the two component fit but not in the experimental data. These two outer peaks are merged when the two components exchange with a rate of $6.3*10^{7}$ s^{-1} (C).

D: The two component fits to the 9, 95, 170, and 240 GHz spectra of 72R1 recorded at 2 ^{o}C; no exchange (black line), with exchange (red line).

E: The three component fit to the 9 GHz spectrum of 72R1 recorded at 2 ^{o}C; experimental data (solid line), simulation (dashed line). The outer peaks are not present in the three component fit.

A.

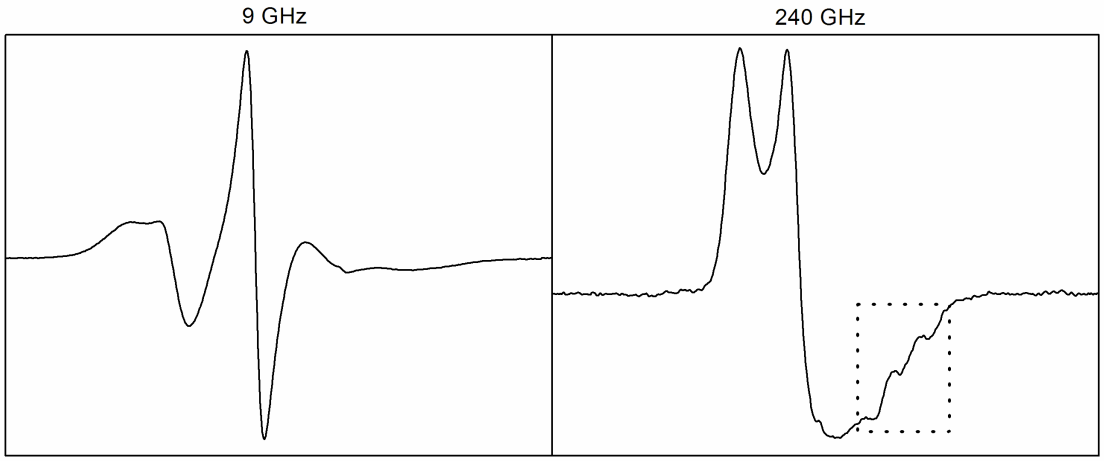

B.

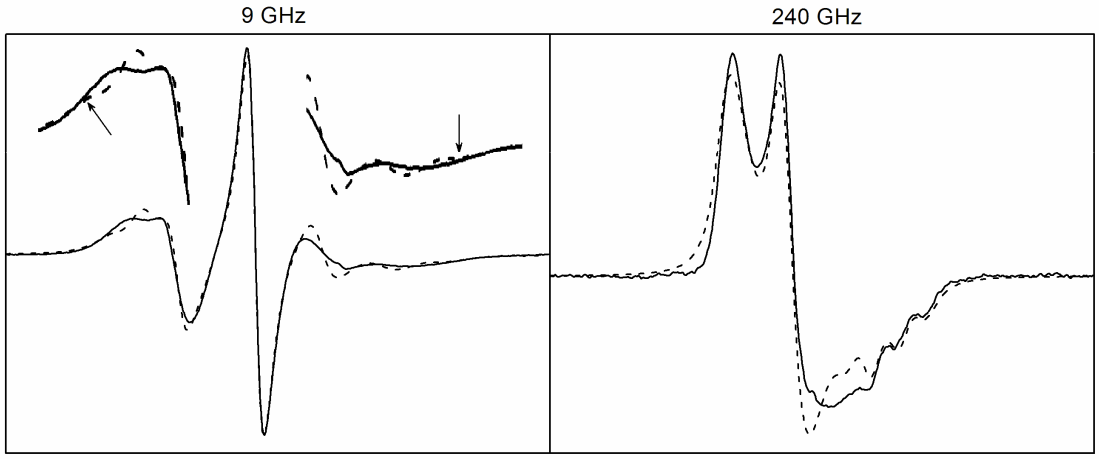

C.

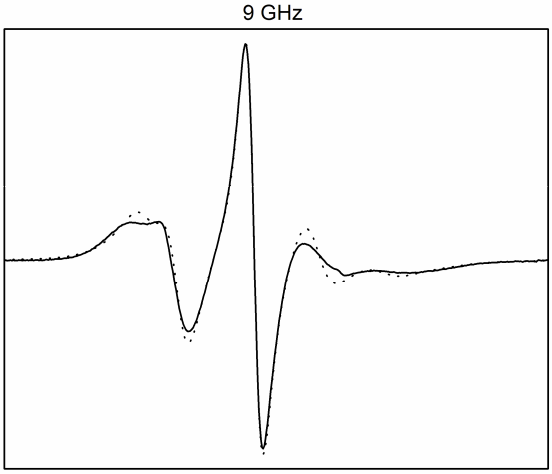

E.

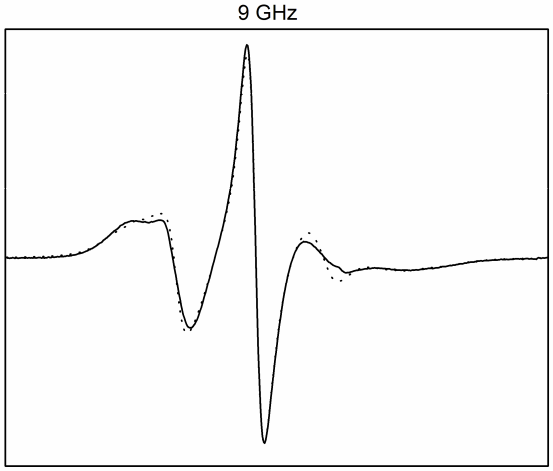

Figure 2-5 (Continued)

D.

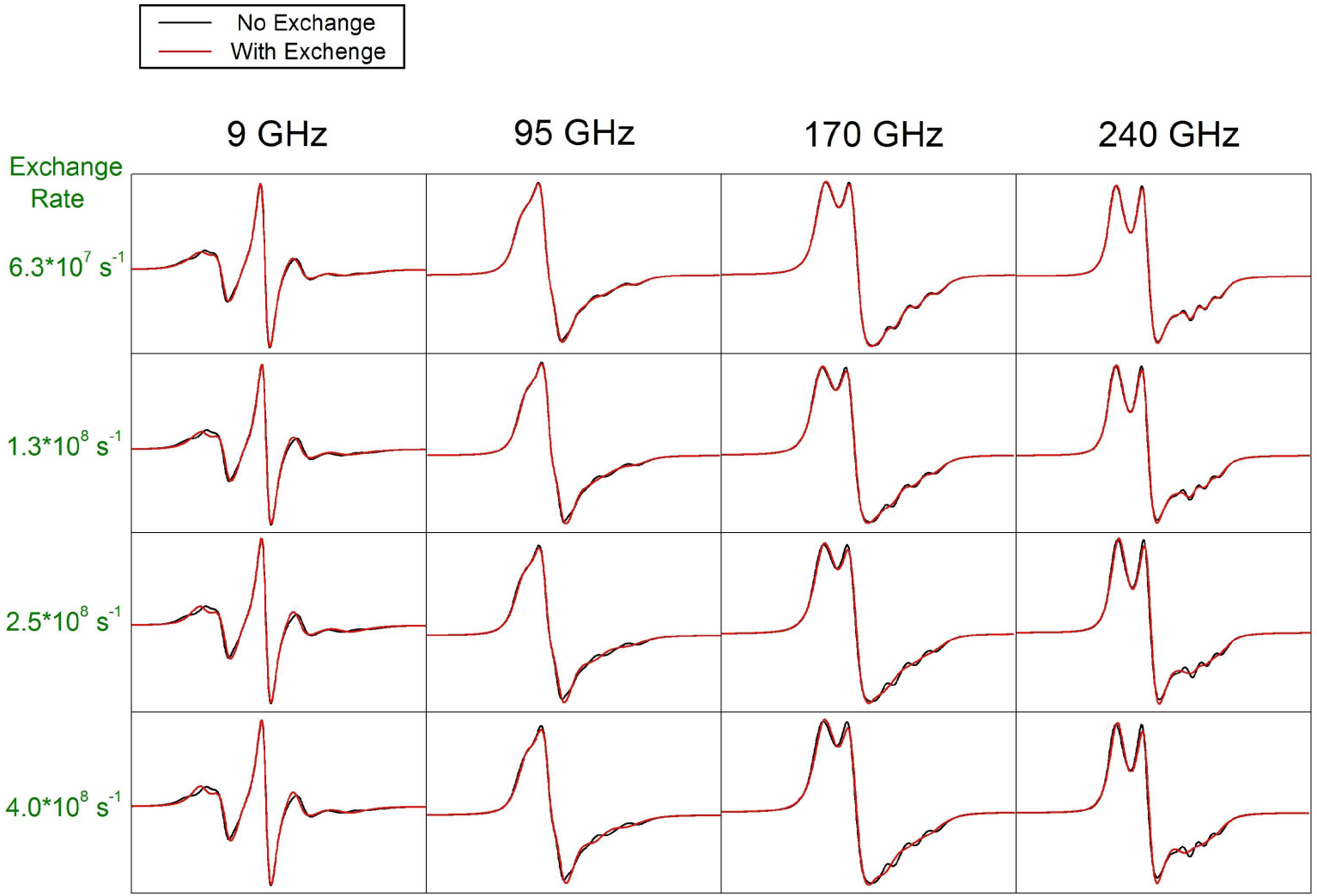

three components makes it possible to fit spectra at all frequencies with the same set of fitting parameters including the relative populations of the components.

For 72R1 at higher temperatures, i.e. 22 and 37.5^{o}C, Liang et al. succeeded in fitting the 9 and 250 GHz spectra simultaneously with a single component using the same set of parameters (28). Indeed, we do find that at higher temperature, e.g. 32^{o}C, the multifrequency spectra of 72R1 can be fit with a single component. However, to be consistent with the lower temperature 2^{o}C fitting results, we initialized the simulation of 32^{o}C spectra with three components and allowed the fitting process to determine if they are required; indeed, it discarded the immobile component. As noted in Barnes et al. (6), the 2^{o}C spectra should be more informative than the 32^{o}C spectra since the latter are more motionally narrowed. This makes the challenge of fitting spectra at lower temperatures a priority.

2.4.3.2 131R1

Liang et al. previously fit the spectra of 131R1 at 9 and 250 GHz with two components for temperatures at or below 22^{o}C, and with just one component for temperatures above room temperature, i.e. 37.5^{o}C (28). They found that, at lower temperatures, the spectra at these two frequencies could be fit simultaneously using the same set of fitting parameters except that different relative populations of the two components were required. Similar to 72R1, the spectral features corresponding to an immobile component can be observed in the high field spectra of 131R1 but cannot be resolved in the 9 GHz spectrum (see Figure 2-6A). We tried to simulate the spectra of 131R1 at 2^{o}C with two components: an immobile component and a relatively mobile component (the parameters for the two component fits to the multifrequency spectra of 131R1 recorded at 2^{o}C are listed in Table 2-4). Similar to the two component fitting for 72R1, two small outer peaks are present in the simulated 9 GHz spectrum but not

in the experimental data (see Figure 2-6B), and the g_{zz} region of the 240 GHz spectrum cannot be well fit (see Figure 2-6B). Moreover, the spectral features in the central region of the 95 GHz spectrum cannot be reproduced (see Figure 2-6B). Consequently, a third component was found to be necessary to reproduce the spectral features at all frequencies. This third component corresponds to the most mobile component amongst the three (see Figure 2-6C showing this component in the 95 GHz simulation). It also led to the same populations of the components for all four frequencies.

2.4.3.3 72R2

The 170 GHz spectrum of 72R2 recorded at 2 or 12^{o}C cannot be satisfactorily fit with only a single component since the spectral features in the g_{zz} region cannot be well reproduced by just a single component (see Figure 2-7). However, the 9 and 95 GHz spectra can be well fit at these temperatures with a single component. In order to reproduce the spectral features at all frequencies, a second component was allowed in the fitting. The parameters for the single component fits to the multifrequency spectra of 72R2 recorded at 2^{o}C are listed in Table 2-4.

2.4.3.4 131R2

As for 72R2 at lower temperatures (i.e. 2 and 12^{o}C) only the 9 and 95 GHz spectra of 131R2 can be well fit with a single component, whereas the 170 and 240 GHz spectra cannot be satisfactorily fit since the spectral features in the g_{zz} region cannot be well reproduced by just a single component (see Figure 2-8). Thus, a second component was again added in the fitting. [Columbus et al. showed in a previous paper that the 9 GHz spectra of 131R2 in 30% sucrose solution cannot be well fit with a single component using the MOMD model (34).] The parameters for the single component fits to the spectra of 131R2 recorded at 2^{o}C are listed in Table 2-4.

Figure 2-6.

A: The 9 and 240 GHz experimental data of 131R1 recorded at 2 ^{o}C. The dashed rectangle shows the immobile component features that can be observed by eyes in the 240 GHz spectrum, but not in the 9 GHz spectrum.

B: The two component fits to the 9, 95 and 240 GHz spectra of 131R1 recorded at 2 ^{o}C; experimental data (solid line), simulations (dashed line). The arrows respectively point to the two outer peaks present in the two component fit but not in the experimental data at 9 GHz, the poor fit to the central region of the 95 GHz spectrum, and the poor fit to the g_{zz} region of the 240 GHz spectrum.

C: The three component fit to the 95 GHz spectrum of 131R1 recorded at 2 ^{o}C; experimental data (solid line), simulation (dashed line). The fit to the central region is improved by the addition of the third component (i.e. the mobile component).

A.

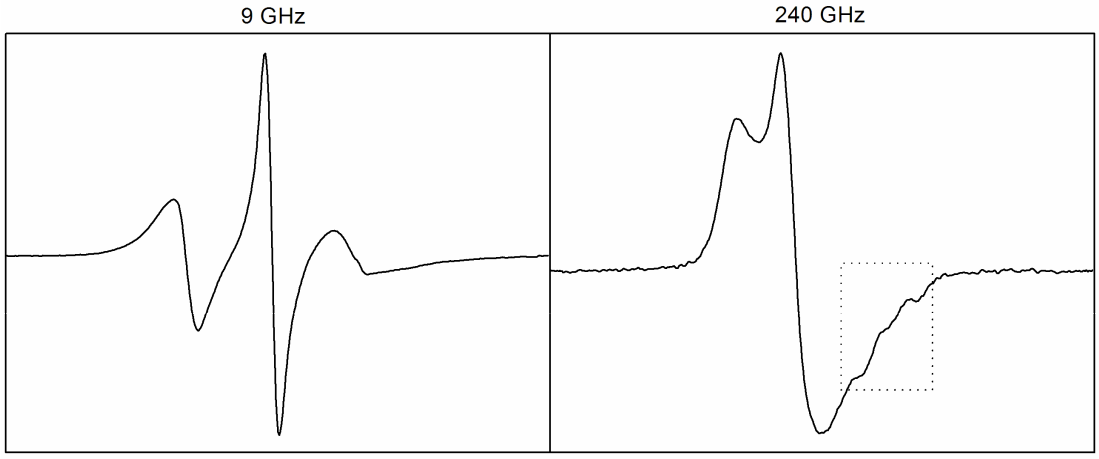

B.

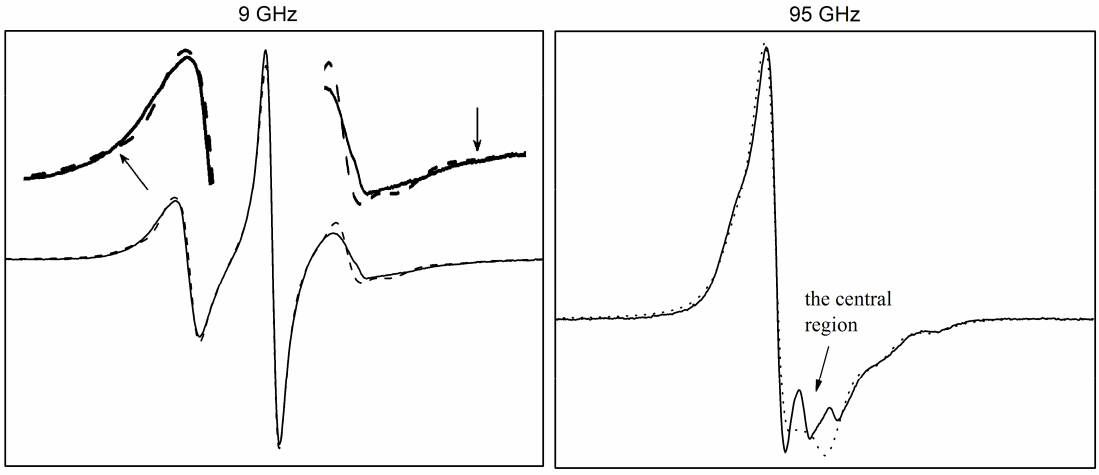

Figure 2-6 (Continued)

B.

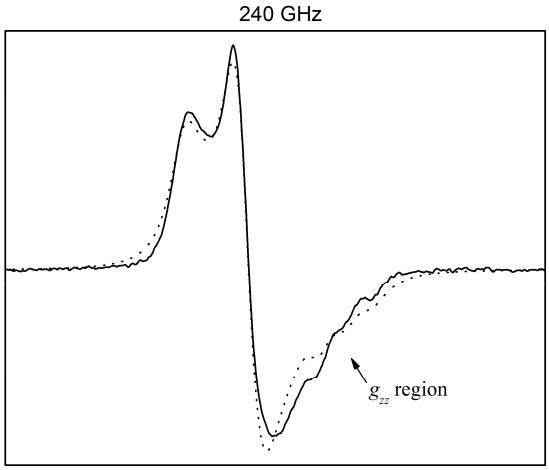

C.

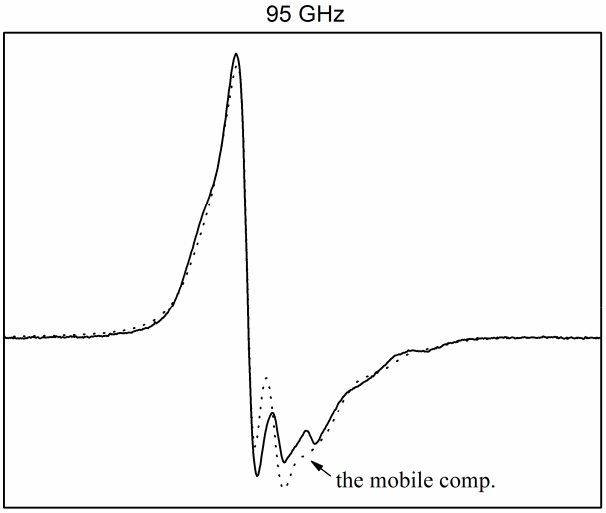

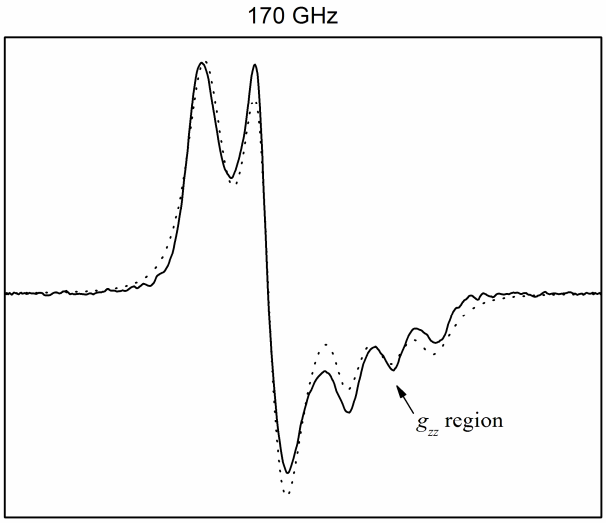

Figure 2-7. The single component fit to the 170 GHz spectrum of 72R2 recorded at 2 ^{o}C; experimental data (solid line), simulation (dashed line). The arrow points to the g_{zz} region that is not well fit.

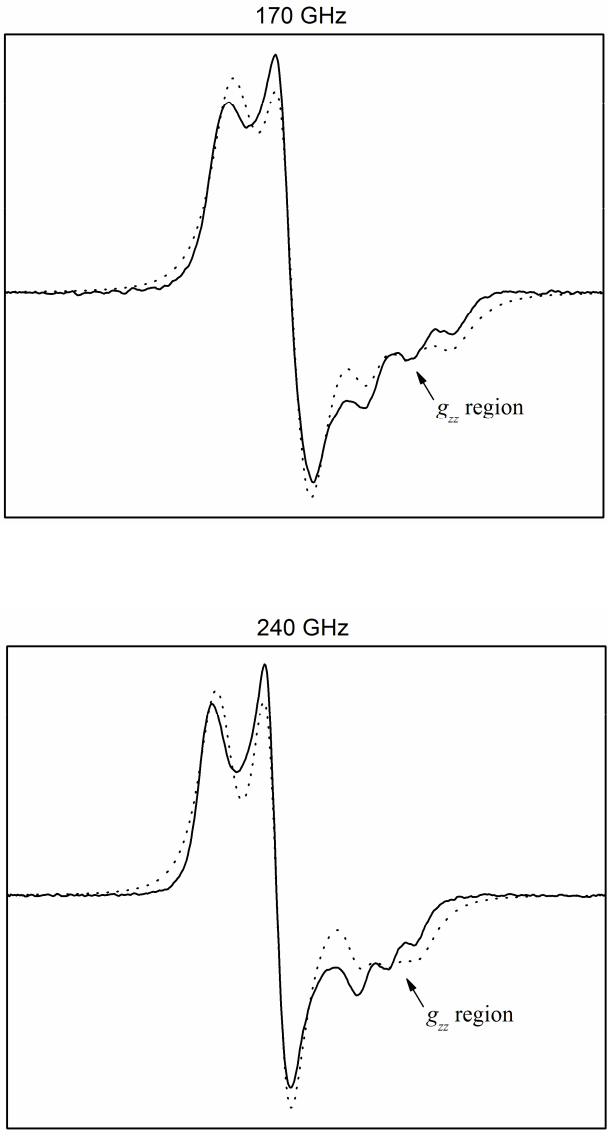

Figure 2-8. The single component fits to the 170 and 240 GHz spectra of 131R2 recorded at 2 ^{o}C; experimental data (solid line), simulations (dashed line). The arrow points to the g_{zz} region that is not well fit.

2.4.4 Temperature Dependence of R^c

The temperature dependence of R^c found for the four mutants in aqueous solution is shown in Figure 2-9. Values obtained for R^c for the four mutants are very close with the exception of 131R1, which is about 20% greater. The average of the values for the four mutants and the standard deviations are given in Table 2-5. Also in this table the average R^c is compared to the value determined by NMR (59) as well as to the diffusion tensor $\boldsymbol{D_o}$ estimated from a hydrodynamic model on the basis of the crystal structure of T4L (67), at 10°C and 25°C respectively. These values were extrapolated to 2, 12, 22, and 32°C using the Stokes-Einstein relation. The values for the average R^c are about 10% below the mean $D_o=(2\,D_{o,\perp}+D_{o,\parallel})/3$, and are about 15% greater than the NMR estimate. These small differences may arise in part from the neglect of the small asymmetry in $\boldsymbol{R^c}$ in the experimental analyses. Note that whereas R^c is varied in the fitting process, it can be fixed to the average value in Table 2-5 and still good fits can be obtained.

2.4.5 Diffusion Tilt Angle (β_d)

The diffusion tilt angle (β_d), as noted in Methods, is related to the conformation of the nitroxide labeled tether. In a previous study on the analysis of the 9 GHz ESR spectra of R1 labeled mutants at solvent exposed sites of T4L, the best fit β_d was found to be 36° (34). In our work, the best fit β_d was determined by fitting the most challenging multifrequency spectra which are those at 2°C. [A few checks at 22°C indicated there was not much temperature dependence of β_d.] For each mutant, we performed separate fits to the multifrequency spectra recorded at 2°C in water solution with β_d fixed to a series of values in the range of 0 to 40°. Variations of the reduced χ^2 with β_d are plotted in Figure 2-10. Variations of the reduced χ^2 (i.e. the sum of χ^2 at all frequencies) and χ^2 at each frequency are tabularized in Table 2-6.

Table 2-5. Comparison of the global tumbling rates of T4 lysozyme from the multifrequency ESR fits, from the NMR estimate, and from the hydrodynamic model calculation

T (^{o}C)	Average R^{c} [a] (10^{7} s^{-1})	Standard Deviation (10^{7} s^{-1})	NMR [b] (10^{7} s^{-1})	$D_{0,\perp}$ [c] (10^{7} s^{-1})	$D_{0,\parallel}$ [c] (10^{7} s^{-1})
2	0.72	0.06	0.63	0.93	0.59
12	1.07	0.13	0.89	1.31	0.83
22	1.33	0.11	1.19	1.75	1.11
32	1.77	0.10	1.54	2.26	1.43

[a] Average R^{c} = (R^{c} of 72R1 + R^{c} of 131R1 + R^{c} of 72R2 + R^{c} of 131R2)/4 (see Table 2-2 for R^{c} of 72R1, 131R1, 72R2, and 131R2).

[b] Calculated from the NMR result at 10^{o}C extrapolated using the Stokes-Einstein relation.

[c] Calculated from $D_{0,\perp}$ and $D_{0,\parallel}$ at 25 ^{o}C (from Table 1 in Reference 67) extrapolated using the Stokes-Einstein relation.

Table 2-6.

Variations of the reduced χ^2 (i.e. the sum of χ^2 at all frequencies) and χ^2 at each frequency with β_d from the best fits to the multifrequency spectra recorded at 2^{o}C in water solution

72 R1 at 2 °C

β_d (o)	0	15	20	21	25	30
χ^2 *	237	245	240	236	252	282
χ^2 9 GHz	51	57	51	52	48	35
χ^2 95 GHz	63	62	50	46	46	33
χ^2 170 GHz	45	41	36	38	51	76
χ^2 240 GHz	78	85	102	100	107	138

131 R1 at 2 °C

β_d (o)	0	15	20	25	30
χ^2	261	264	259	263	279
χ^2 9 GHz	91	93	73	71	77
χ^2 95 GHz	77	83	83	81	77
χ^2 170 GHz	49	43	47	54	62
χ^2 240 GHz	45	45	55	57	63

Table 2-6 (Continued)

72 R2 at 2 ^{o}C

β_d (o)	0	15	25	30	35
χ^2	139	123	105	84	85
χ^2 9 GHz	54	50	39	27	22
χ^2 95 GHz	38	33	28	25	28
χ^2 170 GHz	47	39	38	32	35

131 R2 at 2 ^{o}C

β_d (o)	0	15	25	30	32	35	40
χ^2	288	257	195	166	155	146	150
χ^2 9 GHz	96	96	79	67	60	58	53
χ^2 95 GHz	32	50	41	30	28	23	20
χ^2 170 GHz	71	48	38	37	36	36	44
χ^2 240 GHz	88	63	37	32	31	29	33

* χ^2 (i.e. the reduced χ^2) = $\Sigma \chi^2$ each frequency

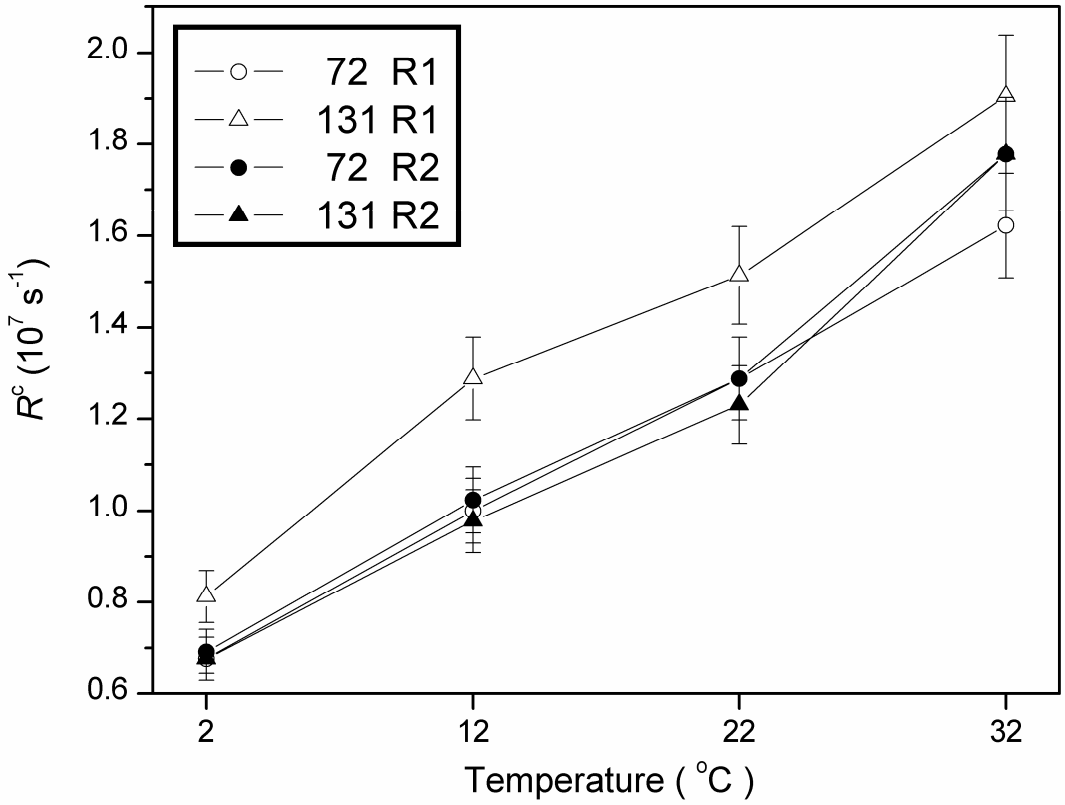

Figure 2-9. The best fit R^c vs temperature from analysis of spectra recorded in water solution (with error bars added).

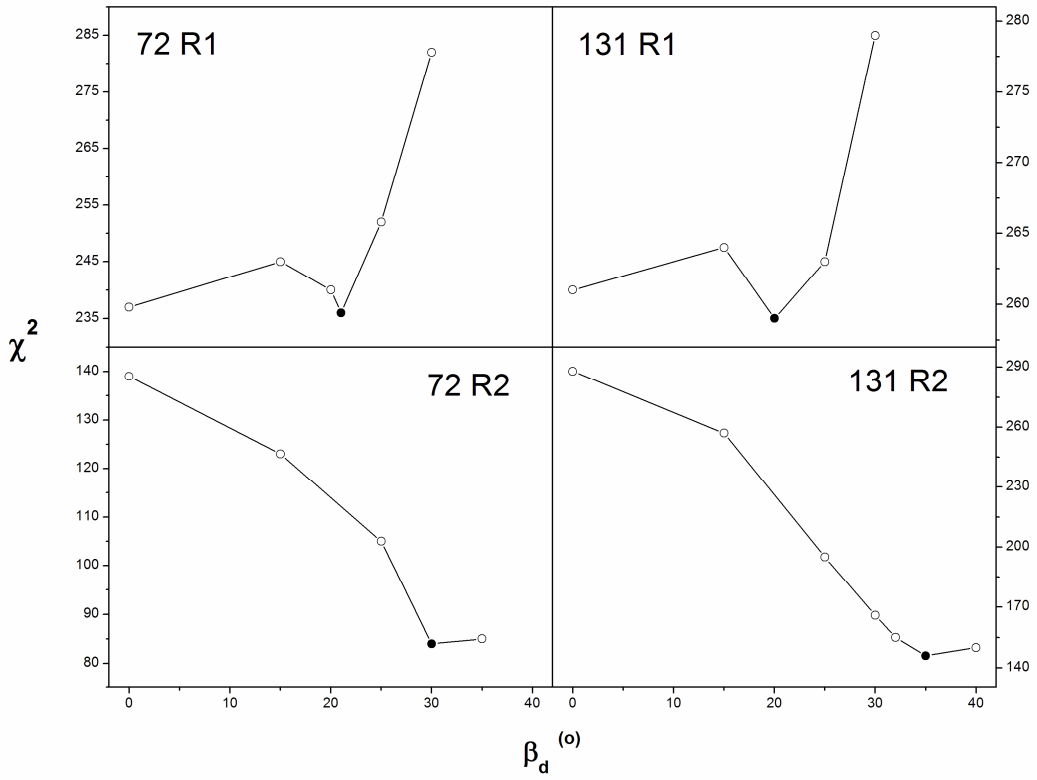

Figure 2-10. The reduced χ^2 from the best fits to the multifrequency spectra recorded at 2 ^{o}C in water solution vs the diffusion tilt angle (β_d); the best fit β_d (●).

For R1, when β_d is increased from 0^o to 25^o, χ^2 at 9 and 95 GHz becomes smaller while χ^2 at 170 and 240 GHz becomes larger. Thus, the sum of χ^2 at all frequencies almost remains same. When β_d is above 25^o, the fit to the 240 GHz spectrum becomes poor and satisfactory fits cannot be obtained for all frequencies with a same set of parameters. For R2, increasing β_d leads to the decrease of χ^2 at each frequency especially χ^2 at 9 GHz. With the best fit β_d (30~35^o), R2's spectra can be well fit with two components (i.e. the immobile and intermediate components). The mobile component which exists when simulating R2's spectra with $\beta_d = 0^o$ is no longer necessary. Anyway, at $\beta_d = 0^o$, the population of the mobile component of R2 is small ($\leq$ 13%) and it is not the dominant component. Thus the two components of R2 are still named as the immobile component and the intermediate component for the purpose of comparison to the three components of R1.

The best fit β_d that yielded the minimum reduced χ^2 was found and listed in Table 2-3 for each mutant. (In the fitting, the β_d was taken as common for all components. To have allowed β_d to vary separately for each component would have introduced too many parameters in the fitting. However, we do note that the value of β_d only affects the intermediate and mobile components but not the immobile one.) Subsequently, β_d was fixed at the value in Table 2-3 when fitting spectra recorded at the other temperatures (12, 22, and 32^oC) and spectra of the mutant in Ficoll solution recorded at 2 to 32^oC [cf. Chapter 3]. Although different values of best fit β_d were found for the four mutants, these values lie within the range of 20 to 35^o. In a previous study, an angle of 20 to 30^o between the rotation axis of χ_4 and the *z*-axis of the magnetic tensor frame was derived from an energy-minimized model of the side chain based on the crystal structure (34). Thus, it would appear that the *z*-axis of the internal diffusion frame is approximately parallel to the rotation axis of χ_4. The other two diffusion tilt angles (α_d and γ_d) were set to zero in the fitting process as noted above.

The spectra were found to be insensitive to α_d and γ_d in a previous paper based on MOMD simulations at 9 GHz (34), and, in addition, their inclusion would have resulted in too many parameters in the fitting.

The effect of β_d on the spectrum is an interesting one. Faster internal modes of motion, will partially average an axial magnetic tensor, such as the ***A*** tensor, so that its effective magnitude is reduced by

$$\left| S_{2,0} \right| \left[\frac{1}{2} \left(3\cos^2 \beta_d - 1 \right) \right],$$

which then must be averaged by the slower overall tumbling (26). Thus, a value of β_d ~30° leads to a value of 5/8 for the expression in brackets, compared to unity for β_d = 0°. This means that for β_d > 0°, the overall tumbling has a reduced effect on the spectrum [cf. 3.3.2.1 and 3.3.2.2]. This is the case for 9 GHz which is dominated by the axial ***A*** tensor, whereas for high frequencies, dominated by the non-axial ***g*** tensor, this is somewhat less the case.

2.4.6 Axially Symmetric R^o vs Rhombic Symmetric R^o

In our work, all the analyses were performed with an axially symmetric internal diffusion tensor. The use of an axially symmetric $\boldsymbol{R}^{\mathbf{o}}$ ($R^o_x = R^o_y = R^o_\perp$ and $R^o_z = R^o_\parallel$) instead of a fully anisotropic $\boldsymbol{R}^{\mathbf{o}}$, ($R^o_x \neq R^o_y \neq R^o_z$) was advanced in a previous paper based on results derived from two frequencies (9 and 250 GHz) fits to the spectra of 72R1 and 131R1 in water solution (28). In that paper, the reduced χ^2 was not found to be significantly improved when a fully anisotropic $\boldsymbol{R}^{\mathbf{o}}$ was used. To verify that an axially symmetric $\boldsymbol{R}^{\mathbf{o}}$ is sufficient, the multifrequency spectra of the four mutants recorded at 2°C in water solution were fit with $\boldsymbol{R}^{\mathbf{o}}$ assumed to be either axially symmetric or fully anisotropic. In these fittings, β_d was fixed to the values in Table 2-3.

The best fit parameters and the reduced χ^2 are listed and compared in Table 2-7 for the two kinds of symmetries. For 72R1, by allowing R^o_x and R^o_y to be different, the fits to the high field spectra are improved with decreased χ^2 at 95, 170, and 240 GHz. The sum of χ^2 at all frequencies is reduced by 17% when $\boldsymbol{R^o}$ is allowed to be fully anisotropic. For 131R1, 72R2, and 131R2, the fits are slightly improved with $\boldsymbol{R^o}$ of rhombic symmetry relative to $\boldsymbol{R^o}$ of axial symmetry. The sum of χ^2 at all frequencies is reduced by 6~12%. The best fit results indicate that, in most cases, the average of R^o_x and R^o_y in the case of rhombic symmetry is close to $R^o\perp$ in the case of axial symmetry, and R^oz is close to $R^o\parallel$. But there are a few exceptions, e.g. $R^o\perp$ in the immobile component of 131R1 is much larger than the average of R^o_x and R^o_y. In addition to the internal diffusion tensor components, the other fitting parameters, including the order parameters and the percentages of the multiple components, were unaffected by the assumption of the axial symmetry in $\boldsymbol{R^o}$. Therefore, to avoid excessive fitting parameters, the internal diffusion tensor was restricted to axial symmetry.

The immobile component of R1 and R2 has almost isotropic $\boldsymbol{R^o}$, whereas the intermediate and mobile components have anisotropic R^o with $R^o\perp$ (R^o_x and R^o_y) much larger than $R^o\parallel$ (R^o_z). In all, for all components of R1 and R2, the relations among $\boldsymbol{R^o}$ tensor components remains no matter which kind of symmetry is assumed for $\boldsymbol{R^o}$ in the simulation. Moreover, the best fit results with rhombic $\boldsymbol{R^o}$ show that R^o_x and R^o_y are very close in the intermediate and mobile components, whereas R^o_y is either close to or larger than R^o_x in the immobile component.

2.5 DISCUSSION

2.5.1 Comparison with Model of Tombolato et al.

One of the results of this work is that we find three components different in

Table 2-7.

The best fit parameters and the reduced χ^2 from fitting the multifrequency spectra recorded at 2 ^{o}C in water solution with two kinds of symmetries of $\boldsymbol{R^{o}}$

72 R1 at 2 °C

Symmetry of R^o	**Axial** ($R^o\perp = R^ox = R^oy$ and $R^o\parallel = R^oz$)			**Rhombic** (R^ox , R^oy and R^oz)		
β_d (o)	25			24		
R^c (10^7 s^{-1})	0.50			0.58		
Component	Immobile	Intermediate	Mobile	Immobile	Intermediate	Mobile
R^ox (10^7 s^{-1})	4.1	38.9	49.0	2.8	38.9	55.0
R^oy (10^7 s^{-1})				4.6	43.7	47.9
$(R^ox + R^oy)$ / 2 (10^7 s^{-1})	4.1	38.9	49.0	3.7	41.3	51.4
$(R^ox - R^oy)$ / 4 (10^7 s^{-1})	0	0	0	-0.5	-1.2	1.8
R^oz (10^7 s^{-1})	2.6	0.2	0.3	2.5	0.2	0.3
S_{20}	0.64	0.59	0.44	0.64	0.58	0.43
S_{22}	0.01	-0.15	-0.3	0.01	-0.17	-0.31
Population (%)	27	41	32	25	48	27
χ^2 9 GHz	48			50		
χ^2 95 GHz	46			35		
χ^2 170 GHz	51			39		
χ^2 240 GHz	107			84		
χ^2 *	252			208		

Table 2-7 (Continued)

131 R1 at 2 °C

Symmetry of R^o	**Axial**($R^o\perp = R^ox = R^oy$ and $R^o\parallel = R^oz$)			**Rhombic** (R^ox , R^oy and R^oz)		
β_d (o)	25			25		
R^c (10^7 s^{-1})	0.79			0.79		
Component	Immobile	Intermediate	Mobile	Immobile	Intermediate	Mobile
R^ox (10^7 s^{-1})	3.3	45.7	38.9	2.5	47.9	38.9
R^oy (10^7 s^{-1})				7.2	38.9	37.2
$(R^ox + R^oy) / 2$ (10^7 s^{-1})	3.3	45.7	38.9	4.9	43.4	38.0
$(R^ox - R^oy) / 4$ (10^7 s^{-1})	0	0	0	-1.2	2.2	0.4
R^oz (10^7 s^{-1})	3.7	1.4	0.2	3.0	1.9	0.6
S_{20}	0.6	0.5	0.2	0.6	0.51	0.2
S_{22}	-0.02	-0.19	0.32	-0.01	-0.19	0.3
Population (%)	15	60	25	17	58	25
χ^2 9 GHz	71			72		
χ^2 95 GHz	81			73		
χ^2 170 GHz	54			47		
χ^2 240 GHz	57			54		
χ^2	263			246		

Table 2-7 (Continued)

72 R2 at 2 ^{o}C

Symmetry of R^o	**Axial** ($R^o\perp = R^ox = R^oy$ and $R^o\parallel = R^oz$)		**Rhombic** (R^ox , R^oy and R^oz)	
β_d (o)	30		30	
R^c (10^7 s^{-1})	0.69		0.69	
Component	Immobile	Intermediate	Immobile	Intermediate
R^ox (10^7 s^{-1})	4.3	33.1	4.8	32.4
R^oy (10^7 s^{-1})			4.7	38.0
$(R^ox + R^oy) / 2$ (10^7 s^{-1})	4.3	33.1	4.7	35.2
$(R^ox - R^oy) / 4$ (10^7 s^{-1})	0	0	0.0	-1.4
R^oz (10^7 s^{-1})	3.9	2.1	3.7	2.3
S_{20}	0.65	0.57	0.68	0.55
S_{22}	-0.01	-0.09	-0.01	-0.11
Population (%)	73	27	73	27
χ^2 9 GHz	27		24	
χ^2 95 GHz	25		22	
χ^2 170 GHz	32		27	
χ^2	84		74	

Table 2-7 (Continued)

131 R2 at 2 ^{o}C

Symmetry of R^o	**Axial** ($R^o\perp = R^ox = R^oy$ and $R^o\parallel = R^oz$)		**Rhombic** (R^ox , R^oy and R^oz)	
β_d (o)	32		31	
R^c (10^7 s^{-1})	0.65		0.74	
Component	Immobile	Intermediate	Immobile	Intermediate
R^ox (10^7 s^{-1})	8.7	38.0	5.8	43.7
R^oy (10^7 s^{-1})			12.9	42.7
$(R^ox + R^oy) / 2$ (10^7 s^{-1})	8.7	38.0	9.3	43.2
$(R^ox - R^oy) / 4$ (10^7 s^{-1})	0	0	-1.8	0.2
R^oz (10^7 s^{-1})	2.0	4.4	2.5	1.9
S_{20}	0.68	0.57	0.68	0.56
S_{22}	-0.03	0.03	-0.07	0.05
Population (%)	55	45	51	49
χ^2 9 GHz	60		59	
χ^2 95 GHz	28		31	
χ^2 170 GHz	36		30	
χ^2 240 GHz	31		22	
χ^2	155		142	

* χ^2 (i.e. the reduced χ^2) = Σ χ^2 each frequency

their internal mobility when simulating the spectra of R1. One is a highly ordered relatively immobile component, and the other two are relatively weakly ordered components referred to as the intermediate and the mobile components with comparable rotational diffusion rates ($R^{o}_{\perp}$) but significantly different orderings (S_{20}). The finding of three components in R1's spectra is in good agreement with a theoretical study of the conformational dynamics of R1 at the solvent exposed helical site 72 of T4L by Tombolato et al. (67). According to that study, the multi-component character is an intrinsic feature of the spectra of R1 and at least three components are necessary in the simulation. The values of S_{20} they obtained for their three components were 0.68, 0.52, and 0.37 when simulating the 9 GHz spectrum of 72R1 at 10°C. Correspondingly, we obtained three components with S_{20} = 0.64, 0.58, and 0.45 from the fits to the multifrequency spectra of 72R1 at 12°C. It followed from the conformational dynamics study that the two relatively mobile components originate from the same conformers but with different torsional distributions about the minima in the energy profile for rotation about χ_5 (67). This would explain why the two relatively mobile components that we find differ from each other in ordering.

As noted in Results, the immobile component has almost isotropic $\boldsymbol{R^{o}}$ and its mobility is similar at site 72 and site 131. In a previous multifrequency ESR study of T4L dynamics, an immobile component was also found when simulating the spectra of R1 linked to another two solvent exposed helical sites (44 and 69), and its mobility was found to be similar at these two sites as well (6). The existence of such an immobile component at solvent exposed helical sites was ascribed to a weak interaction of the nitroxide ring with the protein surface by Columbus et al. (34). According to Tombolato et al., the change of spectral lineshape with increasing temperature arises from increasing global tumbling and increasing internal mobility of each component, whereas the population of each component remains unchanged (67).

However, our results show that the population of each component does vary with temperature and the population of the immobile component decreases with increasing temperature. Our results are supported by molecular modeling which have suggested that the conformers corresponding to immobile components are entropically unfavored, and a weak interaction is necessary to stabilize them (37). The interaction is so weak that it exists only at reduced temperature, so that the immobile component becomes more abundant at lower temperatures (34).

In this study, we discerned two components in the spectra of R2, which, compared to the three components in the case of R1, allow for a simpler description of the dynamics of R2. Tombolato et al. found, that the spectrum of 72R2 is composed of similar spectra of a series of conformers, so that the spectrum of R2 can be simulated with a single component (67). Additionally, they suggested that the spectrum of R2 is not far from a rigid limit spectrum with partially averaged magnetic tensors. Our results indicate that, in addition to an immobile component, which yields a spectrum similar to the rigid limit case, a more mobile component, referred to as the intermediate component in this paper, also exists. We found that the spectra of R2 have some features in common with those of R1: (1) There is a highly ordered immobile component; (2) The intermediate component has an anisotropic $\boldsymbol{R}^{\mathbf{0}}$ and relatively lower ordering. Fleissner et al. obtained the same crystal structure for 131R1 and 131R2 (37). This may help to explain why the spectra of R1 and R2 share such common features.

2.5.2 Effects of Added Methyl Group in R2

Now we wish to discuss the change of spectral lineshape when a methyl group substitutes the hydrogen atom at the 4-position of the nitroxide ring of R1, i.e. when R2 is linked to the mutant. On the basis of the molecular modeling described by

Columbus et al., it was suggested that the 4-substituent increases the ordering because of the steric clash with the disulfide which reduces the amplitude of rotation about χ_5 (34). This is consistent with our current results that 72R2 and 131R2 have more highly ordered components than 72R1 and 131R1 respectively. For example, the value of S_{20} in the intermediate component of 72R2 is higher than the average of S_{20} in the two relatively mobile components of 72R1. Similarly, the value of S_{20} in the intermediate component of 131R2 is higher than both order parameters in the two relatively mobile components of 131R1. At both sites, the larger population of the immobile component of R2 compared to R1 can be caused by the stronger interaction between R2 and the protein surface because of the additional methyl group (34). As previously noted (34), with the 4-methyl group the interaction between the nitroxide ring and its nearby residues is evident in the 9 GHz spectrum of 131R2 recorded at room temperature in 30% sucrose solution, whereas such an interaction cannot be clearly observed in the spectrum of 131R1 at room temperature. Such observations are further confirmed by our quantitative analysis showing that the immobile component, stabilized by such interaction, is more populated in the spectra of R2 than in those of R1.

2.5.3 $R^o_\perp$ vs $R^o_\parallel$

According to our results, it is shown that $R^o_\perp > R^o_\parallel$ in the two relatively mobile components of R1 and in the intermediate component of R2. As noted in Results, $R^o_\parallel$ is roughly parallel to χ_4, and as suggested by Columbus et al. (34), $R^o_\perp$ is in the plane of the nitroxide ring where χ_5 lies. Liang et al. also observed that $R^o_\perp$ in the dominant component of 72R1 and 131R1 is an order of magnitude larger than $R^o_\parallel$ in their two-frequency study (28). Also, Barnes et al. obtained $R^o_\perp > R^o_\parallel$ by nearly a factor of 10 from their two frequency study of 44R1 and 69R1 at 9 and 250 GHz (6). Such a relation between $R^o_\perp$ and $R^o_\parallel$ indicates that the rotation about χ_5 is the major

contributor to the fast conformational transitions in the relatively mobile components of R1 and R2. That the rotation about χ_5 is the fastest rotation has been shown by studies using various methods by Mchaourab et al., Budil et al., Tombolato et al., and Sezer et al. (10, 66, 67, 68). Moreover, simulation of the 9 GHz spectrum of 41R1 in terms of the MOMD model yielded a mobile component with anisotropic $\boldsymbol{R}^{\mathbf{0}}$ and an immobile component with isotropic $\boldsymbol{R}^{\mathbf{0}}$, that is in general agreement with our observations (76).

2.5.4 Dynamics at Site 72 vs Site 131

We have shown in our present work that the difference in the spectra of mutants at site 72 and at site 131 does not result from any difference in the magnetic tensors, since they are identical, but rather it arises from differences in their dynamics. What then is the source of the spectral difference at these two sites? Both sites were defined as solvent exposed helical sites (10). It is shown that they have no interaction with their local environment by the fact that their spectral lineshapes are independent of $i\pm3$ and $i\pm4$ mutations to alanine (10). In light of this, Columbus et al. (34) and Liang et al. (28) hypothesized that the backbone mobility, which is different at these two sites because of their attachment to helices of different length and rigidity, is responsible for the lineshape difference at these two sites. Site 72 is located in the middle of a long 5-turn helix and is thought to be one of the most highly ordered helical surface sites (6, 10, 34). Site 131 is on a short 2.5-turn helix and is more flexible in terms of higher Debye-Waller factors and hydrogen exchange rates when compared to site 72 (34). Tombolato et al. found that the spectra of 131R1 could not be simply obtained by adjusting the populations of the three components obtained from the simulation of 72R1's spectra. (They only developed their theoretical model only for the 72 site and not for the 131 site.) Thus they postulated that the backbone

dynamics is most likely the main reason for the observed difference between the spectra of 72R1 and 131R1, supporting the hypothesis suggested by Columbus et al. and Liang et al (28, 67). It was noted by Columbus et al. (34) that the immobile component, which is common in the spectra of both R1 and R2, most likely arises from the interactions of the nitroxide ring with the protein surface. Thus, it does not directly reflect the modulation of the internal motion by the backbone dynamics (60). On the other hand, the conformers corresponding to the intermediate and the mobile components were modeled to have no interaction with the surrounding residues (37). Thus, they can be used to infer the backbone motion.

R2 has been suggested by Columbus et al. to be a useful probe for the backbone dynamics because the steric clash of the 4-methyl group with the disulfide constrains rotations about the side chain bonds (e.g. χ_5), resulting in the enhanced sensitivity to the backbone dynamics (34). Since the mobility of R2 is restricted by interaction within the side chain itself rather than by interaction with its local environment, R2 can be used to monitor the backbone dynamics even more readily than R1.

Our results show that, for the intermediate component of R2, the values of S_{20} at the two sites of 72 and 131 are similar. However, for both the intermediate and the mobile components of R1, the values of S_{20} at the two sites are significantly different. Such an inconsistency raises the question whether the backbone dynamics does account for the spectral difference at the two sites, or whether R1 and R2 can both be used to probe the backbone dynamics. Sezer et al. found from their molecular dynamics simulations that the most populated conformers of 72R1 are well localized, and in contrast, the most populated conformers of 131R1 are more diffuse (68). Taken together, our results suggest that the backbone motion may not be the major contributor to the lineshape difference at these two sites, if we take as given the

assumption that R2 can probe the backbone mobility. It is however possible that the conformers corresponding to the intermediate component of R2 have some interactions with the local environment. If this were the case, then the differences in the ESR spectra of 72R1 and 131R1 might be reflecting the differences in their backbone motion as suggested by Columbus et al. and Tombolato et al. (34, 67).

As noted above, Mchaourab et al. pointed out that there was no tertiary interaction at solvent exposed helical sites including site 72 and site 131, with negligible change in spectral lineshape upon $i\pm3$ and $i\pm4$ mutation to alanine (10). Guo et al. showed that there are interactions with the neighboring side chains at some solvent exposed helical sites, e.g. site 41 and site 44 (76). However, it was shown in that study that such interactions are most likely occurring for the immobile component. In contrast, Sezer et al. found from their analysis of molecular dynamics simulations the presence of significant hydrophobic interactions of the spin label with alanine (77, 78, 79). They suggested that the variation in spectra at solvent exposed helical sites results from the difference in the ability of R1 to engage in the hydrophobic interactions with the helix (77). Thus, according to the molecular dynamics simulation results, site 72 and site 131 can both interact with surrounding residues and the difference in their spectral features may not be simply related to the backbone dynamics. Clearly this is a different view-point than that of the experimental studies referred to above.

However for 72R2 vs 131R2, the S_{20} values for the "intermediate" component are similar, a result which might not be expected if the difference between the sites is due to backbone motions. It is self evident that the motion of R1 will reflect particular modes of backbone flexibility on the ns time scale. For example, the studies of Columbus et al. clearly revealed the highly flexible backbone segments of GCN4 (60) that were previously identified by NMR relaxation. Hence, SDSL will be a powerful

tool in identifying "intrinsically disordered" domains in proteins using a similar approach. However, uncertainty remains as to the origin of relatively small differences in R1 motion, such as that between 72R1 and 131R1.

2.6 CONCLUSIONS

The main findings are the following:

(1) Best global fits to a SRLS model using data from four frequencies on T4 lysozyme in aqueous solution require three spectral components characterized as relatively "mobile", "intermediate", and "immobile" for both 72R1 and 131R1. In the case of 72R2 and 131R2 only the "intermediate" and "immobile" components are found.

(2) For R1, three components are found. Liang et al. could not simultaneously fit the 9 and 250 GHz spectra of R1 at or below room temperature using the same set of parameters (28). They utilized a two-component fit and required different fractional amounts at the two frequencies. We show in the present work that by including three components in the fitting we can simultaneously fit all spectra at the four frequencies with the same parameters.

(3) For R2, just two components may be discerned. One of the two components, highly ordered and with slow isotropic R^{o}, is also present in R1's spectra, referred to as the "immobile" component. This component may correspond to conformers stabilized by interaction with the protein surface. The fraction of this component for R2 is higher than it is for R1, ostensibly because the interaction of the nitroxide ring with the protein surface is stronger in the case of R2 due to the additional 4-methyl group.

(4) The “mobile” and “intermediate” components exhibit fast anisotropic local diffusion and relatively low ordering. They most likely correspond to conformers having little or no interactions with nearby residues.

(5) In all cases, for the spectra at all four frequencies, very good simultaneous fits were achieved at all temperatures with the SRLS model.

(6) The more mobile components of 72R1 and 131R1 exhibit significantly different S_{20} values, with that for 72R1 being significantly greater, as is consistent with previous studies which suggested that this difference results from reduced backbone flexibility for 72R1.

(7) A comparison between the results for 72R1 vs 131R1 and 72R2 vs 131R2, renders uncertain the suggestion by Columbus et al. that the backbone dynamics is the major contribution to the spectral difference at site 72 and site 131 (34).

(8) The values for overall tumbling rate, R^c obtained independently from each of the four spin labeled mutants were generally in very good agreement with each other and agree favorably with estimates from NMR and hydrodynamic modeling. This supports the results of the SRLS analysis.

(9) The experimental results, and their SRLS analysis, show some key similarities with the predictions of Tombolato et al. from their dynamic modeling, but the relationship to the results of the MD simulations by Sezer et al. is more tenuous.

2.7 IMPLICATIONS

We wish now to make an overall assessment of this study and its implications. Clearly the multifrequency approach provides substantial information to study the complex dynamics of a protein such as T4L. Not only do the different frequency spectra supply "snapshots" at different time scales of the dynamics, (i.e. higher

frequencies give faster time-scale insights and lower frequencies slower ones), but they also provide "snapshots from different angles". That is, the lower frequency spectra are mostly influenced by the nearly axially symmetric hyperfine tensor, for which the *z*-component is dominant, whereas the high frequency spectra are most influenced by the fully asymmetric ***g*** tensor wherein both the *x* and *z* components differ substantially from its trace. Thus, whereas motion about an axis parallel to the magnetic *z*-axis is difficult to discern at 9 GHz, it is very clear at the high frequencies, as are motions relative to the other magnetic axes (80). Taken together, these features emphasize the value of the multifrequency approach to study molecular dynamics.

On the other hand, when dealing with dynamics as complex as displayed in the present study on T4L, the substantial independent experiments provided in this study are not in themselves guarantors of sufficient information to disentangle all the complex features. This is a primary reason that we analyzed the data in the context of what we refer to as a "mesoscopic" model, viz. the SRLS model. The SRLS model, which distinguishes internal and overall motions, but does allow for several components, already provides numerous parameters to fit to the experimental spectra. We have found it necessary to restrict somewhat the parameters that we chose to fit, hopefully in a reasonable manner, as we have discussed above. Clearly, further efforts at sharpening up the model for fitting these spectra would be of value, but one must be wary of introducing too many fitting parameters.

Recent efforts at improved models include that of Tombolato et al. (67), which adds an atomistic viewpoint to the SLE. We have compared the results of our SRLS analysis of the experimental results with their predictions and find that our approach, with as many as three components, is consistent with their predictions, even in the characteristics of these components. However, the analysis provided by Tombolato et al clearly shows that the side chain motion of the MTSSL tether is significantly more

complex than the internal motional modeling that SRLS allows. (For example, the motion about the five dihedral angles, each with its own effective tilt angle and motional rate, leads to fully asymmetric partially averaged hyperfine and g-tensors with as many as five components each, whereas our SRLS analysis just allows for a single effective internal mode with an $R_{\|}$, $R_{\perp}$, and β_{d} which preserve more of the symmetry of the magnetic tensors.) Thus the SRLS approach, as intended, must be regarded in the mesoscopic sense of replacing the actual detailed internal motions of the MTSSL tether by a single effective set of internal motional parameters. Tombolato et al only considered the 9 GHz spectra of 72R1 and 72R2, but indicated how to extend their analysis to the higher frequency spectra.

The fully atomistic viewpoint provided by the MD study of Sezer et al. (68) is more difficult to reconcile with our multifrequency study and analysis, even though they succeeded admirably in fitting several of the multifrequency results (at room temperature) that form a part of our present extensive study. Their MD study emphasizes the detailed complexities of a fully atomistic viewpoint, much of which are not resolvable in actual experiments. Sezer et al also provide explicit evidence that even successful fitting to extensive multifrequency spectra is not in itself a guarantor of uniqueness of fit.

This MD study does make clear, as did the work of Tombolato et al, that there are generally several groups of interchanging MTSSL conformers, which will lead to the spectral presence of more than one component, both for 72R1 and 131R1. However, their assignment of the relevant conformers proved to be somewhat different from those of Tombolato et al., most likely due in part to the fact that the MD analysis showed cooperative side chain adjustments and motions that could overcome steric barriers, whereas Tombolato et al. allowed only independent single bond motions. The MD study indicated that there is a subtle interplay in the energetics of

the nitroxide moiety with its amphiphilic character in determining the relative populations of the different conformers and their interactions with the backbone; it would be of interest to see how small variations in the interaction potentials would affect these populations and their motional dynamics.

In general, the studies of Tombolato et al. (67) and Sezer et al. (68) do emphasize the very important role that motion of the MTSSL side chain plays in the ESR spectra. This presents a difficulty in extracting out information on backbone dynamics. Tombolato et al. only included the side chain and the overall protein motion in their fitting to the 9 GHz spectra, whereas any backbone motion is implicit in the MD simulations, and further efforts would need to be made to extract them out. Our present and past multifrequency experimental studies could not clearly distinguish between the conformational motions of the side chain and local backbone motions. The proposed interpretation that the difference in multifrequency spectra between 72R1 and 131R1 is due to the more locally rigid position of the former, while an appealing one, is not confirmed in the present study nor is it ruled out. It may, in fact, be that the local side chain dynamics is coupled to local backbone fluctuations, such that any motion in the latter more restricted motion, may induce larger side chain fluctuations with their lower potential barriers. We note that extensive studies at 9 GHz on mutants labeled at many sites of T4L are consistent with the sensitivity of the ESR spectra to backbone dynamics (10, 34, 60, 81). It would clearly be of value to extend the multi-frequency approach to several more of these mutants.

CHAPTER 3

STUDY OF FICOLL'S EFFECT ON T4 LYSOZYME 'S DYNAMICS

3.1 INTRODUCTION

Ficoll 70 is a macromolecule with an approximate molecular weight of 70000 daltons, which is about 4 times the molecular weight of T4L. To better distinguish between the slower global tumbling and the faster internal motion, Ficoll was added into aqueous solution to different concentrations in order to increase the viscosity of the solution and slow down the global tumbling of the protein.

3.2 EXPERIMENTAL

The concentration of protein in each sample is between 1 and 2 mM. Ficoll 70 was purchased from Amersham Biosciences (now GE Healthcare Life Sciences), and was used without further purification.

Multifrequency spectra of the five samples listed in Table 3-1 were taken at 2, 12, 22, and 32 ^{o}C. The phase of the experimental spectra at 95, 170, and 240 GHz was adjusted to correct for a small admixture of dispersional signal, according to the procedure described previously (70).

3.3 RESULTS

3.3.1 Ficoll's Effect on the Global Tumbling and the Internal Motion

The experimental and the fitted spectra of 131R1, 72R2, and 131R2 in 15 and

Table 3-1. The nitroxide labeled T4 lysozyme samples for multifrequency ESR study in Ficoll solutions

Sample No.	Mutant Site	Spin Label	Ficoll Concentration (w/v %)	Frequency (GHz)			
				9	95	170	240
1	131	R1	25	√ [a]			√
2	72	R2	15	√	√	√	
3	72	R2	25	√	√	√	
4	131	R2	15	√	√	√	
5	131	R2	25	√	√	√	√

[a] A √ indicates the ESR spectrum has been recorded.

25 w/v% Ficoll solutions (samples 1 to 5 in Table 3-1) at 2, 12, 22, and 32°C are compared in Figure 3-1, showing very good agreement. The best fit parameters are listed in Table 3-2. The values of $R^{o}_{\perp}$, S_{20}, and the percentages of the components vs temperature in different concentrations of Ficoll solutions (0, 15, and 25 %) are displayed and compared in Figure 3-2. It is found that the spectra of each mutant in 0, 15, and 25 % Ficoll solutions cannot be fit well with the same set of internal dynamic and ordering parameters with just different global tumbling rates (R^{c}). Therefore, the spectra with different Ficoll concentrations were fit separately, and the parameters derived from the best fits were compared to determine which are influenced by the addition of Ficoll.

The macroscopic viscosity of Ficoll solution and the microscopic viscosity for the global tumbling of T4L calculated from R^{c} are compared in Table 3-3. It was shown by Lavalette et al. (82) that the linear viscosity dependence of the Stokes-Einstein relation should be replaced by a power law to describe the rotational diffusion of proteins in a macromolecular environment. This can explain the significant difference between the values of the macroscopic and microscopic viscosities in Table 3-3. In fact, we find $\eta(\text{micro}) \propto [\eta(\text{macro})]^{0.39}$. The temperature dependence of the microscopic viscosity is shown in Figure 3-3.

The spectra recorded in Ficoll solution were fit with three components for R1 and with two components for R2. The population distributions are close to those in water solution with difference within only 10%. Comparison of R2's motion in different concentrations of Ficoll solutions shows that adding Ficoll has little effect on $R^{o}_{\perp}$ of the intermediate component, whereas it has a small influence on the ordering of this component. The most notable effect after adding Ficoll is that the value of $R^{o}_{\perp}$ in the immobile component is reduced. Ratios of rotational diffusion rates (R^{c}, $R^{o}_{\perp}$ in the

Table 3-2.

Best fit parameters of nitroxide labeled T4 lysozyme in 15 and 25 w/v% Ficoll solutions

Mutant	T (°C)	Comp.	$R^{o}_{\perp}$ (10^7 s^{-1})	$R^{o}_{\parallel}$ (10^7 s^{-1})	c_{20}	c_{22}	S_{20}	S_{22}	Popu.	R^{e} (10^7 s^{-1})	W_9 (G)	W_{95} (G)	W_{170} (G)	W_{240} (G)
131 R1 in 25% Ficoll	2	1	3.55	2.00	3.10	-0.02	0.62	0.00	0.24	0.12	1.14			2.79
		2	46.8	0.69	2.80	-1.42	0.51	-0.17	0.52					
		3	37.2	0.63	1.10	-0.35	0.24	-0.09	0.24					
	12	1	4.47	1.91	3.03	0.07	0.61	0.01	0.17	0.23	1.02			4.26
		2	50.1	0.79	2.72	-1.46	0.49	-0.18	0.60					
		3	49.0	0.79	1.08	-0.07	0.24	-0.02	0.23					
	22	1	4.68	1.78	2.87	-0.07	0.59	-0.01	0.10	0.41	0.87			4.37
		2	51.3	1.55	2.63	-1.38	0.48	-0.18	0.57					
		3	46.8	0.79	1.20	0.04	0.27	0.01	0.33					
	32	2	58.9	2.51	2.56	-1.52	0.46	-0.21	0.71	0.60	0.85			4.52
		3	60.3	1.00	1.20	0.81	0.23	0.21	0.29					
72 R2 in 15% Ficoll	2	1	2.69	2.82	3.43	-0.32	0.66	-0.02	0.65	0.17	0.70	0.56	1.46	
		2	33.9	2.04	3.29	-1.03	0.62	-0.09	0.35					
	12	1	4.07	3.80	3.42	-0.28	0.65	-0.02	0.62	0.35	0.62	0.46	1.85	
		2	40.7	2.40	3.13	-0.85	0.60	-0.08	0.38					
	22	1	6.03	4.90	3.41	-0.07	0.65	-0.01	0.48	0.63	0.64	0.75	1.73	
		2	45.7	3.31	3.10	-0.77	0.60	-0.07	0.52					
	32	1	8.32	6.31	3.30	-0.39	0.64	-0.03	0.40	0.91	0.57	1.09	1.38	
		2	51.3	5.01	3.03	-0.61	0.60	-0.06	0.60					

Estimated errors: $R^{o}_{\perp} \leq 7\%$, $R^{o}_{\parallel} \leq 17\%$; $c_{20} \leq 5\%$; $S_{20} \leq (\pm 0.02)$, $S_{22} \leq (\pm 0.05)$; Popu $\leq (\pm 0.05)$; $R^{c} \leq 7\%$.

Table 3-2 (Continued)

	2	1	1.91	2.24	3.49	-0.62	0.66	-0.05	0.65	0.10	0.63	0.67	1.79	
		2	33.9	1.66	3.35	-1.17	0.62	-0.10	0.35					
72 R2 in 25% Ficoll	12	1	2.75	2.75	3.45	-0.43	0.66	-0.03	0.58	0.20	0.65	0.91	1.94	
		2	38.0	2.82	3.31	-1.01	0.62	-0.09	0.42					
	22	1	3.98	3.89	3.40	0.06	0.65	0.01	0.50	0.38	0.63	0.97	2.08	
		2	44.7	2.82	3.30	-1.00	0.62	-0.08	0.50					
	32	1	5.50	4.37	3.30	-0.50	0.64	-0.04	0.39	0.50	0.61	1.24	2.08	
		2	51.3	5.37	3.19	-0.60	0.62	-0.05	0.61					
	2	1	6.03	1.35	3.74	-0.69	0.68	-0.04	0.63	0.21	0.75	1.13	3.70	
		2	42.7	7.08	2.97	0.33	0.60	0.03	0.37					
131 R2 in 15% Ficoll	12	1	7.08	1.62	3.72	-0.62	0.68	-0.04	0.49	0.43	0.70	1.03	3.59	
		2	46.8	3.89	2.80	0.11	0.58	0.01	0.51					
	22	1	10.0	1.70	3.66	-1.16	0.66	-0.08	0.44	0.65	0.63	1.65	2.75	
		2	58.9	4.37	2.77	0.36	0.57	0.04	0.56					
	32	1	12.9	2.19	3.64	-1.27	0.65	-0.09	0.40	1.00	0.55	1.50	2.53	
		2	69.2	7.41	3.01	0.93	0.58	0.09	0.60					
	2	1	4.07	1.07	3.75	-0.77	0.68	-0.05	0.65	0.11	0.83	1.28	3.36	3.71
		2	41.7	3.02	2.98	0.31	0.60	0.03	0.35					
131 R2 in 25% Ficoll	12	1	4.57	1.70	3.70	-1.19	0.66	-0.08	0.49	0.21	0.79	1.40	2.79	3.56
		2	50.1	2.88	2.84	-0.05	0.58	-0.01	0.51					
	22	1	5.37	1.66	3.68	-1.07	0.66	-0.07	0.46	0.42	0.63	1.36	3.01	3.91
		2	58.9	2.51	2.82	-0.01	0.58	0.00	0.54					
	32	1	6.61	2.19	3.68	-1.78	0.62	-0.13	0.40	0.58	0.54	1.48	2.55	4.39
		2	67.6	3.47	2.86	0.33	0.58	0.04	0.60					

Table 3-3. Comparison of the macroscopic and the microscopic viscosities of 15 and 25 w/v% Ficoll solutions

Ficoll Concentration (w/v %)	Macroscopic Viscosity at 20 °C [a]	Microscopic Viscosity at 22 °C [b]
15	5.6	2.05
25	16.6	3.39

[a] Relative viscosity of solutions of Ficoll 70 from product information sheet provided by Amersham Biosciences (now GE Healthcare Life Sciences).

[b] The microscopic viscosity with regard to the global tumbling of T4 lysozyme. Values were determined by dividing R^c of 72R2 in water solution (see Table 2-2) by R^c of 72R2 in Ficoll solution (see Table 3-2).

Figure 3-1.

The multifrequency ESR spectra of 72R1, 131R1, 72R2, and 131R2 recorded in 15 and 25 w/v% Ficoll solutions at 2, 12, 22, and 32 ^{o}C; experimental data (solid line), simulations (dashed line).

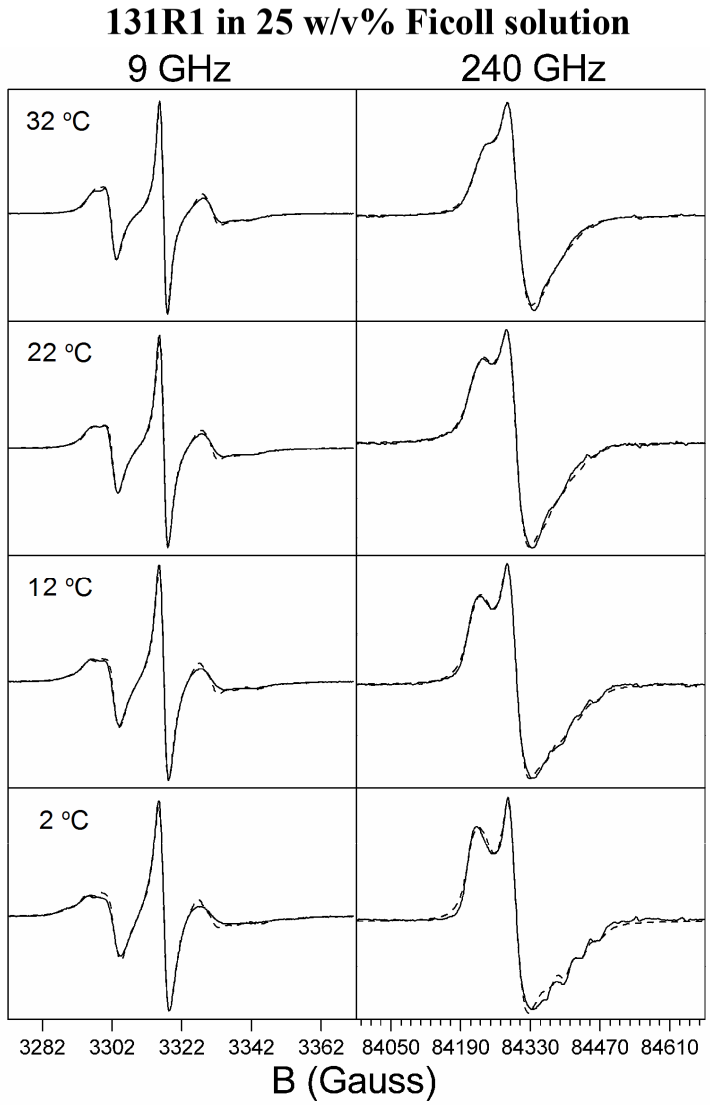
131R1 in 25 w/v% Ficoll solution
9 GHz
240 GHz
32 °C
22 °C
12 °C
2 °C
3282
3302
3322
3342
3362
84050
84190
84330
84470
84610
B (Gauss)

Figure 3-1 (Continued)

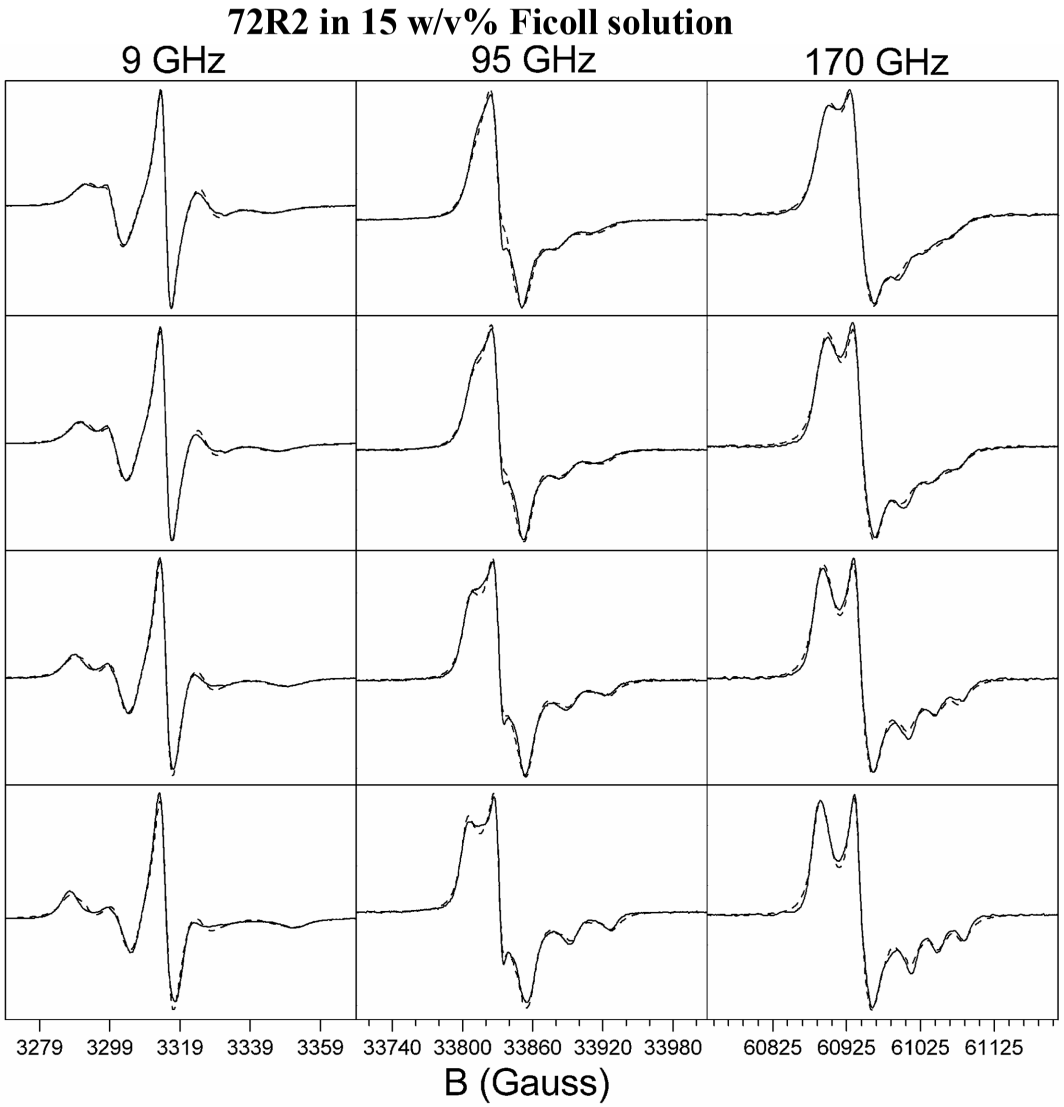

Figure 3-1 (Continued)

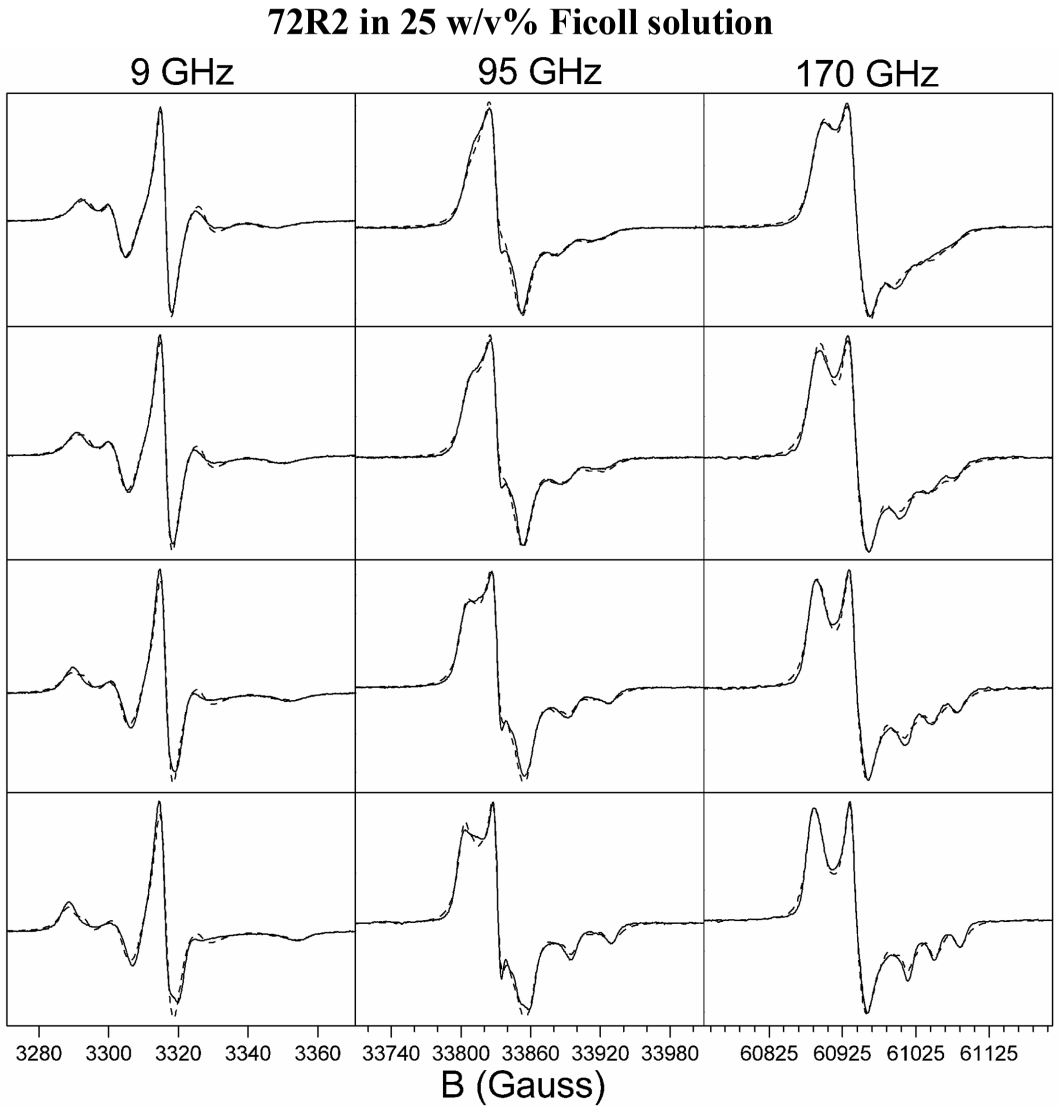

Figure 3-1 (Continued)

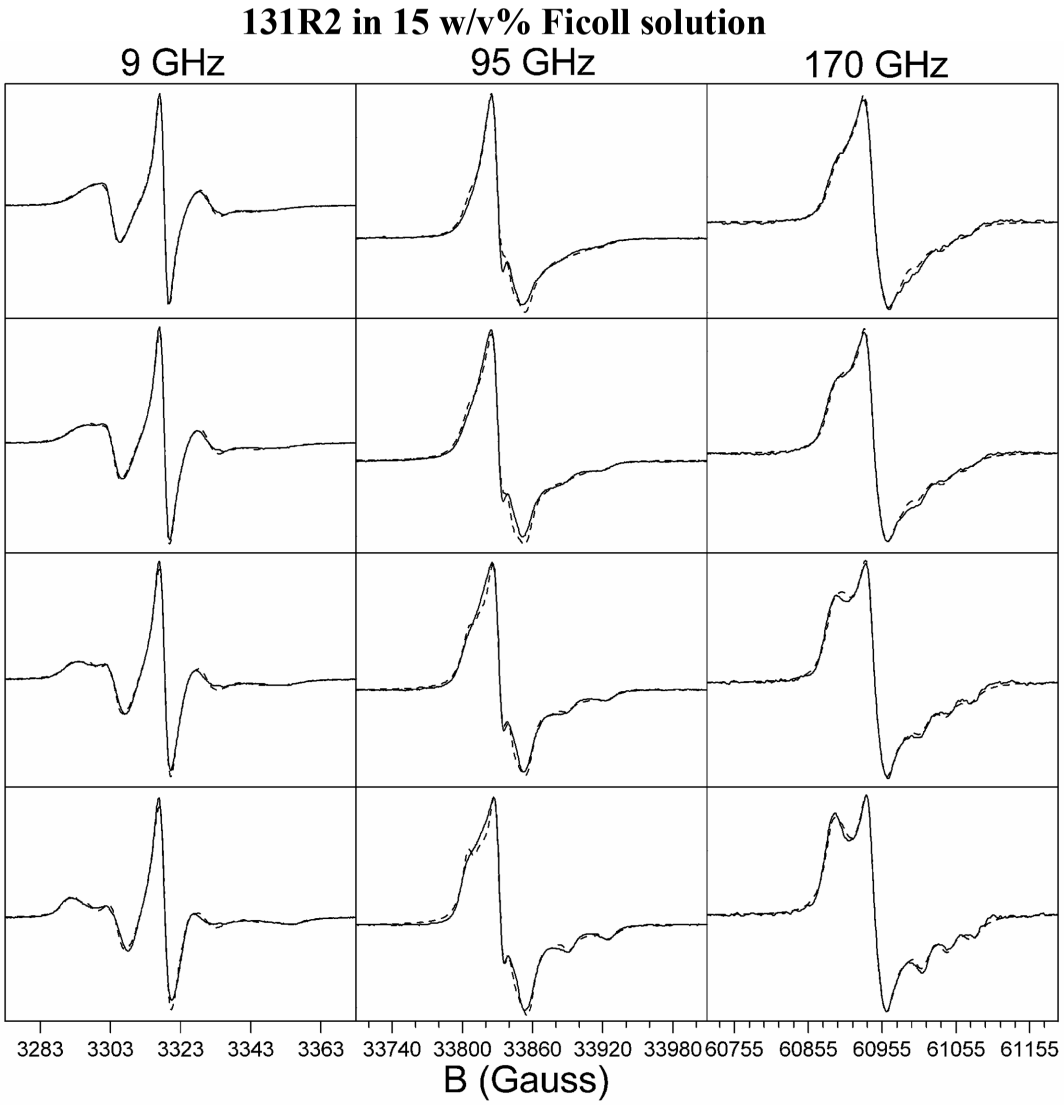

Figure 3-1 (Continued)

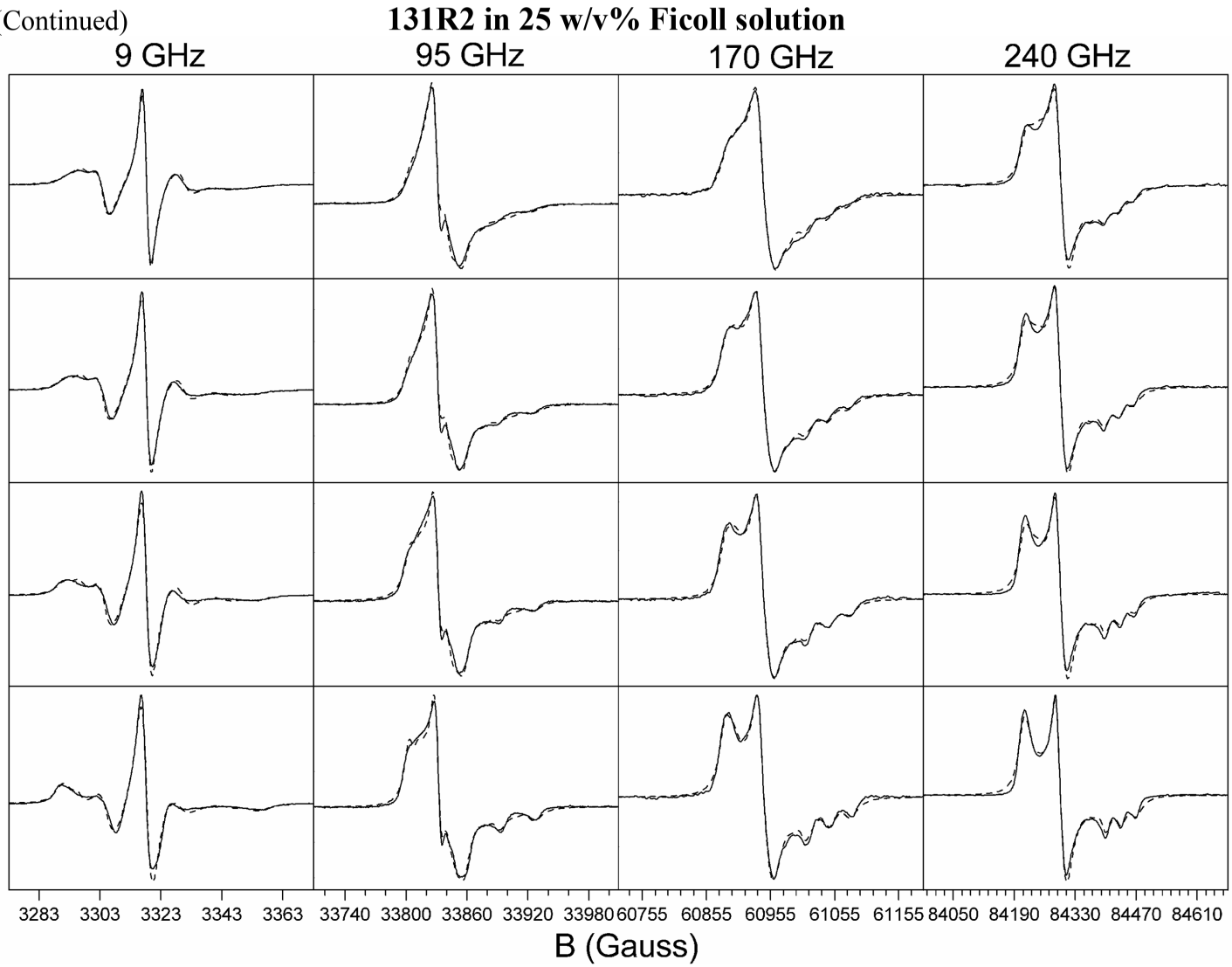

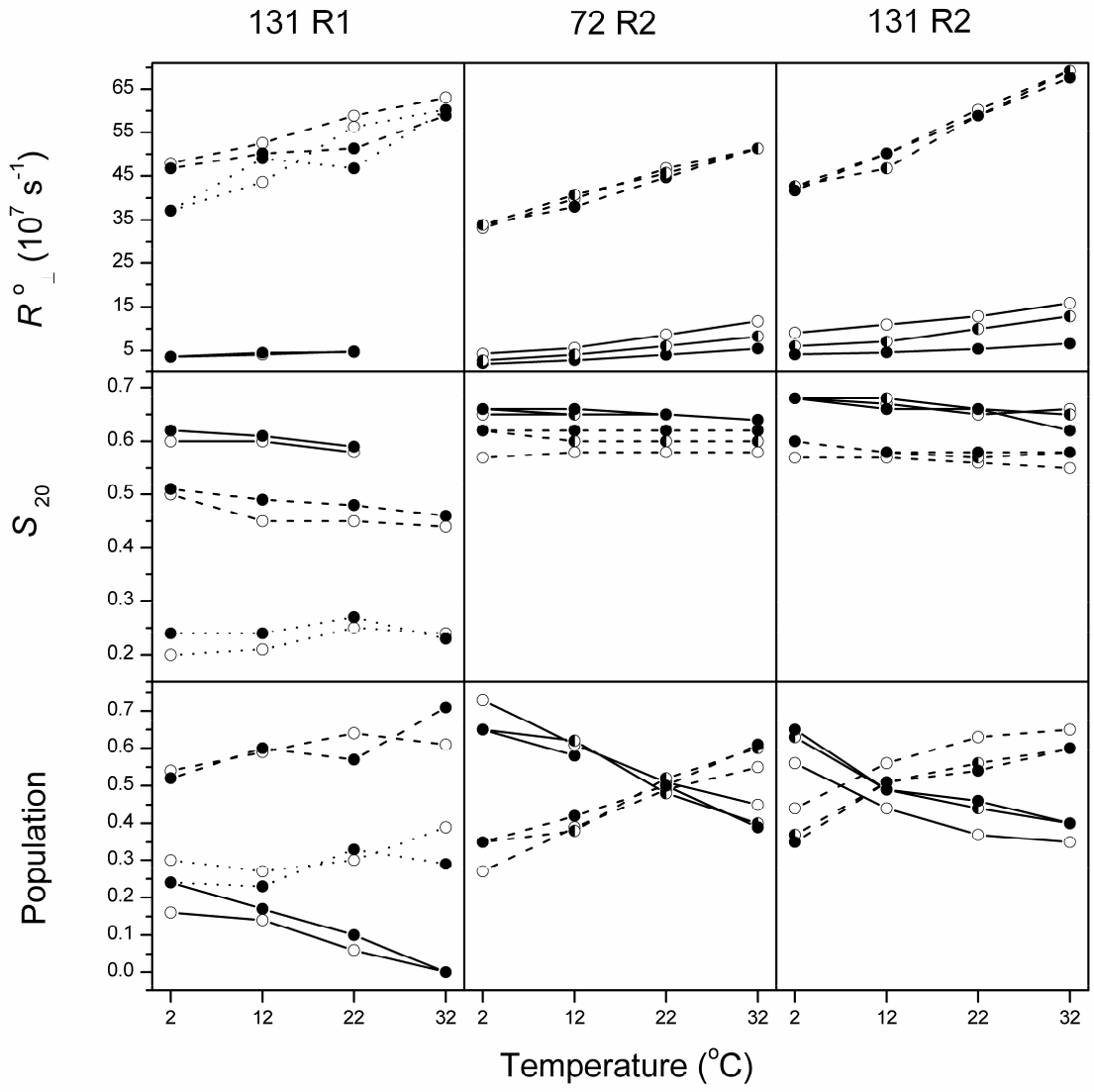

Figure 3-2. The best fit parameters of $R^o_\perp$, S_{20}, and the relative populations vs temperature from analysis of spectra recorded in water solution (○), in 15 w/v% Ficoll solution (◐), and in 25 w/v% Ficoll solution (●); the immobile component (solid line), the intermediate component (dashed line), the mobile component (dotted line).

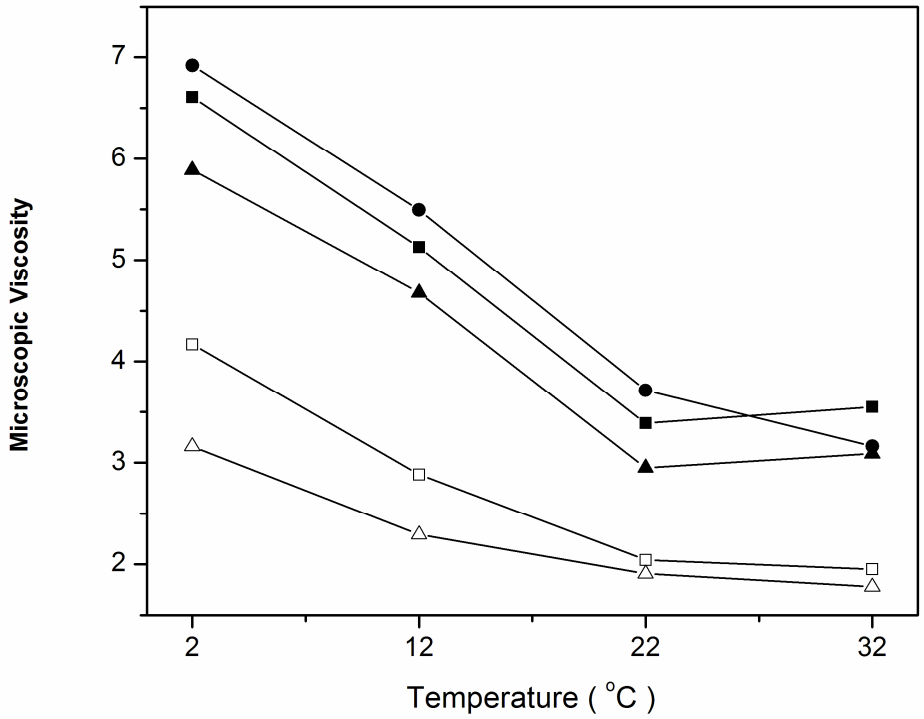

Figure 3-3. The microscopic viscosity with regard to the global tumbling of T4 lysozyme in 15 w/v% (empty symbol) and 25 w/v% (filled symbol) Ficoll solutions vs temperature; 131R1 (circle symbol), 72R2 (square symbol), 131R2 (triangle symbol).

Microscopic Viscosity ≡ R^c in water solution (see Table 2-2) / R^c in Ficoll solution (see Table 3-2)

immobile component and $R^{o}_{\perp}$ in the intermediate component) in Ficoll solution over those in water solution are displayed in Figure 3-4. We found in Figure 3-4 that R^{c} is the most affected in Ficoll solution, as can be expected from Ficoll's large size. Ficoll, as a macromolecule, is supposed to be a better viscogen than sucrose, since Ficoll produces a low osmotic pressure in solution and the protein should not be compressed (9). Therefore, the mobility of either the backbone or the spin labeled tether should not be suppressed by such pressure, as was demonstrated by Guo from a simple analysis of the 9 GHz data (9). However, in this multifrequency study, it is found that in Ficoll solution, $R^{o}_{\perp}$ of the immobile component does decrease when Ficoll is added into the solution. Even by allowing a larger fraction of the immobile component when simulating R2's spectra in Ficoll solution, the spectra cannot be fit without decreasing $R^{o}_{\perp}$ of the immobile component. On the other hand, for 131R1 at 32°C, with no immobile component in the simulation, the internal motion is still found to be slowed down by Ficoll in the solution, as is manifested by the increased S_{20} and decreased $R^{o}_{\perp}$ in the intermediate and the mobile components. Why the internal motion is slowed down in Ficoll solution will be discussed in Discussion.

3.3.2 The Global Tumbling in Ficoll Solution

3.3.2.1 Effect of R^{c} in Ficoll solution

30 w/w% sucrose solution, in which R^{c} of T4L is reduced by about a factor of 3 at room temperature, was used to increase the viscosity of the solution and minimize the contribution of R^{c} to the 9 GHz spectral lineshape (10, 76). This is a reason why the 9 GHz spectra of T4L recorded in 30% sucrose solution can be analyzed by using the MOMD model. In the present study, we used Ficoll 70 instead of sucrose as the viscogen to slow down the global tumbling of the protein. As shown in Figure 3-3, the

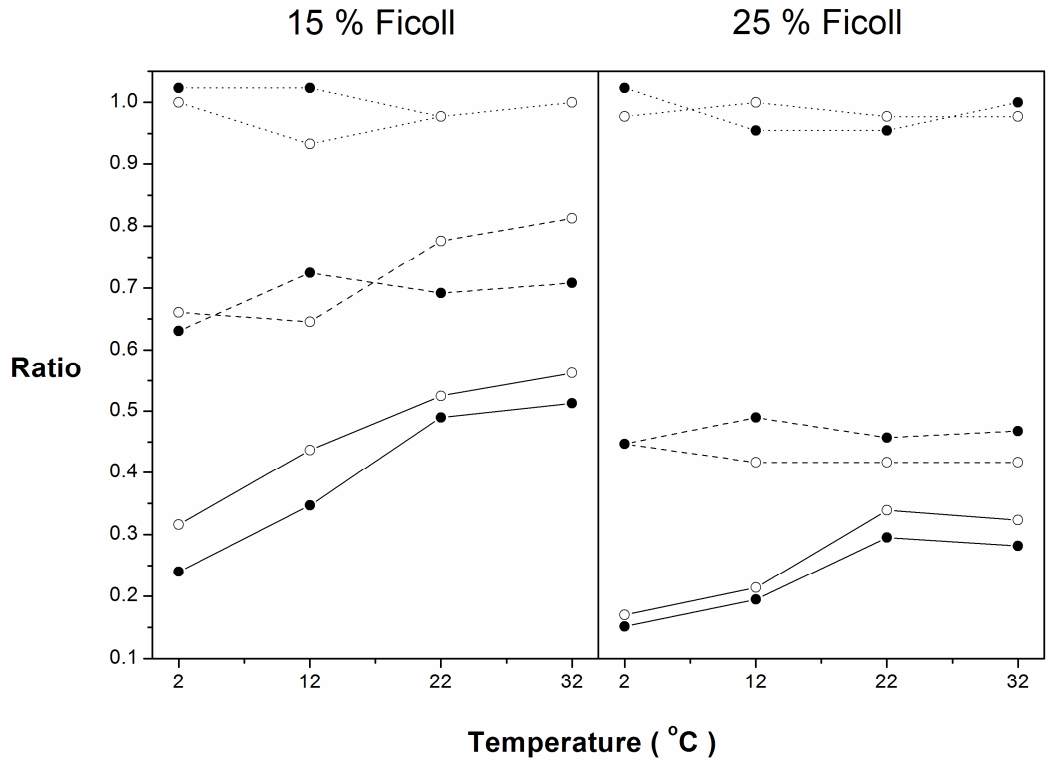

Figure 3-4. Decrease of R^c (solid line), $R^o{}_\perp$ in the immobile component (dashed line), and $R^o{}_\perp$ in the intermediate component (dotted line) of 72R2 (filled circle) and 131R2 (empty circle) in 15 and 25 w/v% Ficoll solutions.

Ratio ≡ Rotational diffusion rate in Ficoll solution (see Table 3-2) / Rotational diffusion rate in water solution (see Table 2-2)

microscopic viscosity of 25 w/v% Ficoll solution relative to that in an aqueous solution is 3.33 on average for the three samples at room temperature. This means that R^c is reduced in 25% Ficoll solution to about the same level as in 30% sucrose solution. We are now able to test whether the contribution of R^c in 25% Ficoll solution to the 9 GHz spectra of T4L is really negligible, given that the global tumbling and the internal motion are explicitly included in the simulations using the SRLS model. We chose 72R2 as the example. Two 9 GHz spectra were simulated with the best fit parameters from the fits to the multifrequency spectra of 72R2 in 25% Ficoll solution at 22^{o}C (see Table 3-2), except for the value of R^c. In Figure 3-5, R^c in the solid line spectrum was set to the best fit value of R^c in 25% Ficoll solution (see Table 3-2); R^c in the dashed line spectrum was set to $3.2*10^5$ s^{-1}, which we have found to be in the rigid limit at all frequencies, including 9 GHz. As seen in Figure 3-5, the subtle difference between these two simulated spectra indicates that whereas R^c in 25% Ficoll solution is not strictly in the rigid limit, it is slow enough that it hardly contributes to lineshape of the 9 GHz spectrum. [This observation is sensitive to the angle β_d used in the simulation for reasons noted in 2.4.5; thus, when a β_d=0° is used the best fit simulations show a greater deviation for the two cases of Figure 3-5.]

3.3.2.2 The reduced effect from R^c when β_d (diffusion tilt angle) > 0

It has been noted in 2.4.5 and 3.3.2.1 that, for $\beta_d > 0°$, the overall tumbling has a reduced effect on the spectrum. Below is the detailed proof and discussion.

Two 9 GHz spectra were simulated with same internal motion but different global tumbling rates (R^c) and compared in Figure 3-6A and 3-6B. When R^c is reduced from $1.58*10^6$ s^{-1} to $3.2*10^5$ s^{-1}, small change in lineshape can still be observed in Figure 3-6B. However, the simulated spectrum with $R^c = 3.2*10^5$ s^{-1} is shown to be almost identical to the simulated MOMD spectrum [There is no global tumbling in the

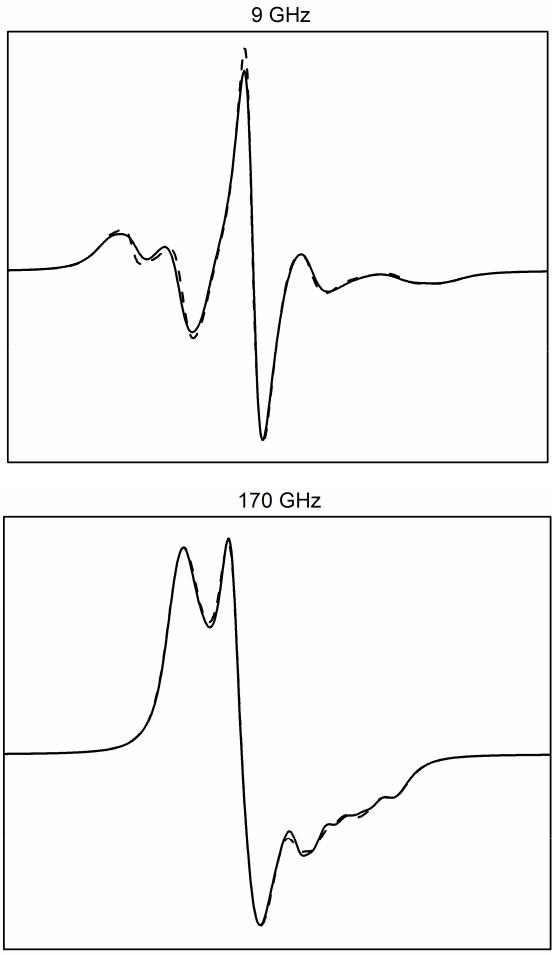

Figure 3-5. Comparison of the 9 and 170 GHz simulated spectra with the global tumbling rate (R^c) set to the value in 25 w/v% Ficoll solution (solid line) and to the rigid limit value (dashed line) respectively.

The solid line spectrum was simulated with the best fit parameters for 72R2 at 22^{o}C in 25 w/v% Ficoll solution (see Table 3-2).

The dashed line spectrum was simulated with the best fit parameters for 72R2 at 22^{o}C in 25 w/v% Ficoll solution (see Table 3-2), except that R^c was set to the rigid limit value (i.e. $3.2*10^5$ s^{-1}).

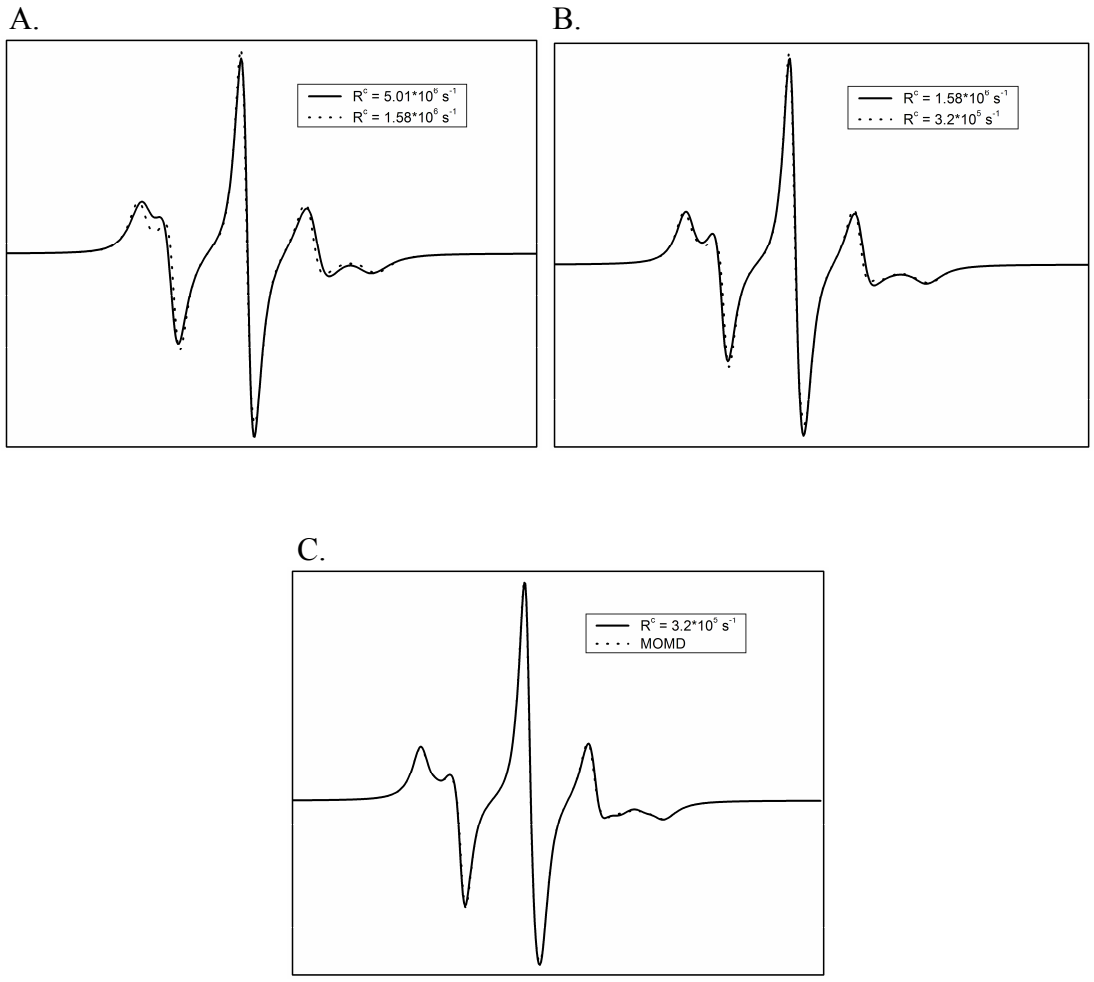

Figure 3-6.

A: Comparison of two SRLS spectra with $R^c = 5.01*10^6\ s^{-1}$ and $1.58*10^6\ s^{-1}$.

B: Comparison of two SRLS spectra with $R^c = 1.58*10^6\ s^{-1}$ and $0.32*10^6\ s^{-1}$.

C: Comparison of the SRLS spectrum with $R^c = 0.32*10^6\ s^{-1}$ and the MOMD spectrum.

Parameters used in simulations are $\beta_d = 0^o$, $R^o_\perp = 29.5*10^7\ s^{-1}$, $R^o_\parallel = 3.3*10^7\ s^{-1}$, $c_{20} = 1.5$, $c_{22} = 0.05$, $W = 0.99$ *G.*

MOMD model.] in Figure 3-6C. Thus when the global tumbling is as slow as $3.2*10^5$ s^{-1}, it can be regarded as completely frozen at the 9 GHz ESR time scale.

In the SRLS program, when the internal diffusion frame and the magnetic tensor frames are assumed to be coincident, the global tumbling and the internal spin label motion are coupled by the ordering potential (***S***). But when the three Euler angles (α_d, β_d and γ_d) between these two frames are considered and included in the simulation, the global tumbling and the internal motion are coupled by a term including not only the ordering potential but also three Euler angles. We here name this coupling term as the effective ordering ($\boldsymbol{S}_{effective}$). As noted in 2.3.1, only β_d is considered and the other two Euler angles are set to zero. When the symmetry of the ordering potential can be regarded as approximately uniaxial and the magnetic tensor is axial (e.g. ***A*** tensor but not ***g*** tensor), the effective ordering can be calculated by $S_{effective} = 0.5 * (3 \cos^2 \beta_d - 1) * S_{20}$. When β_d is set to 54.74^o, the effective ordering turns out to be zero and the global tumbling should have no effect on the lineshape even if R^c is very large. Such a hypothesis has been proved in Figure 3-7 by showing that the simulated SRLS spectrum with $R^c = 5.01*10^6$ s^{-1} and the simulated MOMD spectrum are identical with this special value for β_d.

The 9, 95, 170, and 240 GHz spectra of 131R1 recorded at 22 ^oC in water solution were simulated with a single component by using the SRLS model with axial $\boldsymbol{R}^{\mathbf{o}}$. β_d was respectively set to 0^o, 30^o, and 40^o in the simulation. R^c was set to $1.38*10^7$ s^{-1}, which is close to the average value for R^c at 22^oC in Table 2-2. Then the best fit parameters were used as initial parameters for fitting the 9 and 240 GHz spectra of 131R1 recorded at 22 ^oC in 25% Ficoll solution. R^c in Ficoll solution was set to $5.01*10^6$ s^{-1}, calculated by dividing R^c in water by 2.75. 2.75 is close to 3.33, which is the average microscopic viscosity of 25% Ficoll solution at 22 ^oC derived from this study (cf. 3.3.2.1). Best fit parameters, the effective ordering, and the reduced χ^2 are

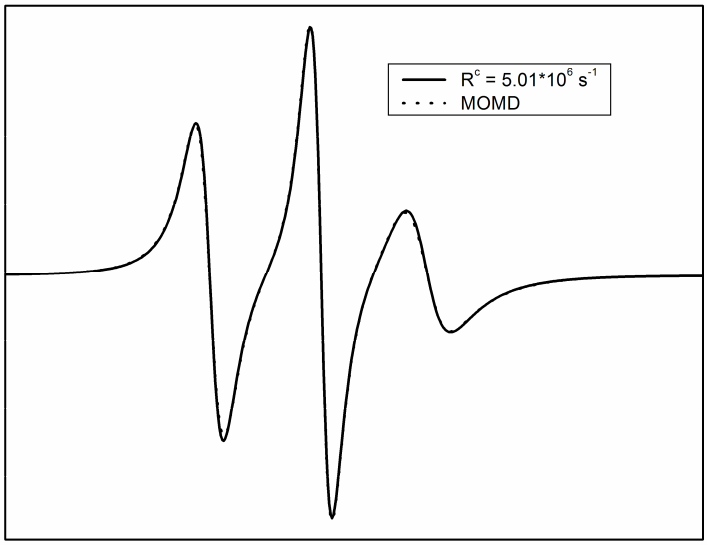

Figure 3-7. Comparison of the SRLS spectrum with R^c = 5.01*10^6 s^{-1} and the MOMD spectrum.

Parameters used in simulations are $\beta_d = 54.74^o$, $R^o_\perp = 29.5*10^7\ s^{-1}$, $R^o_\parallel = 3.3*10^7\ s^{-1}$, $c_{20} = 1.5$, $c_{22} = 0.05$, $W = 0.99$ G.

compared in Table 3-4 for these three tilt angles. The experimental data at 9 and 240 GHz and the best fits are displayed in Figure 3-8A and χ^2 at each frequency is labeled for each fit. Then, a 9 GHz MOMD spectrum was simulated for each tilt angle with the corresponding best fit parameters listed in Table 3-4. The MOMD spectrum is compared with the 9 GHz best fit SRLS spectrum in Figure 3-8B for each tilt angle. All spectra in Figure 3-8B were normalized to the same intensity. In Figure 3-8B, χ^2 (difference between the MOMD simulation and the SRLS fit) for each tilt angle is divided by χ^2 for $\beta_d = 0^o$ and labeled in each subplot. It is found that when β_d increases from 0^o to 30^o and finally to 40^o, the difference between spectrum with global tumbling in Ficoll solution and that with frozen global tumbling becomes smaller. This can be understood since the effective ordering (see Table 3-4) decreases with increased β_d from 0^o to 40^o.

3.3.3 Single- and Multi- Frequency Fit(s) to the Spectra of 131R1 in Ficoll Solution

The 9 and 240 GHz spectra of 131R1 in 25% Ficoll solution recorded at 32 ^{o}C were simulated individually as well as simultaneously. In each case, both single component and two component fits were performed. The same values for R^c and β_d were used in all the simulations. The best fit parameters from single- and multi- (i.e. two-) frequency simulations are compared in Table 3-5 for the two component fits and Table 3-6 for the single component fits. It is found that the best fit ordering parameters do not vary much with what frequency or how many frequencies are included in the fitting. But, the best fit values for $R^o_\perp$ from the 9 GHz fitting and that from the 240 GHz fitting are quite different. The best fit value for $R^o_\perp$ from simultaneous two-frequency fitting is closer to that from the 240 GHz fitting rather than that from the 9 GHz fitting. By further studying the single frequency simulation at 9 GHz, it is found

Table 3-4. Best fit parameters, the effective ordering, and the reduced χ^2 from simultaneously fitting the 9 and 240 GHz spectra of 131R1 at 22 ^{o}C in 25% Ficoll solution by using the SRLS model with axial $\boldsymbol{R}^{\mathbf{o}}$

β_d (^{o})	$R^{o}_{\perp}$ (10^7 s^{-1})	$R^{o}_{\parallel}$ (10^7 s^{-1})	c_{20}	c_{22}	S_{20}	S_{22}	$S_{effective}$	W_9 (G)	W_{240} (G)	Reduced χ^2
0	29.5	3.3	1.50	0.05	0.33	0.01	0.33	0.99	4.28	152
30	37.2	0.004	1.98	-0.51	0.42	-0.09	0.26	0.60	5.29	175
40	39.8	0.016	2.31	-0.83	0.47	-0.12	0.18	0.20	5.30	366

Table 3-5. Best two component fit results from (1) the 9 GHz fitting, (2) the 240 GHz fitting, and (3) the simultaneous two-frequency fitting.

Frequency to Fit (GHz)	9		240		9 + 240	
R^c / β_d	$0.6*10^7$ s^{-1} / 20^o					
Component	Intermediate	Mobile	Intermediate	Mobile	Intermediate	Mobile
$R^o_\perp$ (10^7 s^{-1})	34.7	20.4	63.1	63.1	58.9	58.9
$R^o_\parallel$ (10^7 s^{-1})	0.001	4.5	2.1	6.0	2.5	1.0
c_{20}	2.56	1.17	2.56	1.18	2.55	1.21
c_{22}	-1.59	1.12	-1.72	1.70	-1.53	0.86
S_{20}	0.45	0.19	0.43	0.11	0.45	0.23
S_{22}	-0.22	0.29	-0.24	0.43	-0.21	0.22
$W_{9\ GHz}$ (G)	0.42		---		0.86	
$W_{240\ GHz}$ (G)	---		4.71		4.64	
Population (%)	57	43	75	25	71	29
χ^2	22		28		42 *	

* χ^2 = (χ^2 at 9 GHz + χ^2 at 240 GHz) / 2

Table 3-6. Best single component fit results from (1) the 9 GHz fitting, (2) the 240 GHz fitting, and (3) the simultaneous two-frequency fitting.

Frequency to Fit (GHz)	9	240	9 + 240
R^c / β_d	$0.6*10^7$ s^{-1} / 20^o		
$R^o_\perp$ (10^7 s^{-1})	16.2	45.7	43.7
$R^o_\parallel$ (10^7 s^{-1})	1.2	0.3	0.6
c_{20}	1.33	1.70	1.66
c_{22}	0.05	-0.46	-0.30
S_{20}	0.30	0.37	0.36
S_{22}	0.01	-0.09	-0.06
$W_{9\ GHz}$ (G)	0.19	---	0.78
$W_{240\ GHz}$ (G)	---	2.47	3.97
χ^2	27	54	64 *

* χ^2 = (χ^2 at 9 GHz + χ^2 at 240 GHz) / 2

A.

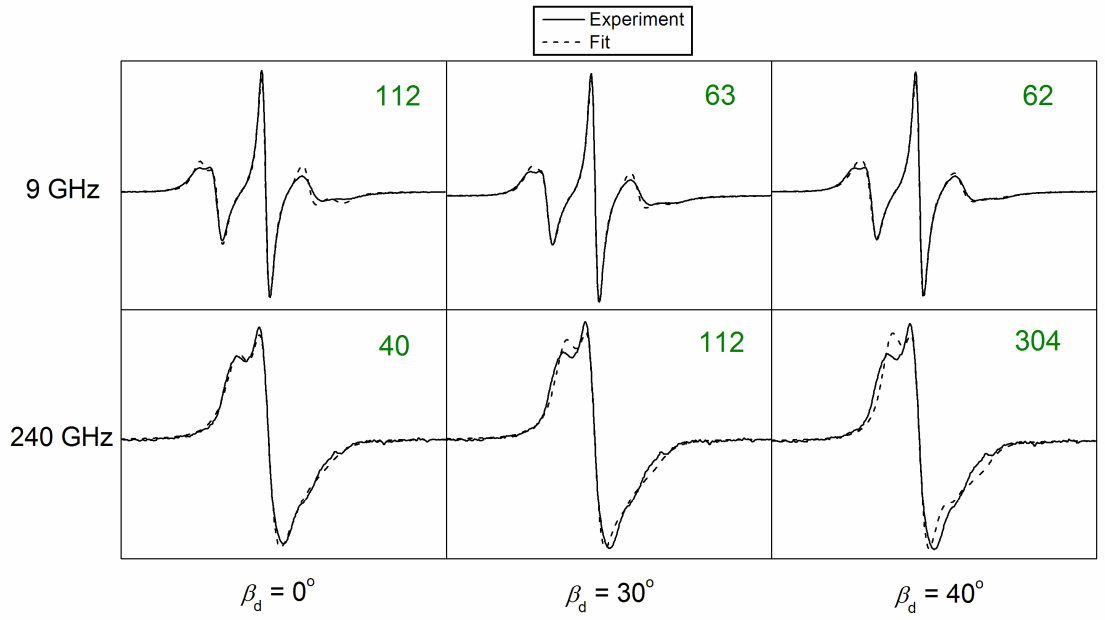

B.

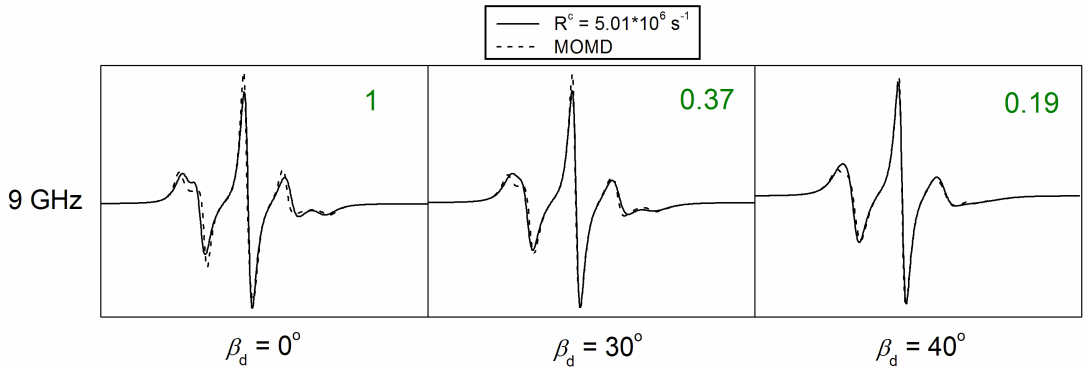

Figure 3-8.

A: The experiment data and the best fits to the 9 and 240 GHz spectra of 131R1 at 22°C in 25% Ficoll solution using the SRLS model with axial $\boldsymbol{R^0}$. χ^2 at each frequency is labeled in each subplot.

B: The solid line spectra are 9 GHz SRLS simulations with best fit parameters in Table 3-4. The dashed line spectra are 9 GHz MOMD simulations with best fit parameters in Table 3-4 (R^c not included). [χ^2 for each β_d / χ^2 for $\beta_d = 0^o$] is labeled in each subplot.

that there is a correlation between $R^{o}_{\perp}$ and the inhomogeneous Lorenzian broadening (i.e. $W_{9\,GHz}$ in Table 3-5 and 3-6). When $W_{9\,GHz}$ increases, the best fit value for $R^{o}_{\perp}$ increases correspondingly. To further prove such correlation, 2 two-component fits were performed for the 9 GHz experimental spectrum: (1) In the first fitting, all parameters including $W_{9\,GHz}$ were varied until the best fit was obtained; (2) In the second fitting, $W_{9\,GHz}$ was set to 0.85 G, which is much larger than the best fit $W_{9\,GHz}$ from the first fitting (0.42 G), and the other parameters were varied until the best fit was obtained. The fit results are listed in Table 3-7. Although $R^{o}_{\perp}$ and $W_{9\,GHz}$ are quite different in these two simulations, similar simulated spectra can be obtained (see Figure 3-9). In contrast, in the 240 GHz simulation, the fitting of $R^{o}_{\perp}$ is independent of that of $W_{240\,GHz}$. Thus, the best fit value for $R^{o}_{\perp}$ from the 240 GHz fitting is more reliable and closer to the value from the multifrequency fitting.

Moreover, based on some previous work and experience, the 9 GHz fitting is also very sensitive to R^{c}, whereas the 240 GHz fitting is not.

3.4 DISCUSSION

We noted in 3.3.1 that Ficoll has some effect on the internal motion. We further demonstrate this in Figure 3-10. The solid line spectrum was simulated with the best fit parameters from the fits to the multifrequency spectra in water solution at 22^{o}C (see Table 2-2), except that R^{c} was set to the best fit value in 25% Ficoll solution (see Table 3-2). The dashed line spectrum was simulated with the best fit parameters from the fits to the multifrequency spectra in 25% Ficoll solution at 22^{o}C (see Table 3-2). The difference between the two simulated spectra in Figure 3-10A, 3-10B, and 3-10C respectively show Ficoll's effect on the internal motion of 72R2, 131R2, and 131R1.

Table 3-7. Best fit results from 2 two-component fits to the 9 GHz spectrum:

(1) In 1st fitting, all parameters including $W_{9\,GHz}$ were varied;

(2) In 2nd fitting, $W_{9\,GHz}$ was fixed to 0.85 G, and the other parameters were varied.

Fitting #	1st Fitting		2nd Fitting	
Frequency to Fit (GHz)	9		9	
R^c / β_d	$0.6*10^7$ s^{-1} / 20^o			
Component	Intermediate	Mobile	Intermediate	Mobile
$R^o_\perp$ (10^7 s^{-1})	34.7	20.4	79.4	41.7
$R^o_\parallel$ (10^7 s^{-1})	0.0006	4.5	2.1	0.8
c_{20}	2.56	1.17	2.58	1.18
c_{22}	-1.59	1.12	-1.24	0.95
S_{20}	0.45	0.19	0.49	0.21
S_{22}	-0.22	0.29	-0.16	0.24
$W_{9\,GHz}$ (G)	0.42		0.85 (fixed)	
Population (%)	57	43	63	37
χ^2	22		31	

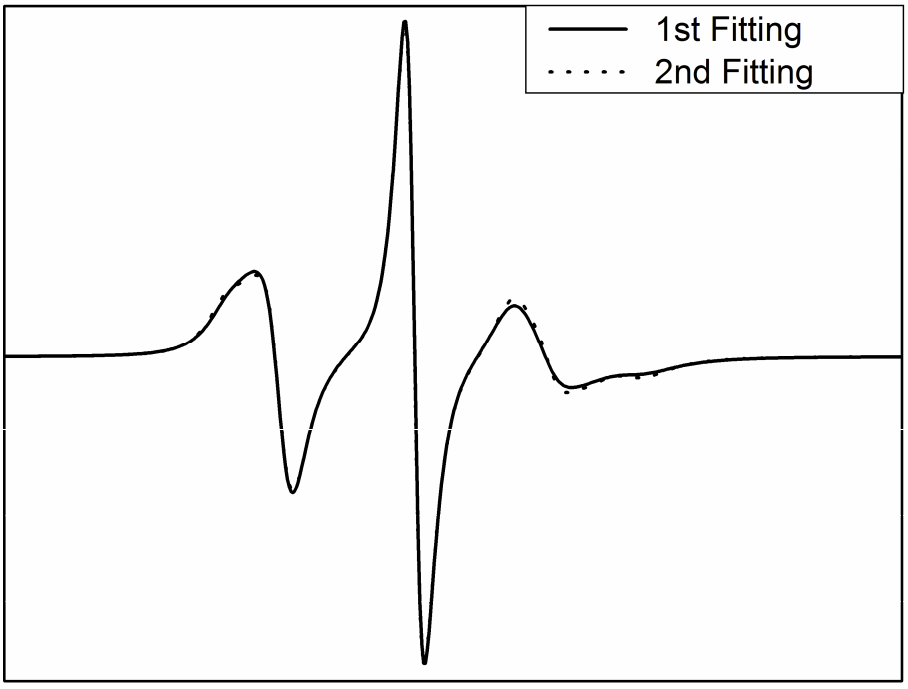

Figure 3-9. The simulated spectra from 1st fitting and 2nd fitting with parameters listed in Table 3-7.

Figure 3-10. Comparison of two 9 (170 or 240) GHz simulated spectra with the dynamic and ordering parameters of the internal motion set to values in water solution (solid lines) and in 25 w/v% Ficoll solution (dashed lines) respectively.

The solid line spectrum was simulated with the best fit parameters at 22 ^{o}C in water solution (see Table 2-2), except that R^{c} was set to the value in 25 w/v% Ficoll solution: (A) 72R2; (B) 131R2; and (C) 131R1.

The dashed line spectrum was simulated with the best fit parameters at 22 ^{o}C in 25 w/v% Ficoll solution (see Table 3-2).

A.

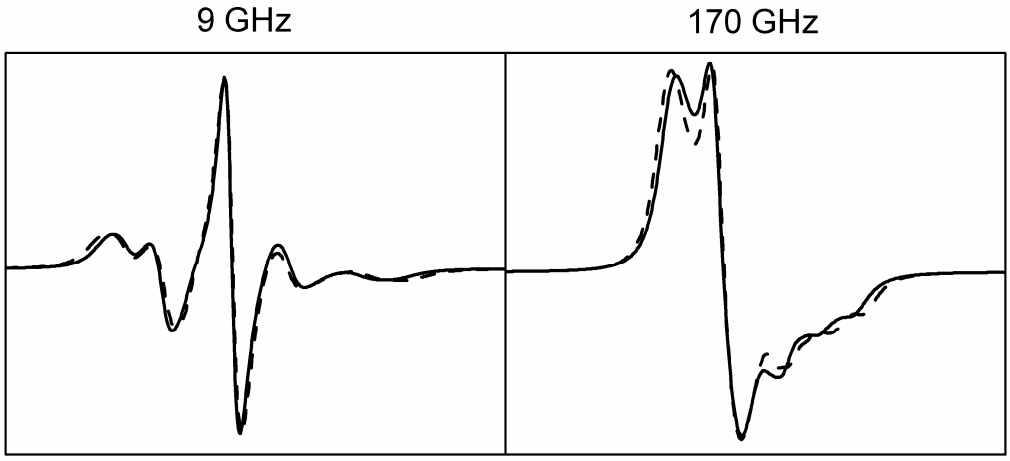

B.

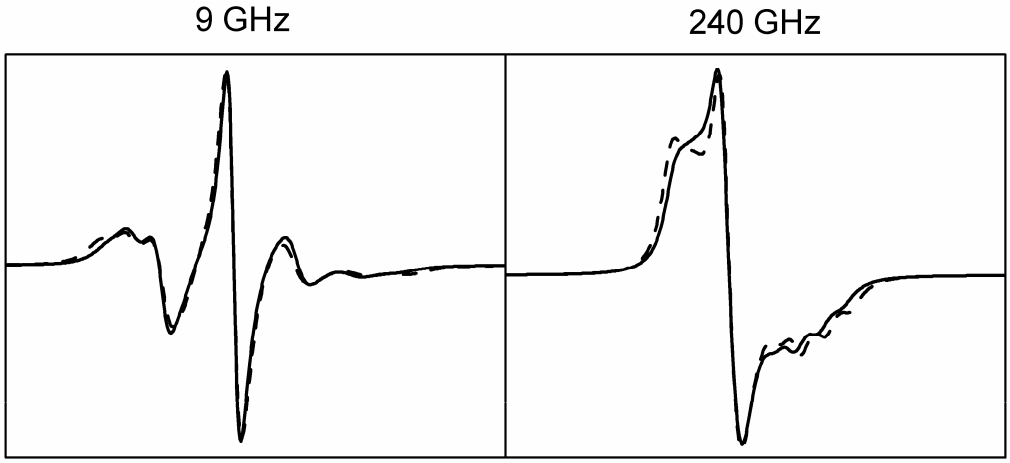

C.

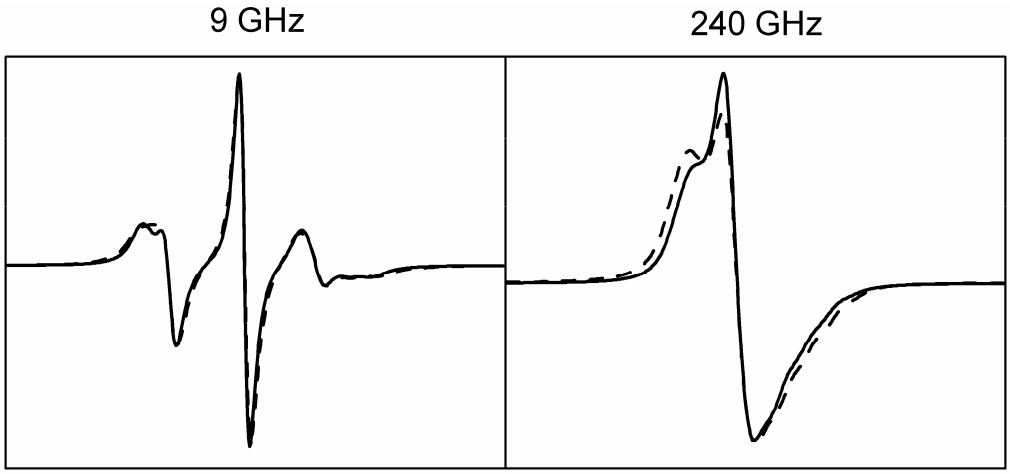

For 72R2 and 131R2 (see Figure 3-10A and 3-10B), the difference at 9 GHz is small but the difference at high frequency is prominent. A reduction in $R^{o}_{\perp}$ of the immobile component contributes most to the prominent lineshape change at high frequency caused by adding Ficoll. The three peaks in the g_{zz} region of the 170 GHz spectrum of 72R2 or the 240 GHz spectrum of 131R2 are from the immobile component and shift dramatically to the high field direction with Ficoll in the solution, confirming that the high field ESR is more sensitive in observing any change in the immobile component. The fact that the 9 GHz spectra are much less sensitive to the immobile component, and it is this component rather than the intermediate one, that is affected by the Ficoll (cf. Figure 3-4) may explain why the addition of sucrose up to 40 w/w% appears to have no effect on the internal motion, as concluded from the simple analysis of the 9 GHz spectra (61, 83). If the focus is on just the intermediate component then it follows from Figure 3-4, that the addition of Ficoll hardly affects its motion. However, adding Ficoll increases the ordering of the intermediate component by 0.01-0.05.

For 131R1 (see Figure 3-10C), the difference at 9 GHz is even smaller compared to the two cases for R2. The very little change in the 9 GHz spectrum is consistent with what Lopez et al. concluded from their extensive 9 GHz study on R1 that Ficoll has little effect on the internal motion of the spin label (61). However, although the difference at 9 GHz is almost negligible, we still observe some difference at 240 GHz caused by the changes in $R^{o}_{\perp}$ and the ordering of the mobile and intermediate components.

What then is the mechanism by which Ficoll slows down the internal motion? There are two relevant ones that one may consider, both based on the well-known molecular crowding (84, 85, 86, 87, 88, 89, 90), i.e. the molecular crowding properties of Ficoll 70 (91). First, for proteins that occupy a manifold of conformational states,

each with a different volume, crowders will drive the equilibrium toward the state of minimum volume. T4L is a two-domain protein with interdomain hinges that allow opening and closing of the active site cleft (92). The open state is the dominant population in solution (16, 93), and has a larger excluded volume than the closed state. As anticipated, Ficoll 70 (25% w/w) drives the equilibrium toward the closed state (94). On the other hand, the melting point of T4L is insensitive to Ficoll 70 (61), and the C terminal domain, in which 72 and 131 reside, is very stable (95), characterized by low Debye Waller factors in the crystal structures (15), and shows no detectable conformational exchange in NMR relaxation experiments (9). Thus, there is no evidence for substantial conformational heterogeneity in the C terminal domain that would be modulated by a crowder. Moreover, the 9 GHz spectrum of 72R1 is apparently insensitive to the hinge motion (16); as is 131R1 (96). Collectively, these data make it unlikely that Ficoll 70 produces stabilization and increased packing of the T4L C terminal domain, in agreement with the lack of effect of Ficoll 70 on the internal motion of 72R1 and 131R1 observed here and in the earlier study of Lopez et al (61). Thus, one would also expect Ficoll 70 not to influence the motion of R2 at either site, contrary to the experimental data.

A second characteristic of crowders is the ability to drive intermolecular associations that would not normally be observed, i.e., the formation of oligomers. T4L is clearly monomeric in solution at low concentrations, but at the high concentrations needed in these experiments (1 – 2 mM) in the presence of 25% w/w Ficoll 70 with a fractional volume occupation of ca. 60% (91) it is entirely possible that weak and non-specific surface associations occur between T4L molecules, or between T4L and Ficoll 70. If this is the case, our results could be explained by assuming that the more hydrophobic R2 is instrumental in driving the association, and hence the crowder only influences T4L molecules bearing R2 and not R1.

It has been shown by Stagg et al. that in the presence of 25% Ficoll, a globular protein with comparable molecular weight to T4L appeared more compact than in its native structure (97).

Finally we would like to address a specific issue that arises in using multi-frequency data to fit to the dynamical model utilized. One can, in general, fit an individual single frequency spectrum with somewhat higher quality of fit and perhaps fewer parameters than emerges in the fitting of as many as four different spectra all at different frequencies. However, given what we have just noted, the spectra at the different frequencies provide different perspectives on the molecular motions, and therefore taken together provide a fuller picture of the dynamics, so they should all be given significant weight. It may be easy to obscure certain details of the dynamics from a single "snapshot" with a single "view-point" which may be observable from another. However, given that the model (e.g. the SRLS model that we have used) is an approximate one, then it will necessarily not include all the motional details that could affect the various ESR spectra (as we have argued above). It can therefore be expected that the snapshots taken at different speeds and view-points will uncover some details not well represented in the approximate model. This is a likely reason why we can generally fit individual spectra (each with their more limited information content) better than we do with the multifrequency approach. However, we do wish to emphasize that despite this fact, a major achievement in the present study is that we consistently do achieve good fits at all frequencies with the same set of fitting parameters. Further progress in assessing the relative importance of the features in the spectra at each frequency would benefit from careful sensitivity analysis, as is currently being conducted by Earle et al. (98).

3.5 CONCLUSIONS

The main findings are the following:

(1) We found in Ficoll solution, not only the global tumbling is reduced as expected, but the internal motion is slowed down somewhat.

(2) The addition of Ficoll reduces R^c according to a microscopic viscosity that is proportional to the macroscopic viscosity taken to the 0.39 power.

(3) The addition of Ficoll reduces substantially the motional rate of the "immobile" component in R2, but has no significant effect on the "intermediate" component for 72R2 and 131R2 except for an increase in its ordering. For 131R1 the effect on the "immobile" component is much reduced, with no significant effects on the "mobile" and "intermediate" components.

(4) The effect of Ficoll on the internal motion could possibly be explained by molecular crowding.

CHAPTER 4

STUDY OF T4 LYSOZYME 'S DYNAMICS IN HIGH CONCENTRATION SUCROSE SOLUTION AND AT LOW TEMPERATURE

4.1 INTRODUCTION

The experimental data and corresponding simulations for the four spin labeled T4 lysozyme samples, 72R1, 131R1, 72R2, and 131R2, in both water and Ficoll solutions collected around room temperature have been discussed in Chapter 2 and 3. In this chapter, first, it is discussed what are the 'good' magnetic tensors, i.e. $\boldsymbol{g}$ tensor and $\boldsymbol{A}$ tensor, to be used when simulating data recorded around room temperature. To obtain values for the magnetic tensor components, experiments for the four samples in very high viscous sucrose solution at low temperatures were performed, and the results were analyzed. In addition, the dynamic models for the residual motion of the spin labeled tether in such condition were constructed to supply a basis for the dynamics of the spin label around room temperature.

4.2 EXPERIMENTAL

Experiments were performed at low temperatures and with high viscosities mainly to obtain accurate rigid limit magnetic tensors, but also to study residual protein motions at the low temperatures.

The 9 and 170 GHz spectra of the 4 mutants listed in Table 4-1 were recorded at -50, -35, -20, -5, and +10 ^{o}C in 65 w/w% sucrose solution. The experimental spectra are displayed in Figure 4-1. Samples were prepared by mixing 79 w/w%

Table 4-1. The nitroxide labeled T4 lysozyme samples for multifrequency (9 and 170 GHz) ESR study in 65 w/w% sucrose solution

Sample No.	Mutant Site	Spin Label	Sucrose Concentration (w/w %)
1	72	R1	65
2	131	R1	65
3	72	R2	65
4	131	R2	65

Figure 4-1.

The experimental spectra of 72R1 (A and E), 131R1 (B and F), 72R2 (C and G), and 131R2 (D and H) in 65 w/w% sucrose solution taken at 9 GHz (A to D) and at 170 GHz (E to H). In each figure, the five spectra, from top to bottom, are recorded at -50, -35, -20, -5, and +10^{o}C respectively.

A.

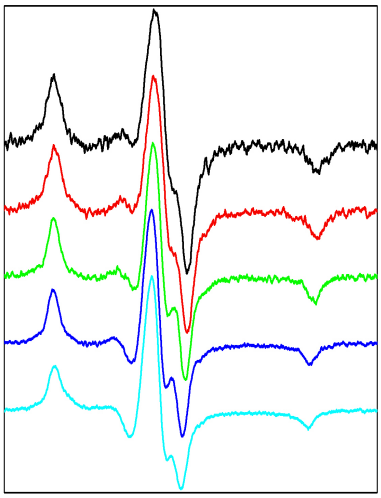

B.

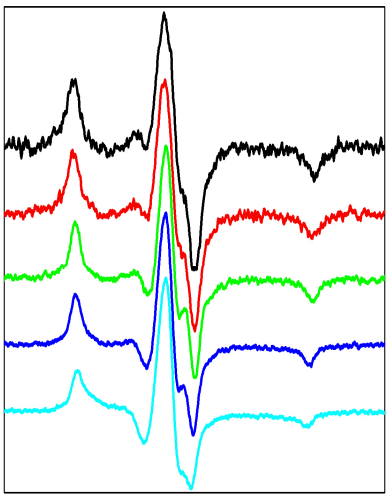

C.

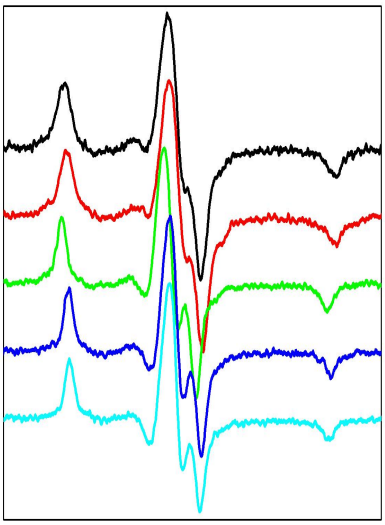

D.

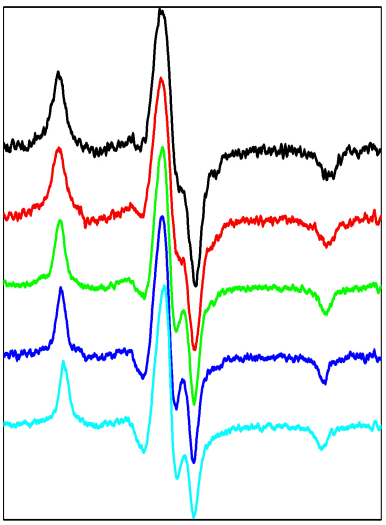

Figure 4-1 (Continued)

E.

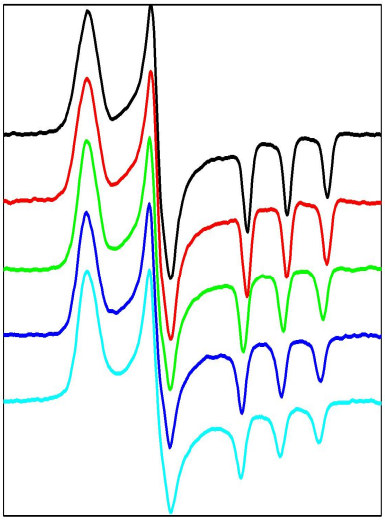

F.

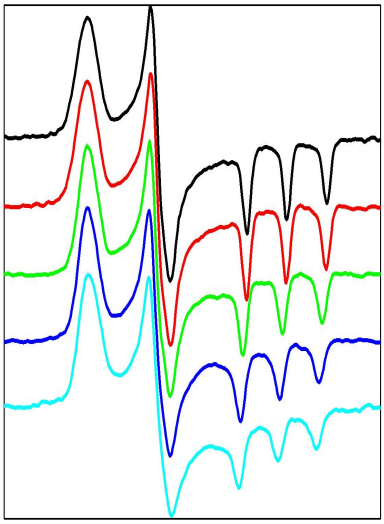

G.

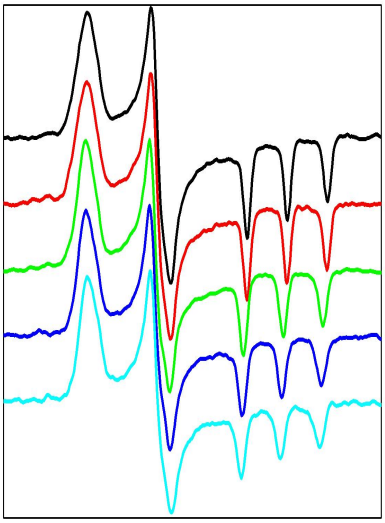

H.

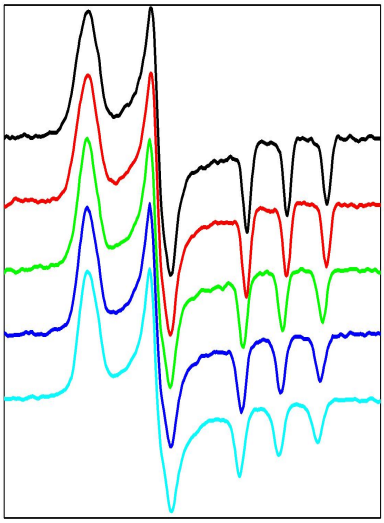

sucrose and protein solution. In order to achieve the same final concentration of sucrose in all samples, a same stock solution of 79 w/w% sucrose was used. As described in 2.2, for 9 GHz experiments, glass capillary was used as sample holder, whereas for 170 GHz experiments, quartz plates were used as sample holder. For experiments at temperature below the freezing point of 65 w/w% sucrose solution (-17 ^{o}C) (99), the sample was initially cooled to -70 ^{o}C, and then the temperature was increased to the destination temperature (100). Such an annealing process was applied to produce maximally freeze-concentrated samples at each temperature set point, so that, at equilibrium, the concentration of sucrose was the same in all samples. However, it was found that, either with or without annealing, spectra at a certain temperature were reproducible as long as the same cooling process was carried out. In 9 GHz experiments where glass capillaries were used as sample holders, there was a slight change in lineshape if samples were directly cooled to the destination temperature without annealing; whereas in 170 GHz experiments where quartz plates were used as sample holders, identical spectra were obtained no matter whether the annealing process was applied or not.

The phase of the experimental spectra recorded at 170 GHz was adjusted to correct for a small admixture of dispersional signal, according to the procedure described previously (70).

4.3 METHODS

4.3.1 Magnetic Tensor Components

The 9 and 170 GHz spectra of the four mutants in 65 w/w% sucrose solution at -50^{o}C were simulated to obtain the hyperfine ($\boldsymbol{A}$) tensor and $\boldsymbol{g}$ tensor components. Experiments at temperatures lower than -50^{o}C were also collected at both frequencies

(-90°C at 9 GHz and -155°C at 170 GHz), but they showed no further change in lineshape from those taken at -50°C. Thus, at -50°C and in 65 w/w% sucrose solution, the spin label can be regarded as completely immobilized on the time scales of ESR at both frequencies. The 9 and 170 GHz spectra recorded at -50°C in 65 w/w% sucrose solution displayed identical spectra to those in 30 w/w% Ficoll solution at the corresponding temperature, indicating that the addition of sucrose to 65 w/w% does not affect the magnetic tensor components, considering the different concentrations of sucrose and Ficoll as well as the large difference in their molecular sizes. Timofeev et al. (83) previously found that the isotropic hyperfine constant remains unchanged with the addition of sucrose up to 65 w/w%. These spectra were simulated as rigid limit spectra by performing nonlinear least squares (NLLS) fits using the microscopic ordering with macroscopic disordering (MOMD) model with an extremely slow motional rate of 10^5 s^{-1}, i.e. the rigid limit on the ESR time scale (73).

The 9 GHz spectra are more sensitive to the ***A*** tensor components, whereas the ***g*** tensor components can be accurately determined from the 170 GHz fits. An exception is A_{zz} which can be well estimated from spectral fits at both frequencies. The fitting process applied to the spectra of all four mutants is described as follows. First, the magnetic field (B_o^{zz}), corresponding to central g_{zz} component in the spectrum, was measured directly at 170 GHz. Then g_{zz} was calculated from

$$g_{zz} = \frac{h\nu}{\beta_e B_o^{zz}}$$

with ν = 171.100 GHz. The measured value of g_{zz} was used in the following procedures. Then, the experimental 170 GHz spectra were fit by varying g_{xx}, g_{yy}, the ***A*** tensor, and the Lorentzian inhomogeneous broadening (***W***) tensor. (Gaussian

broadening was set to zero to simplify the fitting process.) The corresponding experimental 9 GHz spectrum was fit with g_{xx} and g_{yy} fixed at the values found from the 170 GHz fit, by varying the $\boldsymbol{A}$ tensor and the $\boldsymbol{W}$ tensor. Small uncertainties in $\boldsymbol{g}$ tensor parameters from the fits at 170 GHz have insignificant effect on the analysis of spectra at 9 GHz. Finally, the experimental 170 GHz spectrum was fit again by varying g_{xx}, g_{yy} and the $\boldsymbol{W}$ tensor with the $\boldsymbol{A}$ tensor components fixed at the values found from the 9 GHz fit. Magnetic tensor parameters including $\boldsymbol{A}$ tensor components from the 9 GHz fits and $\boldsymbol{g}$ tensor components from the 170 GHz fits are given in Table 4-2 (101). Values of A_{zz} found from the 170 GHz fits were identical to the ones listed in Table 4-2. Magnetic tensor components for the four mutants are the same within the uncertainty of the experiments and fits. The values of magnetic tensor components, especially of A_{zz} and g_{xx}, are related to the structure of the spin label and the polarity of the local environment to which the spin label is exposed (71, 102). Thus, we find that sites 72 and 131 are exposed to local environment of the same polarity.

Once determined, the $\boldsymbol{A}$ and $\boldsymbol{g}$ tensor components were fixed and used as input parameters in the other simulations to extract information regarding motions.

4.4 RESULTS

4.4.1 72R1 vs 131R1 and 72R2 vs 131R2

The 9 and 170 GHz spectra of the four mutants in 65 w/w% sucrose solution were recorded over a temperature range of -50 to +10^{o}C. The spectra of 72R2 and 131R2 are identical over the whole temperature range (see Figure 4-2), whereas the spectra of 72R1 and 131R1 have identical lineshapes only at very low temperatures,

e.g. -50 and -35°C (see Figure 4-3). At higher temperatures, e.g. -5 and +10°C, the motion of 131R1 is faster than that of 72R1, as seen in Figure 4-3.

In the previous study on 72R1 and 131R1, it was assumed that 65 w/w% sucrose solutions provided virtually rigid limit spectra (28). Our study encompassing the range of -50°C to +10°C clearly demonstrates that at +10°C the spectra are significantly affected by motion. Thus the true rigid limit $\boldsymbol{g}$ and $\boldsymbol{A}$ tensors given in Table 4-2 show some differences with those reported in the previous study. But a comparison of the estimates of these tensors from our current +10°C spectra, when incorrectly interpreted as rigid limit spectra, yields relative results in rather good agreement with those reported previously. The most prominent effects of the increase in temperature are an apparent substantial increase in g_{zz}, a decrease in g_{xx}, and a very small decrease in g_{yy}. [Also, A_{zz} appears to decrease, while A_{yy} increases, but A_{xx} hardly changes.] The differences previously noted in the magnetic tensors for 72R1 and 131R1 at +10°C were tentatively ascribed to local polarity differences (28). Our present study makes clear that the true rigid limit magnetic tensors in 65% sucrose are identical, and the differences at +10°C result from differences in their mobilities.

At 10°C, the identical spectra observed for 72R2 and 131R2 can be fit as rigid limit spectra by varying magnetic and linewidth tensors, although their broader lines than for -50°C spectra indicate incipient slow motion. They can be fit with a single component, i.e. the immobile component. The absence of the intermediate component could suggest that the equilibrium has substantially shifted to the immobile component in 65% sucrose solution vs aqueous solution or else the near rigid spectra provide much too limited features to discriminate two components.

The spectra of 72R1 and 131R1 are clearly slow motional, nor can these spectra be well fit with a single component. This further supports that, at +10°C, there should be at least a second component for R1. One component is an immobile one,

Table 4-2. Magnetic tensor components [a, b]

Mutant Site	Spin Label	g_{xx}	g_{yy}	g_{zz}	A_{xx}	A_{yy}	A_{zz}
72	R1	2.00839	2.00615	2.00232	6.2	4.3	36.9
131	R1	2.00841	2.00616	2.00232	6.0	4.1	37.0
72	R2	2.00841	2.00616	2.00231	6.3	4.6	37.2
131	R2	2.00840	2.00615	2.00231	6.3	4.6	37.1

[a] The estimated absolute error in the $\boldsymbol{g}$ tensor components is $\pm 7*10^{-5}$, but the estimated error in their relative values is $\pm 1*10^{-5}$.

[b] The estimated error in $\boldsymbol{A}$ tensor components is ±0.2 G.

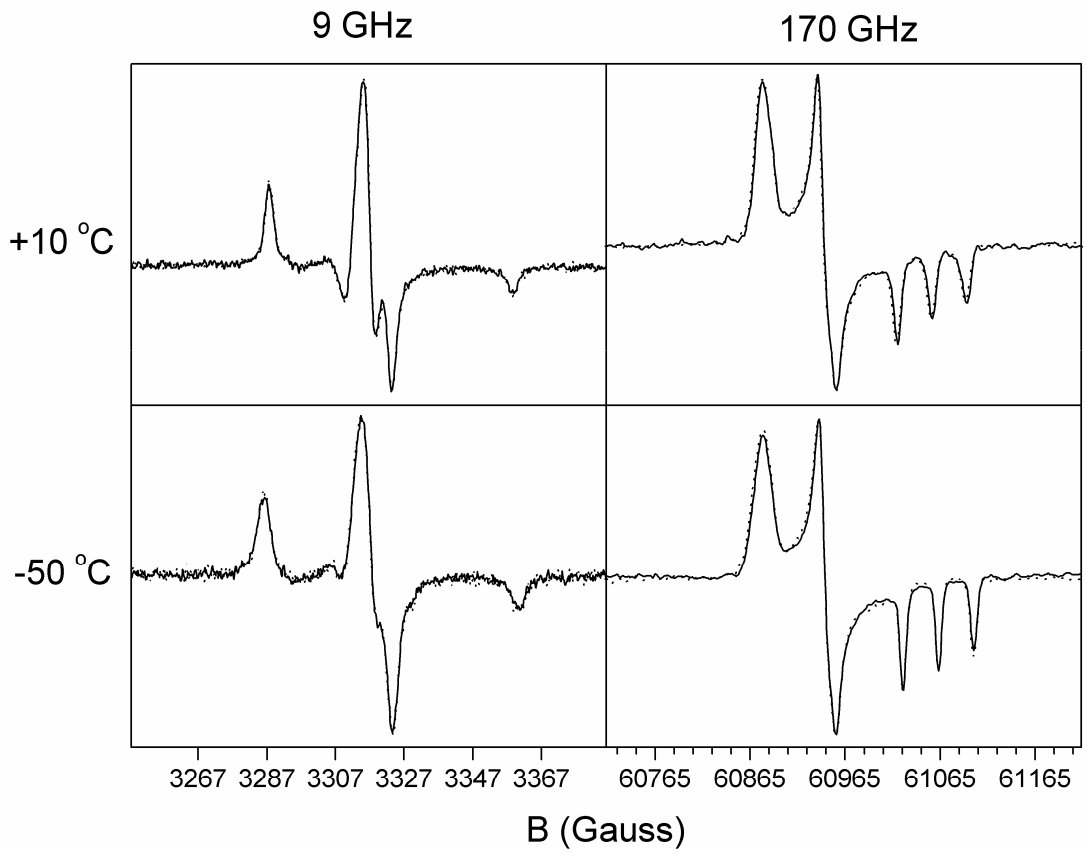

Figure 4-2. Comparison of spectra of 72R2 (solid line) and 131R2 (dashed line) recorded in 65 w/w% sucrose solution.

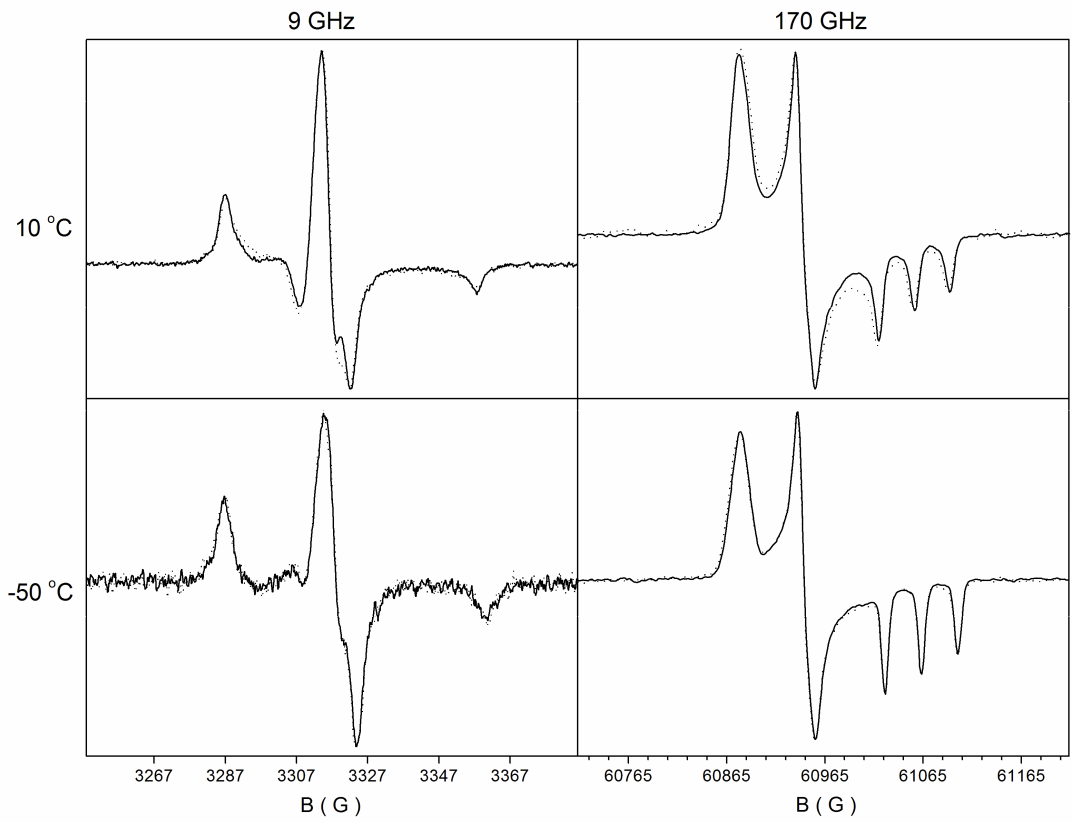

Figure 4-3. Comparison of spectra of 72R1 (solid line) and 131R1 (dashed line) recorded in 65 w/w% sucrose solution.

and the other is a relatively mobile one. Qualitatively simulations show that the population for the immobile component is ~65%, which is ~20% in water solution, suggesting that the equilibrium shifts ~45% to the immobile component in 65% sucrose. Some amounts (~35%) of either the intermediate or the mobile components still exist, and the difference in their motilities at site 72 and site 131 makes the spectra of 72R1 and 131R1 different at +10^{o}C in 65% sucrose solution. The equilibrium shift towards the immobile component in sucrose solution was also suggested by Guo by showing that 30% sucrose shifts the equilibrium towards the immobile component at some interacting surface sites of T4L (9). Guo explained this phenomenon by high osmotic pressure arising from the concentrated sucrose solution, resulting in the compression of the protein and increases in its intramolecular interactions. Such intramolecular interaction stabilizes the immobile component and makes it more favored.

At -50 ^{o}C, the sample is frozen since the glass transition temperature of the sucrose solution is -40^{o}C (100). In the glass one expects the motions of all components are extremely slow or frozen, so all spectra are the same for the different spin labels and sites, since they have same magnetic tensors.

4.4.2 Variations of Magnetic Tensor Components with Temperature

The 9 and 170 GHz spectra of the 4 mutants in 65 w/w% sucrose solution from -50 to +10^{o}C (i.e. -50, -35, -20, -5, and +10^{o}C) were simulated as rigid limit spectra by varying magnetic $\boldsymbol{A}$ and $\boldsymbol{g}$ tensors as well as $\boldsymbol{W}$ tensor, and the parameters obtained from the simulations are listed in Table 4-3. A_{zz} from the 9 GHz fits, $\boldsymbol{g}$ tensor components from the 170 GHz fits, and W_{zz} from fits at both frequencies vs temperature are plotted for all four samples in Figure 4-4. All the parameters in Figure 4-4 have good resolutions whereas the other parameters, including A_{xx}, A_{yy}, W_{xx}, and

Table 4-3. Best fit parameters (A_{xx}, A_{yy}, and A_{zz} from the 9 GHz fits, g_{xx}, g_{yy}, and g_{zz} from the 170 GHz fits, as well as W_{xx}, W_{yy}, and W_{zz} from fits at both frequencies)

Mutant	T (°C)	A_{xx} (G)	A_{yy} (G)	A_{zz} (G)	g_{xx}	g_{yy}	g_{zz}	W^{9}_{xx} (G)	W^{9}_{yy} (G)	W^{9}_{zz} (G)	W^{170}_{xx} (G)	W^{170}_{yy} (G)	W^{170}_{zz} (G)
72R1	-50	6.2	4.3	36.9	2.00839	2.00615	2.00232	2.6	2.2	2.4	5.5	3.8	3.2
	-35	6.1	4.5	36.6	2.00841	2.00615	2.00233	2.4	2.2	2.5	5.2	3.7	3.2
	-20	6.3	5.4	36.3	2.00838	2.00617	2.00244	2.1	1.8	2.0	4.4	3.5	3.6
	-5	6.2	5.6	35.7	2.00839	2.00618	2.00250	2.0	1.6	2.0	4.6	3.5	4.1
	10	6.4	6.6	35.1	2.00835	2.00614	2.00254	2.3	1.6	2.0	4.8	3.8	5.1
131R1	-50	5.9	4.1	37.0	2.00841	2.00616	2.00232	2.6	2.4	2.4	5.6	3.9	3.2
	-35	6.1	4.6	36.8	2.00842	2.00616	2.00233	2.3	2.2	2.5	5.2	3.7	3.3
	-20	6.3	5.5	36.3	2.00838	2.00618	2.00246	2.0	1.8	2.0	4.5	3.5	3.9
	-5	6.2	5.8	35.6	2.00838	2.00618	2.00255	2.1	1.7	2.1	4.8	3.9	4.7
	10	7.0	8.1	34.9	2.00833	2.00612	2.00260	2.8	1.8	2.4	5.3	4.4	6.0
72R2	-50	6.3	4.6	37.2	2.00841	2.00616	2.00231	2.6	2.2	2.3	5.3	3.6	3.1
	-35	6.3	4.4	36.9	2.00843	2.00616	2.00232	2.5	2.2	2.4	5.1	3.7	3.1
	-20	6.4	5.4	36.4	2.00841	2.00619	2.00244	2.0	1.5	1.7	4.3	3.5	3.4
	-5	6.5	5.6	35.9	2.00840	2.00618	2.00249	1.9	1.4	1.7	4.3	3.5	3.8
	10	6.4	5.9	35.4	2.00833	2.00614	2.00253	2.0	1.3	1.6	4.4	3.4	4.4
131R2	-50	6.3	4.6	37.1	2.00840	2.00615	2.00231	2.5	2.2	2.3	5.3	3.8	3.2
	-35	6.2	4.7	36.9	2.00842	2.00616	2.00233	2.5	2.2	2.3	4.9	3.7	3.2
	-20	6.5	5.4	36.5	2.00841	2.00619	2.00246	2.0	1.6	1.7	4.3	3.5	3.6
	-5	6.5	5.7	35.9	2.00838	2.00617	2.00250	1.9	1.4	1.6	4.3	3.6	3.9
	10	6.6	6.0	35.2	2.00834	2.00614	2.00256	2.1	1.3	1.6	4.3	3.6	4.5

Figure 4-4.

Variations of the best fit parameters (A_{zz} from the 9 GHz fits, g_{xx}, g_{yy}, and g_{zz} from the 170 GHz fits, as well as W_{zz} from fits at both frequencies) with temperature.

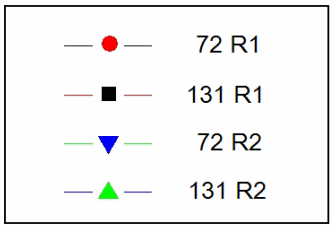

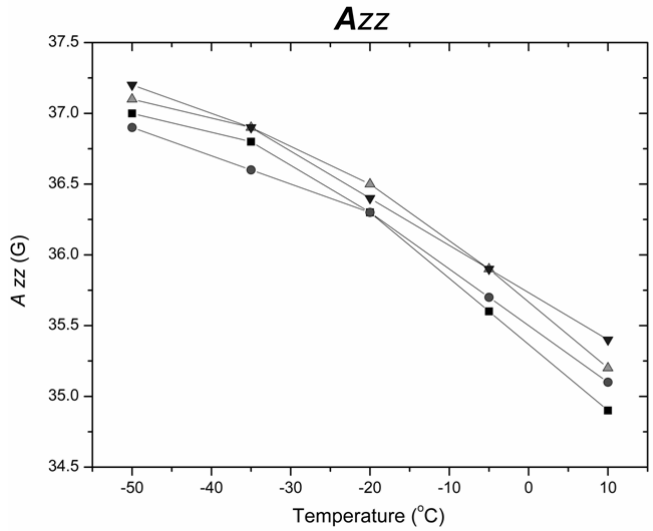
Azz
A zz (G)
37.5
37.0
36.5
36.0
35.5
35.0
34.5
-50
-40
-30
-20
-10
0
10
Temperature (°C)

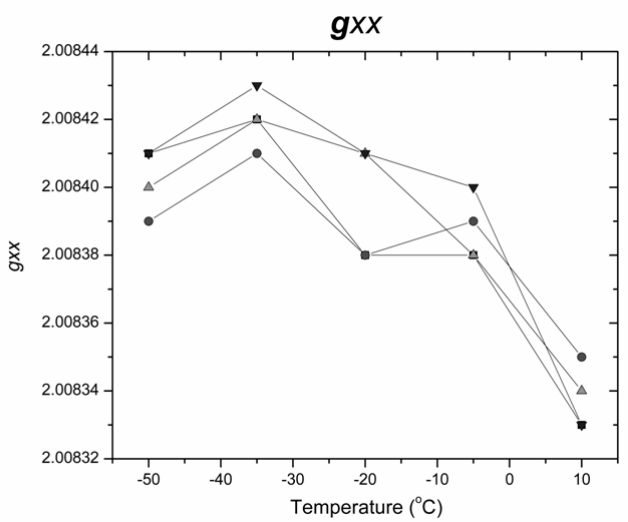
gxx
gxx
2.00844
2.00842
2.00840
2.00838
2.00836
2.00834
2.00832
-50
-40
-30
-20
-10
0
10
Temperature (°C)

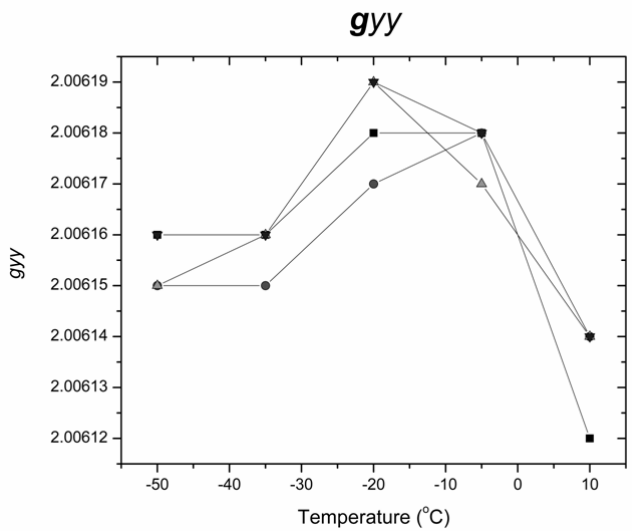
gyy
gyy
2.00619
2.00618
2.00617
2.00616
2.00615
2.00614
2.00613
2.00612
-50
-40
-30
-20
-10
0
10
Temperature (°C)

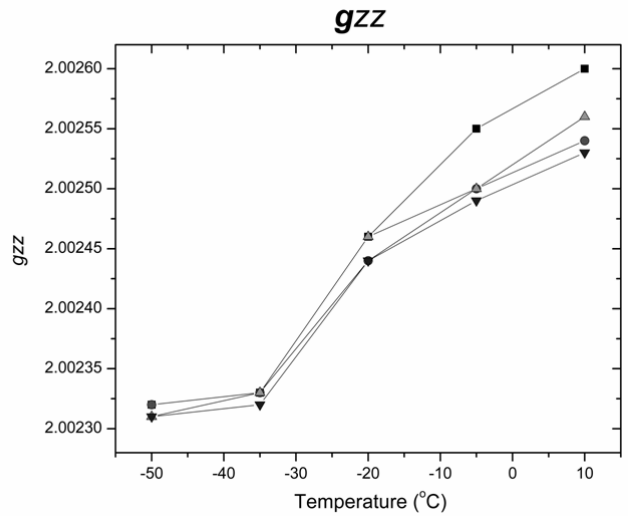
gzz
gzz
2.00260
2.00255
2.00250
2.00245
2.00240
2.00235
2.00230
-50
-40
-30
-20
-10
0
10
Temperature (°C)

Figure 4-4 (Continued)

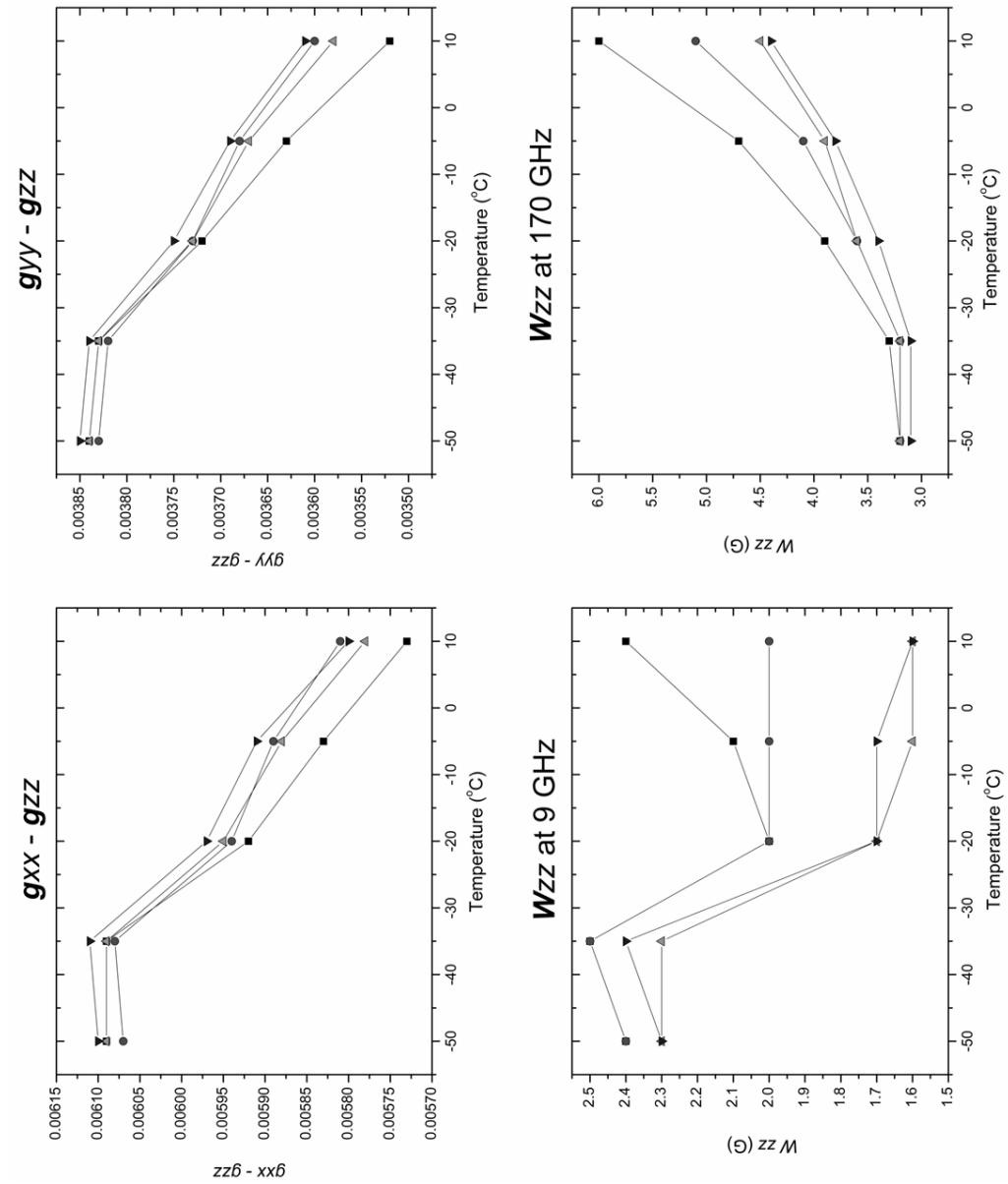

W_{yy} can not be determined very accurately and therefore are not plotted out. A comparison of g_{xx}, g_{yy}, and $\boldsymbol{A}$ tensor components from independent 170 GHz fitting and from dependent 170 GHz fitting with $\boldsymbol{A}$ tensor components from the 9 GHz fits is shown in Table 4-4. From the comparison in Table 4-4, it can be concluded that: (1) $\boldsymbol{g}$ tensor from the 170 GHz fitting is not influenced by different values for $\boldsymbol{A}$ tensor; (2) At -50 and -35^{o}C, the diffusion of the spin label is very slow and the same set of $\boldsymbol{A}$ tensor components can be used for fittings at both frequencies; (3) At higher temperatures, the diffusion of the spin label increases and is no longer slow enough. Thus, in the rigid limit fitting, different frequencies need different sets of $\boldsymbol{A}$ tensor components; (4) $\boldsymbol{A}$ tensor components average more at 9 GHz than at 170 GHz.

In Figure 4-4, g_{zz} shows a dramatic change from -35 to -20^{o}C. This can be explained by considering the glass transition temperature of the sucrose solution is -40^{o}C (100). When glass forms, "molecular motion is thought to be restricted to vibrations and short range rotational motions" (103).

From Figure 4-4, it is observed that the *Wzz* curves for 72R1 and 131R1 deviate from the normal trend. This can be explained by the poor fit for these two R1 labeled samples at temperatures above glass transition temperature especially at -5 and +10^{o}C. These spectra cannot be fitted well as rigid limit spectra.

4.4.3 Dynamics Models for the Internal Motion in High Viscous Solution

In the spectra of R2 from -50 to +10^{o}C, the deviations of magnetic tensors from the rigid limit ones are caused by the residual diffusion of the spin labeled tether.

The spectra of R2 from -50 to 10^{o}C can be fit as rigid limit spectra by varying magnetic and linewidth tensors. Above -50^{o}C, the deviations of magnetic tensors from the rigid limit ones are caused by the residual diffusion of the spin label. We made two assumptions for how the diffusion of the spin label varies with temperature: (1) The

Table 4-4. Comparison of fitting parameters (g_{xx}, g_{yy}, and $\boldsymbol{A}$ tensor components) for 72R2 with two methods of fitting at 170 GHz

	-50°C		-35°C		-20°C		-5°C		+10°C	
	I *	D **	I	D	I	D	I	D	I	D
gxx	2.0084	2.00841	2.00842	2.00843	2.00841	2.00841	2.00839	2.0084	2.00832	2.00833
gyy	2.00616	2.00616	2.00616	2.00616	2.00619	2.00619	2.00618	2.00618	2.00614	2.00614
Axx	6.4	6.3	6.4	6.3	6	6.4	5.9	6.5	6	6.4
Ayy	4.1	4.6	4.2	4.4	4.7	5.4	4.9	5.6	5	5.9
Azz	37.2	37.2	37	36.9	36.8	36.4	36.5	35.9	36.1	35.4

* I: Independent 170 GHz fitting

** D: Dependent 170 GHz fitting with $\boldsymbol{A}$ tensor components from the 9 GHz fitting

diffusion is very slow but with no ordering. In this assumption, the diffusion rate (R^o) increases when temperature increases; (2) The diffusion rate is relatively fast, but the ordering is considered and can be very high. In this case, the ordering (S_{20}) decreases when temperature increases. For assumption (1), we performed some simulations with all kinds of symmetries for the $\boldsymbol{R^0}$ tensor. For assumption (2), we performed some simulations with *x*-, *y*-, and *z*- ordering. For both assumptions, the 9 and 170 GHz spectra were simulated. In the simulation, the $\boldsymbol{g}$, $\boldsymbol{A}$, and $\boldsymbol{W}$ tensors are taken from the best fit parameters for 72R2 at -50°C (cf. Table 4-3). The center field which corresponds to $g_{\text{average}} = 1/3 * (g_{xx} + g_{yy} + g_{zz})$ is set to 60953.54 G. The magnetic field for g_{xx}, g_{yy}, g_{zz}, and A_{zz} are measured directly from the simulated spectra. The change of g_{xx}, g_{yy}, g_{zz}, and A_{zz} with either the diffusion rate for assumption (1) or the ordering parameter for assumption (2) is compared with the change of these parameters with temperature from the best fits to the experimental data in Figures 4-5 and 4-6 respectively. The fitting parameters for 72R2 are used in Figures 4-5 and 4-6 because spectra for R2 can be fitted with only one component and can be fitted well as near rigid limit spectra throughout the whole temperature range. Therefore, its motion is assumed to be simpler than that of R1 even at low temperatures. g_{xx}, g_{yy}, g_{zz}, and A_{zz} at 170 GHz are taken from the independent 170 GHz fitting (cf. Table 4-3 and 4-4), while A_{zz} at 9 GHz is taken from the 9 GHz fitting (cf. Table 4-3).

In the first assumption, the order parameters were set to zero. Values for R_x, R_y and R_z were set in the range of 10^5 s^{-1} to 10^7 s^{-1}. Totally 13 cases were simulated with different relations among R_x, R_y and R_z. Both axial and rhombic symmetries are considered. The various relations are listed in Table 4-5. From comparison, three cases, 5, 10, and 11 can be regarded as poor models because of their relatively small change in g_{zz} and A_{zz}, which is not agreed with the fits to the experimental data.

Table 4-5. List of 13 Cases for the first assumption

Case No.	Quantitive Relation among *Rx*, *Ry*, and *Rz*	Qualitative Relation among *Rx*, *Ry*, and *Rz*
1	$Rx = Ry = Rz$	$Rx = Ry = Rz$
2	$Rx = Ry = 10*Rz$	$Rx = Ry > Rz$
3	$Rx = 3*Ry = 17*Rz$	$Rx > Ry > Rz$
4	$Ry = 3*Rx = 17*Rz$	$Ry > Rx > Rz$
5	$Rz = 10*Ry = 10*Rx$	$Rz > Rx = Ry$
6	$Ry = 10*Rz = 10*Rx$	$Ry > Rz = Rx$
7	$Rx = 10*Ry = 10*Rz$	$Rx > Ry = Rz$
8	$Rx = Rz = 10*Ry$	$Rx = Rz > Ry$
9	$Ry = Rz = 10*Rx$	$Ry = Rz > Rx$
10	$Rz = 6*Ry = 17*Rx$	$Rz > Ry > Rx$
11	$Rz = 6*Rx = 17*Ry$	$Rz > Rx > Ry$
12	$Ry = 3.2*Rz = 10*Rx$	$Ry > Rz > Rx$
13	$Rx = 3.2*Rz = 10*Ry$	$Rx > Rz > Ry$

Figure 4-5.

Compare the best fit parameters from fitting the experimental data of 72R2 (circular symbol) to g_{xx}, g_{yy}, g_{zz}, A_{zz} from the simulated 170 GHz spectra, and A_{zz} from the simulated 9 GHz spectra for the 13 cases of the first assumption (square symbol). In each page, from top to bottom are g_{xx}, g_{yy}, g_{zz}, A_{zz} at 9 GHz, and A_{zz} at 170 GHz. Each case takes up a column and the sequence is from case 1 to case 13.

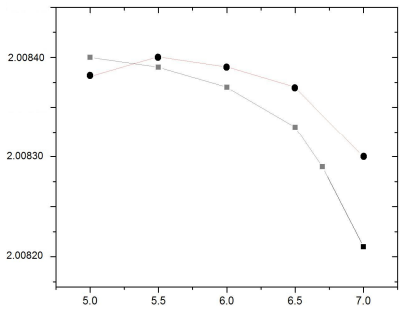
2.00840
2.00830
2.00820
5.0
5.5
6.0
6.5
7.0

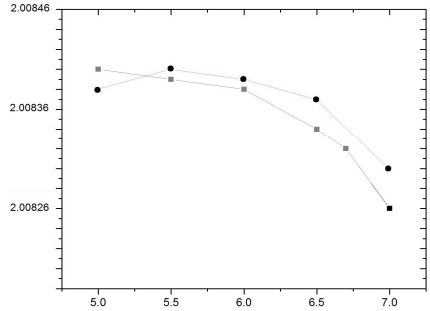
2.00846
2.00836
2.00826
5.0
5.5
6.0
6.5
7.0

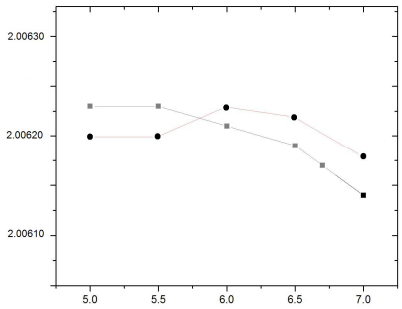
2.00630
2.00620
2.00610
5.0
5.5
6.0
6.5
7.0

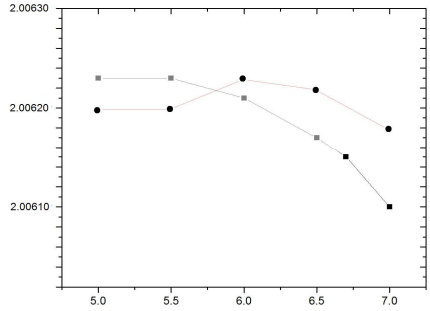
2.00630
2.00620
2.00610
5.0
5.5
6.0
6.5
7.0

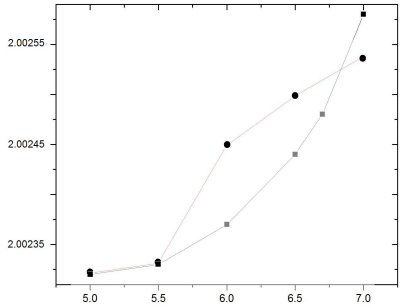
2.00255
2.00245
2.00235
5.0
5.5
6.0
6.5
7.0

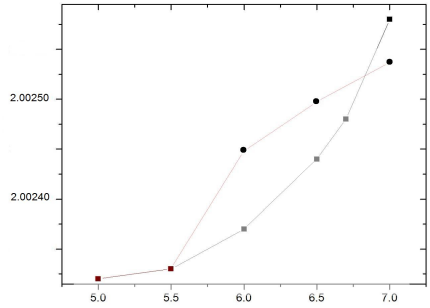
2.00250
2.00240
5.0
5.5
6.0
6.5
7.0

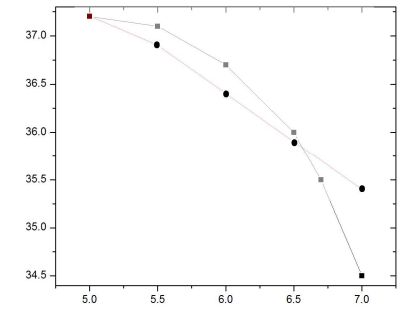
37.0
36.5
36.0
35.5
35.0
34.5
5.0
5.5
6.0
6.5
7.0

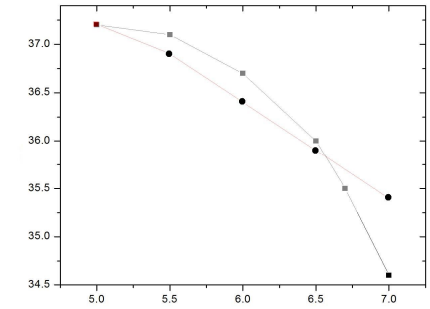
37.0
36.5
36.0
35.5
35.0
34.5
5.0
5.5
6.0
6.5
7.0

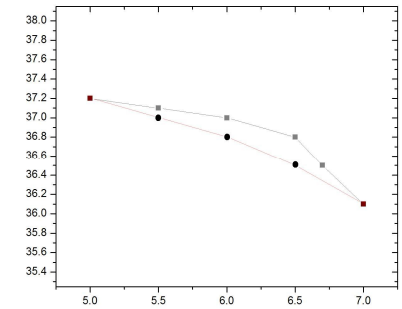
38.0
37.8
37.6
37.4
37.2
37.0
36.8
36.6
36.4
36.2
36.0
35.8
35.6
35.4
5.0
5.5
6.0
6.5
7.0

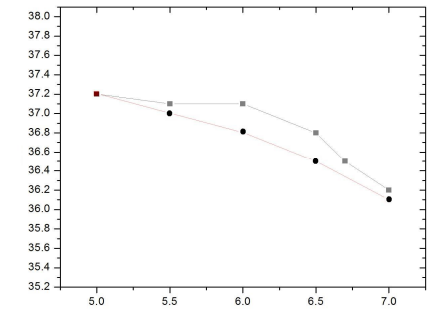
38.0
37.8
37.6
37.4
37.2
37.0
36.8
36.6
36.4
36.2
36.0
35.8
35.6
35.4
35.2
5.0
5.5
6.0
6.5
7.0

Figure 4-5 (Continued)

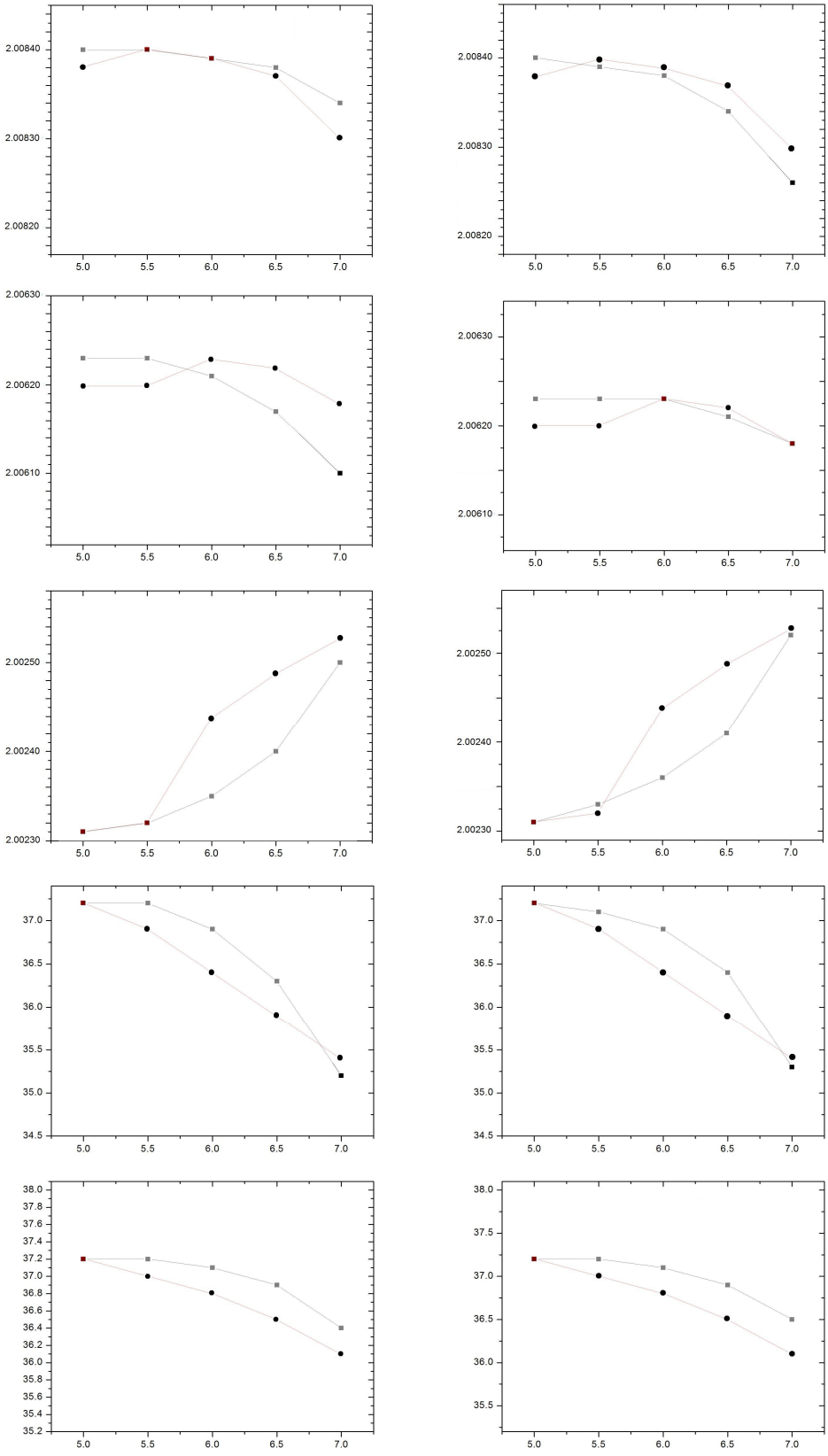

Figure 4-5 (Continued)

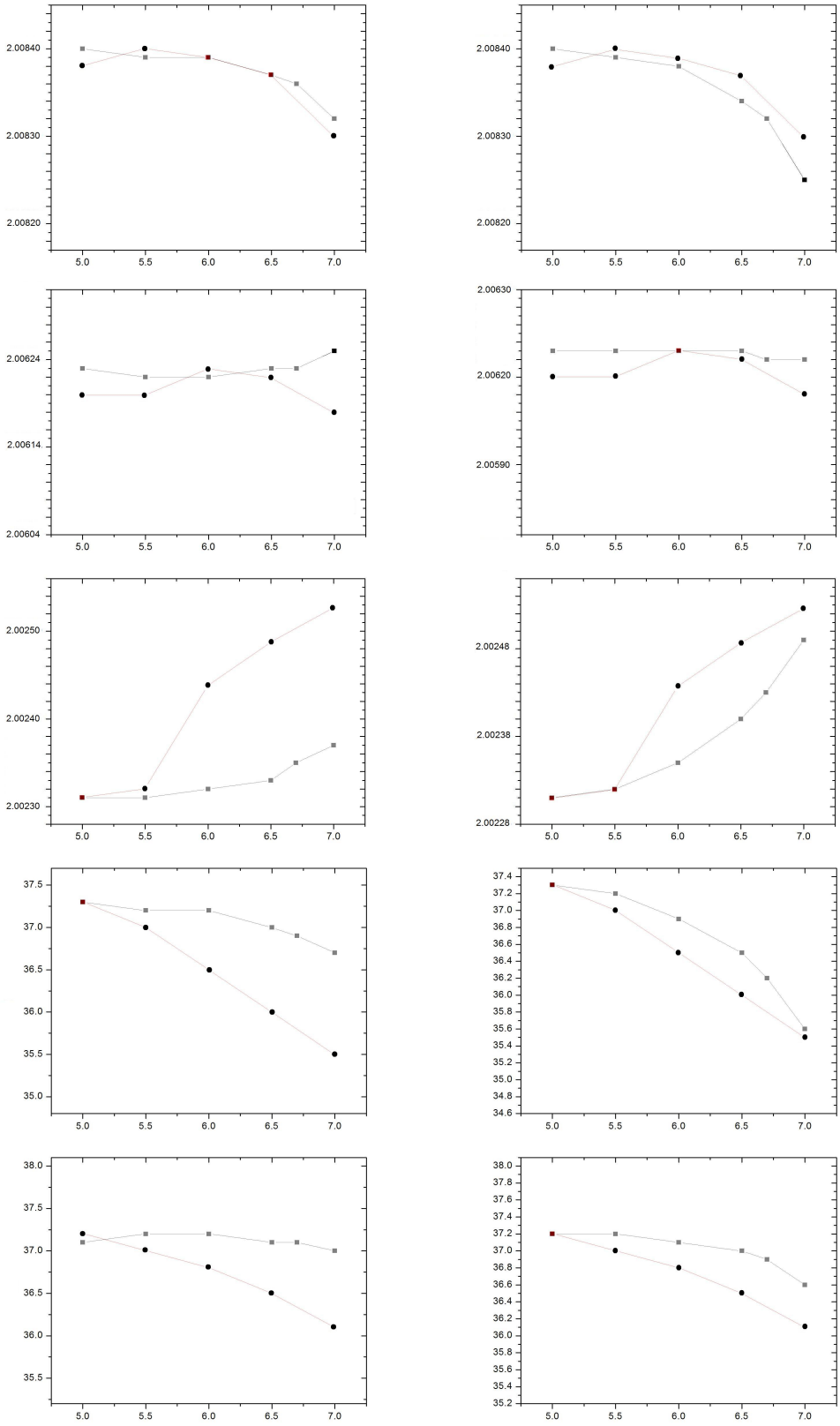

Figure 4-5 (Continued)

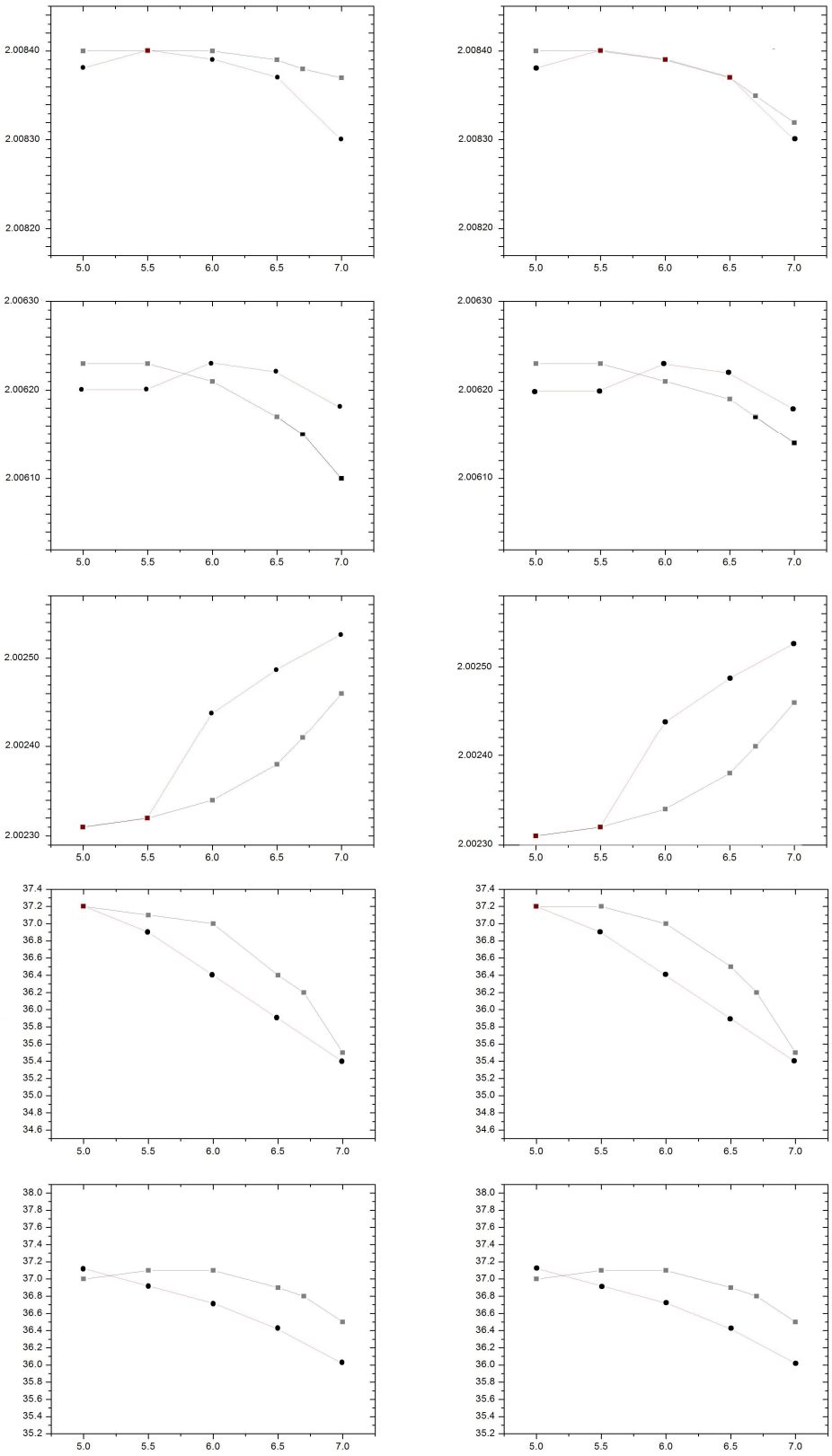

Figure 4-5 (Continued)

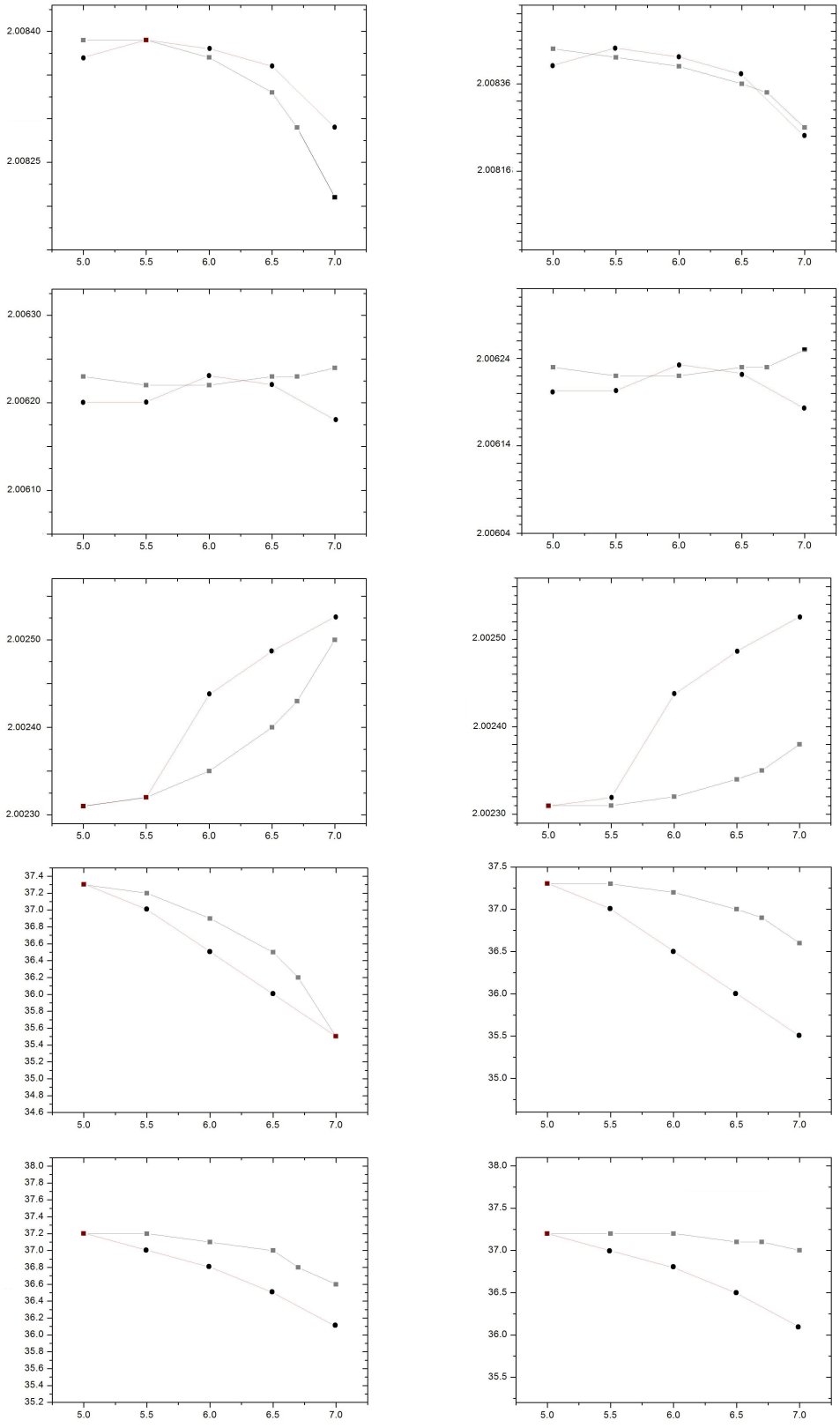

Figure 4-5 (Continued)

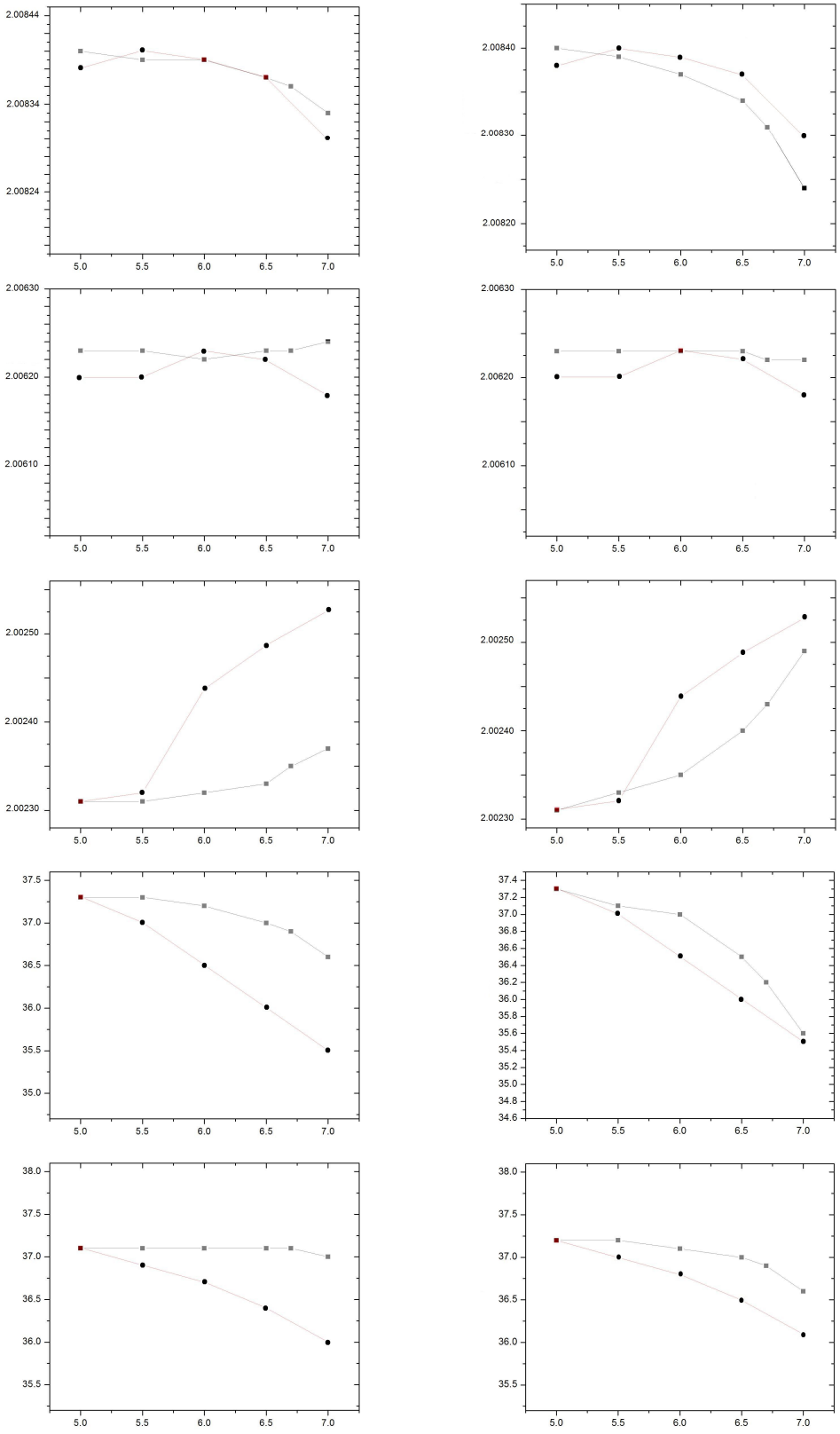

Figure 4-5 (Continued)

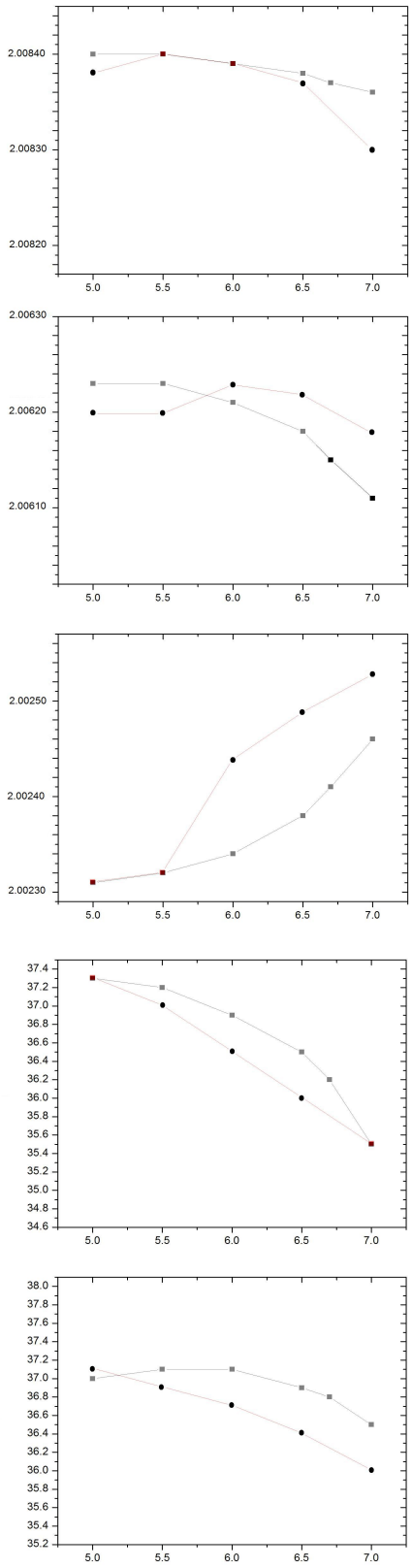

Figure 4-6.

Compare the best fit parameters from fitting the experimental data of 72R2 (circular symbol) to g_{xx}, g_{yy}, g_{zz}, A_{zz} from the simulated 170 GHz spectra, and A_{zz} from the simulated 9 GHz spectra for the *x*-, *y*-, and *z*- ordering of the second assumption (square symbol). In each page, from top to bottom are g_{xx}, g_{yy}, g_{zz}, A_{zz} at 9 GHz, and A_{zz} at 170 GHz. Each type of ordering takes up a column and the sequence is from *x*- to *y*- to *z*- ordering.

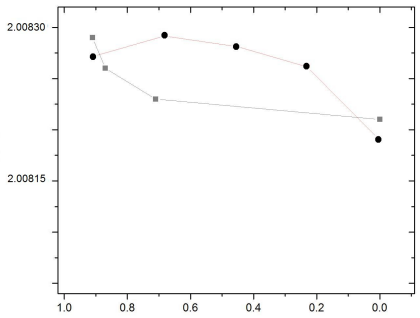
2.00830
2.00815
1.0 0.8 0.6 0.4 0.2 0.0

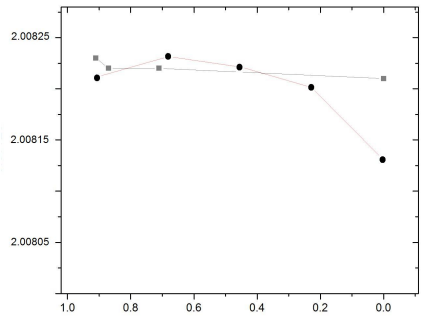
2.00825
2.00815
2.00805
1.0 0.8 0.6 0.4 0.2 0.0

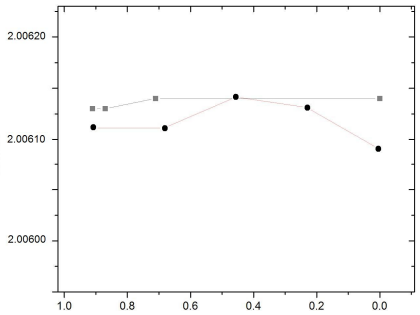
2.00620
2.00610
2.00600
1.0 0.8 0.6 0.4 0.2 0.0

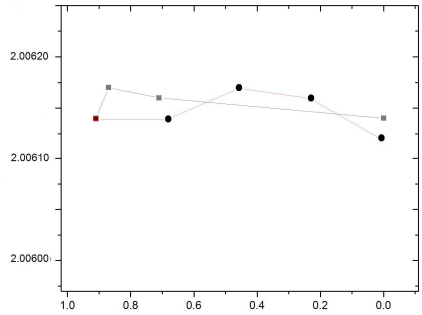
2.00620
2.00610
2.00600
1.0 0.8 0.6 0.4 0.2 0.0

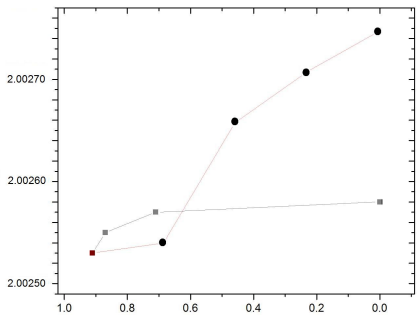
2.00270
2.00260
2.00250
1.0 0.8 0.6 0.4 0.2 0.0

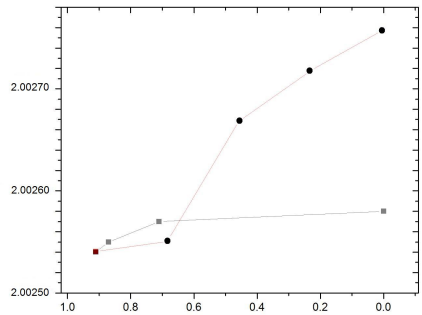
2.00270
2.00260
2.00250
1.0 0.8 0.6 0.4 0.2 0.0

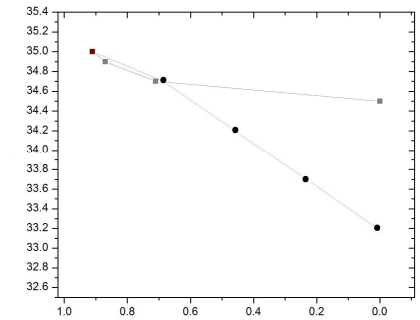
35.4
35.2
35.0
34.8
34.6
34.4
34.2
34.0
33.8
33.6
33.4
33.2
33.0
32.8
32.6
1.0 0.8 0.6 0.4 0.2 0.0

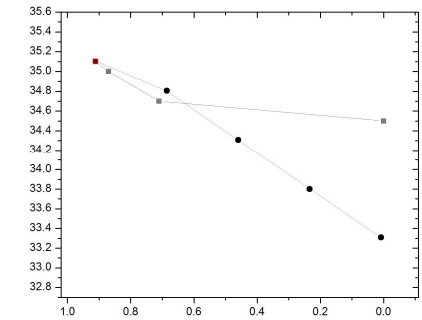
35.6
35.4
35.2
35.0
34.8
34.6
34.4
34.2
34.0
33.8
33.6
33.4
33.2
33.0
32.8
1.0 0.8 0.6 0.4 0.2 0.0

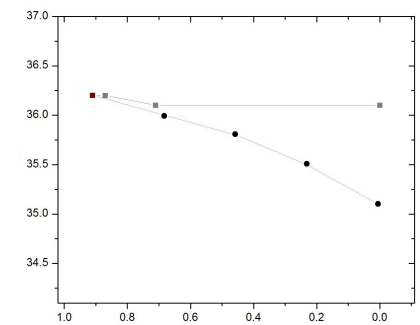
37.0
36.5
36.0
35.5
35.0
34.5
1.0 0.8 0.6 0.4 0.2 0.0

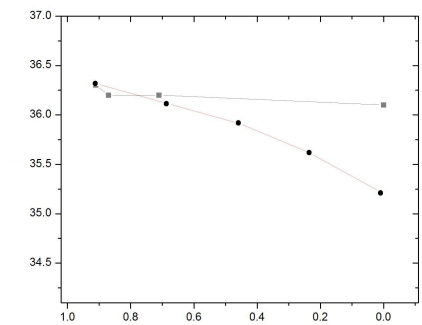
37.0
36.5
36.0
35.5
35.0
34.5
1.0 0.8 0.6 0.4 0.2 0.0

Figure 4-6 (Continued)

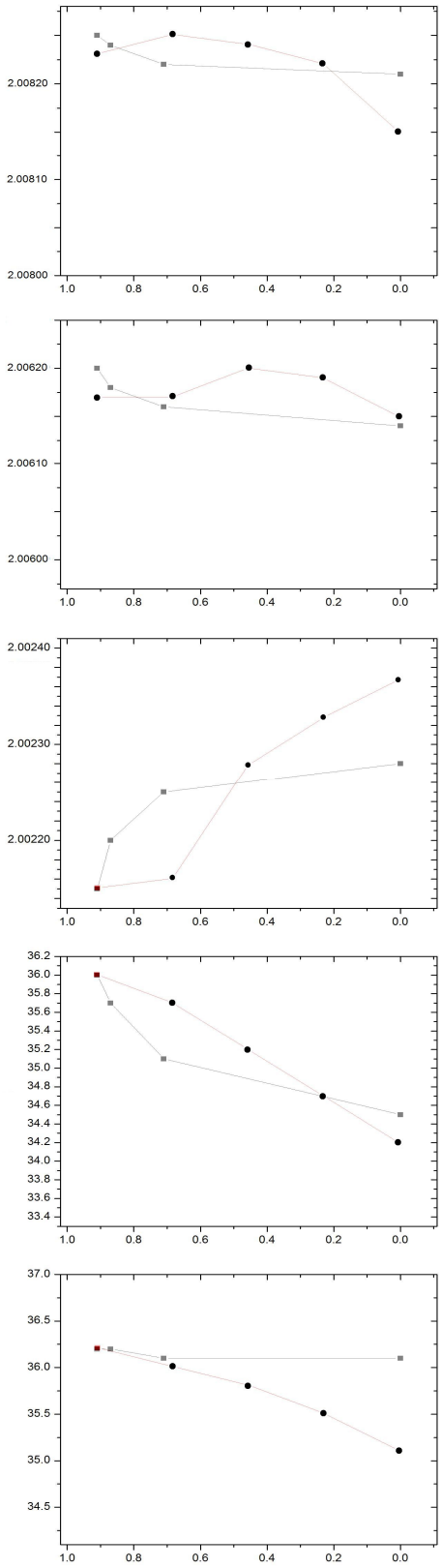

As a conclusion, if the symmetry is axial, $R_{\parallel}$ cannot be much larger than $R_{\perp}$; if the symmetry is rhombic, R_z cannot be much larger than both R_x and R_y.

In the second assumption, the rotational diffusion rate (R^o) is set to 10^7 s^{-1}. Axial symmetry is assumed for $\boldsymbol{S}$, and *x*-, *y*-, and *z*- ordering are all considered. The ordering parameter (S_{20}) varies in a range of 0 to 0.9. From comparison, *z*-ordering model is found to be much better than *x*- and *y*- ordering models.

Consistently, our results in water and Ficoll solutions [cf. Chapter 2 and 3] show that: (1) $R^o_{\parallel}$ is either much smaller than or close to $R^o_{\perp}$; (2) The diffusion of the spin label is *z*-ordering.

4.5 CONCLUSIONS

The main findings are the following:

(1) The $\boldsymbol{g}$ tensor and hyperfine tensor for all four spin labeled mutants obtained from the rigid limit multifrequency spectra (at low temperature and in viscous sucrose/water solution) are identical within the experimental uncertainty, indicating that they are all in very similar polarity environments.

(2) By comparing the change of the $\boldsymbol{g}$ tensor in the simulated 170 GHz spectrum and A_{zz} in the simulated 9 and 170 GHz spectrum with the change of these tensor components in the experimental spectra, we reached the following conclusions: 1) $R^o_{\parallel}$ cannot be greater than $R^o_{\perp}$; 2) The *z*-ordering model is much better than the *x*- and *y*- ordering models.

(3) These observations in high concentration sucrose solution are consistent with our results in water and Ficoll solutions which show that: 1) $R^o_{\parallel}$ is typically much smaller than or close to $R^o_{\perp}$; 2) The internal diffusion of the spin label shows *z*-ordering.

CHAPTER 5

CONCLUSIONS AND PERSPECTIVES

5.1 CONCLUSIONS

In this section, I will summarize the results and conclusions we obtained from this dissertation.

The major findings are as follows:

(1) Very good simultaneous fits have been achieved for all four-frequency spectra at all temperatures using the SRLS model.

(2) The values for overall tumbling rate, R^c obtained independently from each of the four spin labeled mutants were generally in very good agreement with each other and agree favorably with estimates from NMR and hydrodynamic modeling. This supports the results of the SRLS analysis.

(3) The best global fits using data from four frequencies on T4 lysozyme in aqueous solution require three spectral components characterized as relatively "mobile", "intermediate", and "immobile" for both 72R1 and 131R1. In the case of 72R2 and 131R2 only the "intermediate" and "immobile" components were found. These results clearly demonstrate the multi-component nature of the spectra.

(4) To further distinguish side chain isomerizations of the tether and backbone fluctuations, additional experiments would be necessary (cf. Section 5.2).

(5) The $\boldsymbol{g}$ tensor and hyperfine tensor for all four spin labeled mutants measured from rigid-limit multifrequency spectra (in low temperature viscous sucrose/water solution) are identical within experimental uncertainty indicating they are all in very similar polarity environments.

(6) The experimental results, and their SRLS analysis, show some key similarities with the predictions of Tombolato et al. from their dynamic modeling.

Some additional findings are as follows:

(1) The "immobile" component is highly ordered and slower in its motion and is more populated in the R2 spectra. This component may correspond to conformers stabilized by interaction with the protein surface.

(2) The "intermediate" and "mobile" components exhibit fast anisotropic local diffusion and relatively low ordering. They most likely correspond to conformers having little or no interactions with nearby residues.

(3) The more mobile components of 72R1 and 131R1 exhibit significantly different S_{20} values, with that for 72R1 being significantly greater, as is consistent with previous studies which suggested that this difference results from reduced backbone flexibility for 72R1.

(4) The addition of Ficoll reduces R^c according to a microscopic viscosity that is proportional to the macroscopic viscosity taken to the ~ 0.4 power; it also slows down the internal motion of the immobile component of R2.

5.2 PERSPECTIVES

In this dissertation, we leave unresolved the question whether ESR can be a good tool to distinguish different ordered backbone segments (e.g. helices with different length and rigidity). In order to focus more on the contribution from the backbone fluctuations in the future studies, better designed spin labels are necessary. For example, a spin label with more constrained motion about its tether should be developed. In fact, the application of R2 (4-methyl-MTSSL) in this work was for this purpose, although no clear conclusions were drawn from the results on R2. Spin labels

with even more constrained tether motion, e.g. 4-bromo-MTSSL and 4-phenyl-MTSSL, have been applied by Fleissner et al. to label T4 lysozyme so that the spectra are mainly affected by the backbone fluctuations (34, 37). In addition, a novel cross-linked nitroxide spin label has been designed to attach to two neighboring residues so that the flexibility from the spin label tether is even more restricted and only motion from the backbone can be observed (37).

Besides applying more restricted spin labels, several new methods have been tested to study the backbone fluctuations, e.g. to mutate a residue which is not adjacent to the spin labeled site but on the same secondary structure (e.g. helix) so that any observable change in the spectral lineshape can be attributed to the change in mobility of the backbone (WL Hubbell, private communication).

With such novel spin labels and methods, as a complement to the multifrequency ESR method for separating the overall tumbling of the protein, the backbone fluctuations and the side chain isomerizations with similar time scales can be further separated.

APPENDICES

Appendix I. The Modified SRLS Model Program for Searching for the Population of Each Component with the Linear Least Squares (LLS) Minimization in the Multifrequency Fitting

(The sections modified in the Fortran program are highlighted.)

sscalenew.f

(This modified subroutine is for 72R2 at 2 ^{o}C in water solution. $\sigma_{9\ GHz}$ / σ_{j} is respectively 1, 6, and 23 for j = 9, 95, and 170 GHz.)

```
c  NLSL Version 1.3 7/17/93
c-----------------------------------------------------------------------
c               =========================
c                 subroutine SSCALENEW
c               =========================
c
c   Given the array <data> with <npt> data points and a matrix of <nsite>
c   calculated spectra, each with <npt> points, calculate a least-squares
c   set of <nsite> scaling factors. This routine uses the QR factorization
c   routine that belongs to MINPACK together with the associated routines
c   for solving the least-squares problem using QR factoriaation.
c
c   Inputs:
c      data(npt)         Data values to be fit by scaled spectra
c      spectr(ldspct,nsi) Spectrum/spectra to be scaled
c      ldspct             Leading dimension of spectr array
c      nsite              # spectra contained in spectr array
c      npt                # points in data/spectra arrays
c      ctol               Tolerance for linearly independent components
c      iscal              Flags =1 for automatic scaling of each site
c                        (otherwise used fixed value passed in sfac)
c      noneg               Flag =1: zero any negative coeffients
c      work(npt)          Temporary work array used in QR solution
c
c    Output:
c      sfac               Array of scaling factors
c                        Scale factors corresponding to spectra that
c                        were eliminated on the basis of linear dependence
c                        or were negative (if noneg=1)
```

```
c
c      resid             Residuals (data minus scaled calculated spectra)
c
c   Includes:
c     nlsdim.inc
c
c   Uses:
c     qrfac    Calculate QR factorization of design matrix (MINPACK)
c     qtbvec   Calculate Q(transpose)*b from Householder transformations
c     rsolve   Solve R*x = Q(transpose)*b
c     dchex    Update QR factors for column permutation of design matrix
c
c-----------------------------------------------------------------------
      subroutine sscalenew( data,spct,wspct,ldspct,work,nsite,npt,ctol,
     #                  noneg,iscal,sfac,resid )
      implicit none
c
      integer ldspct,noneg,npt,nsite
      integer iscal(nsite)
      double precision data(npt),work(npt),spct(ldspct,nsite),
     #                 wspct(ldspct,nsite),resid(npt),sfac(nsite),ctol
c
      include 'nlsdim.inc'
c
      integer ixspc(MXSITE),jpvt(MXSITE)
      double precision qtd(MXSITE),qraux(MXSITE),rdiag(MXSITE),
     #                 tmpfac(MXSITE),wa1(MXSITE),wa2(MXSITE)
c
      integer i,info,j,jtmp,k,m,mneg,nscl
      double precision smin,sumc2,sumdc,tmp
c
      double precision ZERO
      parameter (ZERO=0.0d0)
c
c
c#############################################################################
c
c --- NEW ---
      do i=1,512
      data(i)=data(i)
      spct(i,1)=spct(i,1)
      spct(i,2)=spct(i,2)
      spct(i,3)=spct(i,3)
      end do
      do i=513,1024
      data(i)=data(i)*6
      spct(i,1)=spct(i,1)*6
      spct(i,2)=spct(i,2)*6
      spct(i,3)=spct(i,3)*6
      end do
      do i=1025,1536
      data(i)=data(i)*23
```

```
      spct(i,1)=spct(i,1)*23
      spct(i,2)=spct(i,2)*23
      spct(i,3)=spct(i,3)*23
      end do
c --- NEW ---
c
      do j=1,npt
        resid(j)=data(j)
      end do
c
c     ----------------------------------------------------------------
c     Copy any spectra with the autoscale flag set to the work array
c     Subtract spectra with fixed scale factors from the residuals
c     ----------------------------------------------------------------
      nscl=0
      do i=1,nsite
        if (iscal(i).ne.0) then
          nscl=nscl+1
          ixspc(nscl)=i
          do j=1,npt
            wspct(j,nscl)=spct(j,i)
          end do
        else
          do j=1,npt
            resid(j)=resid(j)-sfac(i)*spct(j,i)
          end do
        end if
      end do
c
      if (nscl.eq.0) return
c
c-----------------------------------------------------------------------
c     If there is only one site, calculate the least-squares
c     scaling factor directly
c-----------------------------------------------------------------------
      if (nscl.eq.1) then
c
        sumdc=ZERO
        sumc2=ZERO
        do i=1,npt
          sumdc=sumdc+resid(i)*wspct(i,1)
          sumc2=sumc2+wspct(i,1)*wspct(i,1)
        end do
c
        if (sumc2.ne.ZERO) then
          tmpfac(1)=sumdc/sumc2
        else
          tmpfac(1)=ZERO
        end if
c
c-----------------------------------------------------------------
c     For multiple sites, use QR decomposition to find linear
```

```
c     least-squares scaling coefficients and rms deviation
c-------------------------------------------------------------
      else
c
c       ---------------------------------------------
c       Compute the QR factorization of the spectra
c       ---------------------------------------------
        call qrfac(npt,nscl,wspct,ldspct,.true.,jpvt,nscl,rdiag,
     #       wa1,wa2)
c
        do i=1,nscl
          qraux(i)=wspct(i,i)
          wspct(i,i)=rdiag(i)
        end do
c
c       ---------------------------------------------------------
c       Determine which spectra are linearly dependent and remove them
c       from the problem
c       ---------------------------------------------------------
        k=0
        do i=1,nscl
          if (dabs(rdiag(i)) .le. ctol*dabs(rdiag(1)) ) goto 14
          k=i
        end do
c
 14     call qtbvec(npt,k,wspct,ldspct,qraux,data,work)
c
c       ---------------------------------------------------------
c       Loop to here if QR factorization has been updated
c       to eliminatespectra entering with negative coefficients
c       ---------------------------------------------------------
c
 15     call rsolve( npt,k,wspct,ldspct,qraux,work,tmpfac,
     #              .false.,tmp )
c
c       ---------------------------------------------------------
c       Optional check for negative coefficients: permute spectra
c       with negative coefficients into the truncated part of the QR
c       factorization and re-solve the problem
c       (But don't truncate the last spectrum!)
c       ---------------------------------------------------------
        if (noneg.ne.0.and.k.gt.1) then
          smin=ZERO
          mneg=0
          do i=1,k
            if (tmpfac(i).lt.smin) then
              mneg=i
              smin=tmpfac(i)
            end if
          end do
c
          if (mneg.ne.0) then
```

```
            if (mneg.lt.k) then
              call dchex( wspct,ldspct,nscl,mneg,k,
     #                    work,ldspct,1,wa1,wa2,2 )
c
              jtmp=jpvt(mneg)
              do j=mneg,k-1
                jpvt(j)=jpvt(j+1)
              end do
              jpvt(k)=jtmp
            end if
            k=k-1
            go to 15
          end if
        end if
c
c     ------------------------------------------------------------
c     Set the unused components of tmpfac to zero and initialize jpvt
c     for unscrambling scaling coefficients from pivoted order
c     ------------------------------------------------------------
        do i=1,nscl
          jpvt(i)=-jpvt(i)
          if (i.gt.k) tmpfac(i)=ZERO
        end do
c
c     ----------------------------------------------------
c     Unscramble the solution from pivoted order using jpvt
c     ----------------------------------------------------
        do 70 i=1,nscl
          if (jpvt(i).le.0) then
            k=-jpvt(i)
            jpvt(i)=k
c
 50           if (k.eq.i) goto 70
            tmp=tmpfac(i)
            tmpfac(i)=tmpfac(k)
            tmpfac(k)=tmp
            tmp=rdiag(i)
            rdiag(i)=rdiag(k)
            rdiag(k)=tmp
            jpvt(k)=-jpvt(k)
            k=jpvt(k)
            go to 50
          end if
 70     continue
c
c           *** End if (nscl.eq.1) ... else ...
      end if
c
c     ----------------------------------------------------
c     Calculate residuals using least-squares scale factors
c     ----------------------------------------------------
c
```

```
c --- NEW ---
      do i=1,512
      data(i)=data(i)
      spct(i,1)=spct(i,1)
      spct(i,2)=spct(i,2)
      spct(i,3)=spct(i,3)
      end do
      do i=513,1024
      data(i)=data(i)/6
      spct(i,1)=spct(i,1)/6
      spct(i,2)=spct(i,2)/6
      spct(i,3)=spct(i,3)/6
      end do
      do i=1025,1536
      data(i)=data(i)/23
      spct(i,1)=spct(i,1)/23
      spct(i,2)=spct(i,2)/23
      spct(i,3)=spct(i,3)/23
      end do
c
      do j=1,npt
        resid(j)=data(j)
      end do
c --- NEW ---
c
      do i=1,nscl
        k=ixspc(i)
        sfac(k)=tmpfac(i)
        do j=1,npt
          resid(j)=resid(j)-sfac(k)*spct(j,k)
        end do
      end do
c
      return
      end
```

Appendix II. Error Estimation for the Best Fit Parameters in Table 2-2 and 3-2

72R2 at 2°C in water solution

9 + 95 + 170 GHz

		Table 2-2	Initial Value = Table 2-2 – 10%		Initial Value = Table 2-2 + 10%	
			Best Fit	Error	Best Fit	Error
Comp 2	$R^{o}_{\perp}$ (10^{7} s^{-1})	33.1	32.4	2%	34.7	5%
	c_{20}	2.91	2.94	1%	2.96	2%
	S_{20}	0.57	0.57	0	0.58	0.01
	Population (%)	27	26~27 (<= 1%)			
Comp 1	$R^{o}_{\perp}$ (10^{7} s^{-1})	4.3	4.2	2%	4.3	0%
	c_{20}	3.41	3.53	4%	3.58	5%
	S_{20}	0.65	0.67	0.02	0.67	0.02
	Population (%)	73	74~73 (<= 1%)			
	R^{c} (10^{7} s^{-1})	0.69	0.74	7%	0.74	7%

131R2 at 2°C in water solution

9 + 95 + 170 + 240 GHz

		Table 2-2	Initial Value = Table 2-2 – 10%		Initial Value = Table 2-2 + 10%	
			Best Fit	Error	Best Fit	Error
Comp 2	$R^{o}_{\perp}$ (10^{7} s^{-1})	42.7	42.7	0%	43.7	2%
	c_{20}	2.81	2.83	1%	2.85	1%
	S_{20}	0.57	0.58	0.01	0.58	0.01
	Population (%)	44	44~46 (<= 2%)			
Comp 1	$R^{o}_{\perp}$ (10^{7} s^{-1})	9.1	8.9	2%	9.1	0%
	c_{20}	3.73	3.9	5%	3.93	5%
	S_{20}	0.68	0.69	0.01	0.70	0.02
	Population (%)	56	56~54 (<= 2%)			
	R^{c} (10^{7} s^{-1})	0.68	0.63	7%	0.66	3%

131R2 at 32°C in water solution

9 + 95 + 170 + 240 GHz

		Table 2-2	Initial Value = Table 2-2 – 10%		Initial Value = Table 2-2 + 10%	
			Best Fit	Error	Best Fit	Error
Comp 2	$R^{o}_{\perp}$ (10^{7} s^{-1})	67.6	66.1	2%	70.8	5%
	c_{20}	2.75	2.72	1%	2.73	1%
	S_{20}	0.55	0.55	0	0.55	0
	Population (%)	65	63~66 (<=2%)			
Comp 1	$R^{o}_{\perp}$ (10^{7} s^{-1})	15.8	16.2	3%	16.2	3%
	c_{20}	3.60	3.61	0%	3.69	2%
	S_{20}	0.66	0.66	0	0.67	0.01
	Population (%)	35	34~37 (<=2%)			
	R^{c} (10^{7} s^{-1})	1.78	1.78	0%	1.82	2%

131R2 at 2°C in 15% Ficoll solution

9 + 95 + 170 GHz

		Table 3-2	Initial Value = Table 3-2 – 10%		Initial Value = Table 3-2 + 10%	
			Best Fit	Error	Best Fit	Error
Comp 2	$R^{o}_{\perp}$ (10^{7} s^{-1})	42.7	39.8	7%	43.7	2%
	c_{20}	2.97	3.01	1%	3.03	1%
	S_{20}	0.6	0.6	0	0.61	0.01
	Population (%)	37	37~38 (<= 1%)			
Comp 1	$R^{o}_{\perp}$ (10^{7} s^{-1})	6.0	6.0	0%	6.2	3%
	c_{20}	3.74	3.8	2%	3.93	5%
	S_{20}	0.68	0.69	0.01	0.70	0.02
	Population (%)	63	63~62 (<= 1%)			
	R^{c} (10^{7} s^{-1})	0.2	0.2	0%	0.2	0%

72R1 at 2°C in water solution

9 + 95 + 170 + 240 GHz

		Table 2-2	Initial Value = Table 2-2 – 10%		Initial Value = Table 2-2 + 10%	
			Best Fit	Error	Best Fit	Error
Comp 2	$R^{o}\perp$ (10^{7} s^{-1})	40.7	38.0	7%	38.9	4%
	c_{20}	3.49	3.41	2%	3.47	1%
	S_{20}	0.59	0.57	0.02	0.58	0.01
	Population (%)	38	37~43 (<= 5%)			
Comp 1	$R^{o}\perp$ (10^{7} s^{-1})	4.0	4.2	4%	4.2	4%
	c_{20}	3.3	3.2	3%	3.37	2%
	S_{20}	0.64	0.63	0.01	0.65	0.01
	Population (%)	32	29~34 (<= 3%)			
Comp 3	$R^{o}\perp$ (10^{7} s^{-1})	49.0	51.3	5%	52.5	7%
	c_{20}	3.21	3.2	0%	3.2	0%
	S_{20}	0.43	0.43	0	0.43	0
	Population (%)	30	28~30 (<= 2%)			
	R^{c} (10^{7} s^{-1})	0.68	0.68	0%	0.66	3%

Appendix III. $\sigma_{9\,GHz} / \sigma_j$ in Equation (2) of Chapter 2

Mutant Site	Spin Label	Ficoll Conc. (w/v %)	Temp. (^oC)	$\sigma_{9\,GHz} / \sigma_j$			
				9 GHz	95 GHz	170 GHz	240 GHz
72	R1	0	32	1	5	44	86
			22	1	4	42	57
			12	1	5	35	50
			2	1	7	40	61
131	R1	0	32	1	17	79	225
			22	1	5	54	96
			12	1	10	48	76
			2	1	9	44	61
72	R2	0	32	1	4	31	---
			22	1	5	40	---
			12	1	7	25	---
			2	1	6	23	---
131	R2	0	32	1	16	48	100
			22	1	8	32	86
			12	1	5	28	61
			2	1	5	30	36
131	R1	25	32	1	---	---	207
			22	1	---	---	118
			12	1	---	---	136
			2	1	---	---	82
72	R2	15	32	1	12	65	---
			22	1	10	40	---
			12	1	12	37	---
			2	1	15	44	---

72	R2	25	32	1	9	67	---
			22	1	10	40	---
			12	1	15	63	---
			2	1	17	67	---
131	R2	15	32	1	6	33	---
			22	1	10	50	---
			12	1	12	44	---
			2	1	18	73	---
131	R2	25	32	1	8	65	121
			22	1	10	72	93
			12	1	10	58	75
			2	1	12	49	50

Appendix IV. Experimental Parameters

Microwave Frequency (GHz)	Modulation Amplitude (Gauss)	Microwave Power (mW)	Time Constant (ms)	Sweep Rate (G/s)	Time Per Point (ms)
9	1.0	1.0	160	---	80
95	4.6	1.0 V [a] (0 V at full power)	30	---	30
170	8.8	18.4 [b]	300	3.3	300
240	9.0	17.4 [b]	300	3.3	210

[a] The microwave power at 95 GHz is not measured by a power meter, thus only the attenuator setting is given here.

[b] The microwave power at 170 and 240 GHz is measured by a power meter, and the attenuator settings are 2.8 and 2.0 respectively at 170 and 240 GHz.

REFERENCES

1. Hubbell, W. L., Mchaourab, H. S., Altenbach, C., and Lietzow, M. A. (1996) Watching Proteins Move using Site-Directed Spin Labeling. *Structure. 4*, 779-783.

2. Hubbell, W. L., Gross, A., Langen, R., and Lietzow, M. A. (1998) Recent Advances in Site-Directed Spin Labeling of Proteins. *Curr. Opin. Struct. Biol. 8*, 649-656.

3. Hubbell, W. L., Cafiso, D. S., and Altenbach, C. (2000) Identifying Conformational Changes with Site-Directed Spin Labeling. *Nat. Struct. Biol. 7*, 735-739.

4. Borbat, P. P., Costa-Filho, A. J., Earle, K. A., Moscicki, J. K., and Freed, J. H. (2001) Electron Spin Resonance in Studies of Membranes and Proteins. *Science. 291*, 266-269.

5. Fanucci, G. E., and Cafiso, D. S. (2006) Recent Advances and Applications of Site-Directed Spin Labeling. *Curr. Opin. Struct. Biol. 16*, 644-653.

6. Barnes, J. P., Liang, Z., Mchaourab, H. S., Freed, J. H., and Hubbell, W. L. (1999) A Multifrequency Electron Spin Resonance Study of T4 Lysozyme Dynamics. *Biophys. J. 76*, 3298-3306.

7. Columbus, L., and Hubbell, W. L. (2002) A New Spin on Protein Dynamics. *Trends in Biochemical Sciences. 27*, 288-295.

8. Schneider, D. J., and Freed, J. H. (1989) Molecular Dynamics and Spin Relaxation. *Adv. Chem. Phys. 73*, 387-527.

9. Guo, Z. (2003) *Ph.D. Thesis.* University of California, Los Angeles, CA.

10. Mchaourab, H. S., Lietzow, M. A., Hideg, K., and Hubbell, W. L. (1996) Motion of Spin-Labeled Side Chains in T4 Lysozyme. Correlation with Protein Structure and Dynamics. *Biochemistry. 35*, 7692-7704.

11. Isas, J. M., Langen, R., Haigler, H. T., and Hubbell, W. L. (2002) Structure and Dynamics of a Helical Hairpin and Loop Region in Annexin 12: A Site-Directed Spin Labeling Study. *Biochemistry. 41*, 1464-1473.

12. Lietzow, M. A., and Hubbell, W. L. (2004) Motion of Spin Label Side Chains in Cellular Retinol-Binding Protein: Correlation with Structure and Nearest-Neighbor Interactions in an Antiparallel Beta-Sheet. *Biochemistry. 43*, 3137-3151.

13. Hoofnagle, A. N., Stoner, J. W., Lee, T., Eaton, S. S., and Ahn, N. G. (2004) Phosphorylation-Dependent Changes in Structure and Dynamics in ERK2 Detected by SDSL and EPR. *Biophys. J. 86*, 395-403.

14. Taylor, J. C., and Markham, G. D. (2003) Conformational Dynamics of the Active Site Loop of S-Adenosylmethionine Synthetase Illuminated by Site-Directed Spin Labeling. *Arch. Biochem. Biophys. 415*, 164-171.

15. Weaver, L. H., and Matthews, B. W. (1987) Structure of Bacteriophage T4 Lysozyme Refined at 1.7 A Resolution. *J. Mol. Biol. 193*, 189-199.

16. Mchaourab, H. S., Oh, K. J., Fang, C. J., and Hubbell, W. L. (1997) Conformation of T4 Lysozyme in Solution. Hinge-Bending Motion and the Substrate-Induced Conformational Transition Studied by Site-Directed Spin Labeling. *Biochemistry. 36*, 307-316.

17. Nelson, W. D., Blakely, S. E., Nesmelov, Y. E., and Thomas, D. D. (2005) Site-Directed Spin Labeling Reveals a Conformational Switch in the Phosphorylation Domain of Smooth Muscle Myosin. *Proc. Natl. Acad. Sci. U. S. A. 102*, 4000-4005.

18. Alonso, A., dos Santos, W. P., Leonor, S., dos Santos, J. G., and Tabak, M. (2001) Stratum Corneum Protein Dynamics as Evaluated by a Spin-Label Maleimide Derivative: Effect of Urea. *Biophys. J. 81*, 3566-3576.

19. Karplus, M., and Pettitt, B. M. (1988) Proteins: A Theoretical Perspective of Dynamics, Structure, and Thermodynamics.

20. Kay, L. E. (1998) Protein Dynamics from NMR. *Nat. Struct. Biol. 5*, 513-517.

21. Ishima, R., and Torchia, D. A. (2000) Protein Dynamics from NMR. *Nat. Struct. Biol. 7*, 740-743.

22. Mittermaier, A., and Kay, L. E. (2006) New Tools Provide New Insights in NMR Studies of Protein Dynamics. *Science. 312*, 224-228.

23. Dalton, L. In *EPR and Advanced EPR Studies of Biological Systems*; Dalton, L., Ed.; CRC Press: Boca Raton, FL, 1985; Chapter 1, pp 1-10.

24. Berliner, L. J. Spin Labeling: the Next Millenium. In *Biological Magnetic Resonance*; Berliner, L. J., Ed.; Plenum: New York, 1998; Vol.14.

25. Budil, D. E., Earle, K. A., and Freed, J. H. (1993) Full Determination of the Rotational Diffusion Tensor by Electron Paramagnetic Resonance at 250 GHz. *J. Phys. Chem. 97*, 1294-1303.

26. Liang, Z., and Freed, J. H. (1999) An Assessment of the Applicability of Multifrequency ESR to Study the Complex Dynamics of Biomolecules. *The Journal of Physical Chemistry B. 103*, 6384-6396.

27. Poluektov, O. G., Utschig, L. M., Dalosto, S., and Thurnauer, M. C. (2003) Probing Local Dynamics of the Photosynthetic Bacterial Reaction Center with a Cysteine Specific Spin Label. *The Journal of Physical Chemistry B. 107*, 6239-6244.

28. Liang, Z., Lou, Y., Freed, J. H., Columbus, L., and Hubbell, W. L. (2004) A Multifrequency Electron Spin Resonance Study of T4 Lysozyme Dynamics using the Slowly Relaxing Local Structure Model. *The Journal of Physical Chemistry B. 108*, 17649-17659.

29. White, G. F., Ottignon, L., Georgiou, T., Kleanthous, C., Moore, G. R., Thomson, A. J., and Oganesyan, V. S. (2007) Analysis of Nitroxide Spin Label Motion in a Protein-Protein Complex using Multiple Frequency EPR Spectroscopy. *J. Magn. Reson. 185*, 191-203.

30. Savitsky, A., Kuhn, M., Duche, D., Mobius, K., and Steinhoff, H. (2004) Spontaneous Refolding of the Pore-Forming Colicin A Toxin upon Membrane Association as Studied by X-Band and W-Band High-Field Electron Paramagnetic Resonance Spectroscopy. *The Journal of Physical Chemistry B. 108*, 9541-9548.

31. Mobius, K., Savitsky, A., Wegener, C., Plato, M., Fuchs, M., Schnegg, A., Dubinskii, A. A., Grishin, Y. A., Grigor'ev, I. A., Kuhn, M., Duche, D., Zimmermann, H., and Steinhoff, H. J. (2005) Combining High-Field EPR with Site-Directed Spin Labeling Reveals Unique Information on Proteins in Action. *Magn. Reson. Chem. 43*, S4-S19.

32. Bagryanskaya, E. G., Polovyanenko, D. N., Fedin, M. V., Kulik, L., Schnegg, A., Savitsky, A., Mobius, K., Coleman, A. W., Ananchenko, G. S., and Ripmeester, J. A. (2009) Multifrequency EPR Study of the Mobility of Nitroxides in Solid-State Calixarene Nanocapsules. *Phys. Chem. Chem. Phys. 11*, 6700-6707.

33. Freed, J. H. (2000) New Technologies in Electron Spin Resonance. *Annu. Rev. Phys. Chem. 51*, 655-689.

34. Columbus, L., Kalai, T., Jeko, J., Hideg, K., and Hubbell, W. L. (2001) Molecular Motion of Spin Labeled Side Chains in Alpha-Helices: Analysis by Variation of Side Chain Structure. *Biochemistry. 40*, 3828-3846.

35. Langen, R., Oh, K. J., Cascio, D., and Hubbell, W. L. (2000) Crystal Structures of Spin Labeled T4 Lysozyme Mutants: Implications for the Interpretation of EPR Spectra in Terms of Structure. *Biochemistry. 39*, 8396-8405.

36. Berlinear, L. J. (1976) Spin Labeling: Theory and Applications.

37. Fleissner, M. R. (2007) *Ph.D. Thesis.* University of California, Los Angeles, CA.

38. Polimeno, A., and Freed, J. H. (1995) Slow Motional ESR in Complex Fluids: The Slowly Relaxing Local Structure Model of Solvent Cage Effects. *J. Phys. Chem. 99*, 10995-11006.

39. Liang, Z., Freed, J. H., Keyes, R. S., and Bobst, A. M. (2000) An Electron Spin Resonance Study of DNA Dynamics using the Slowly Relaxing Local Structure Model. *The Journal of Physical Chemistry B. 104*, 5372-5381.

40. McConnell, H. M., and McFarland, B. G. (1970) Physics and Chemistry of Spin Labels. *Quart. Rev. Biophys. 3*, 91-136.

41. Snipes, W., Cupp, J., Cohn, G., and Keith, A. (1974) Electron Spin Resonance Analysis of the Nitroxide Spin Label 2,2,6,6-Tetramethylpiperidone-N-Oxyl (Tempone) in Single Crystals of the Reduced Tempone Matrix. *Biophys. J. 14*, 20-32.

42. Lipari, G., and Szabo, A. (1982) Model-Free Approach to the Interpretation of Nuclear Magnetic Resonance Relaxation in Macromolecules. 1. Theory and Range of Validity. *J. Am. Chem. Soc. 104*, 4546-4559.

43. Lipari, G., and Szabo, A. (1982) Model-Free Approach to the Interpretation of Nuclear Magnetic Resonance Relaxation in Macromolecules. 2. Analysis of Experimental Results. *J. Am. Chem. Soc. 104*, 4559-4570.

44. Clore, G. M., Szabo, A., Bax, A., Kay, L. E., Driscoll, P. C., and Gronenborn, A. M. (1990) Deviations from the Simple Two-Parameter Model-Free Approach to the Interpretation of Nitrogen-15 Nuclear Magnetic Relaxation of Proteins. *J. Am. Chem. Soc. 112*, 4989-4991.

45. Meirovitch, E., Shapiro, Y. E., Polimeno, A., and Freed, J. H. (2006) Protein Dynamics from NMR: The Slowly Relaxing Local Structure Analysis Compared with Model-Free Analysis. *J. Phys. Chem. A. 110*, 8366-8396.

46. Tugarinov, V., Liang, Z., Shapiro, Y. E., Freed, J. H., and Meirovitch, E. (2001) A Structural Mode-Coupling Approach to 15N NMR Relaxation in Proteins. *J. Am. Chem. Soc. 123*, 3055-3063.

47. Meirovitch, E., Shapiro, Y. E., Polimeno, A., and Freed, J. H. (2009) Structural Dynamics of Bio-Macromolecules by NMR: The Slowly Relaxing Local Structure Approach. *Submitted for Publication.*

48. Freed, J. H. (1977) Stochastic-Molecular Theory of Spin--Relaxation for Liquid Crystals. *J. Chem. Phys. 66*, 4183-4199.

49. Meirovitch, E., Nayeem, A., and Freed, J. H. (1984) Analysis of Protein-Lipid Interactions Based on Model Simulations of Electron Spin Resonance Spectra. *J. Phys. Chem. 88*, 3454-3465.

50. Emrich, J., and Streisinger, G. (1968) The Role of Phage Lysozyme in the Life Cycle of Phage T4. *Virology. 36*, 387-391.

51. Mirelman, D., Kleppe, G., and Jensen, H. B. (1975) Studies on the Specificity of Action of Bacteriophage T4 Lysozyme. *Eur. J. Biochem. 55*, 369-373.

52. Mirelman, D., Kleppe, G., Jensen, H. B., and Schindler, M. (1976) The Specificity Requirements of Bacteriophage T4 Lysozyme. *Eur. J. Biochem. 66*, 319-325.

53. Anderson, W. F., Grutter, M. G., Remington, S. J., Weaver, L. H., and Matthews, B. W. (1981) Crystallographic Determination of the Mode of Binding of Oligosaccharides to T4 Bacteriophage Lysozyme: Implications for the Mechanism of Catalysis. *J. Mol. Biol. 147*, 523-543.

54. Fischer, M. W., Majumdar, A., Dahlquist, F. W., and Zuiderweg, E. R. (1995) 15N, 13C, and 1H NMR Assignments and Secondary Structure for T4-Lysozyme. *J. Magn. Reson. B. 108*, 143-154.

55. Remington, S. J., Anderson, W. F., Owen, J., Ten Eyck, L. F., Grainger, C. T., and Matthews, B. W. (1978) Structure of the Lysozyme from Bacteriophage T4: An Electron Density Map at 2.4 A Resolution. *J. Mol. Biol. 118*, 81-98.

56. Matthews, B. W., and Remington, S. J. (1974) The Three Dimensional Structure of the Lysozyme from Bacteriophage T4. *Proc. Natl. Acad. Sci. 71*, 4178-4182.

57. de Groot, B. L., Hayward, S., van Aalten, D. M., Amadei, A., and Berendsen, H. J. (1998) Domain Motions in Bacteriophage T4 Lysozyme: A Comparison between Molecular Dynamics and Crystallographic Data. *Proteins. 31*, 116-127.

58. Faber, H. R., and Matthews, B. W. (1990) A Mutant T4 Lysozyme Displays Five Different Crystal Conformations. *Nature. 348*, 263-266.

59. Mulder, F. A., Hon, B., Mittermaier, A., Dahlquist, F. W., and Kay, L. E. (2002) Slow Internal Dynamics in Proteins: Application of NMR Relaxation Dispersion Spectroscopy to Methyl Groups in a Cavity Mutant of T4 Lysozyme. *J. Am. Chem. Soc. 124*, 1443-1451.

60. Columbus, L., and Hubbell, W. L. (2004) Mapping Backbone Dynamics in Solution with Site-Directed Spin Labeling: GCN4-58 bZip Free and Bound to DNA. *Biochemistry. 43*, 7273-7287.

61. Lopez, C. J., Fleissner, M. R., Guo, Z., Kusnetzow, A. K., and Hubbell, W. L. (2009) Osmolyte Perturbation Reveals Conformational Equilibria in Spin-Labeled Proteins. *Protein Sci. 18*, 1637-1652.

62. Hofbauer, W., Earle, K. A., Dunnam, C. R., Moscicki, J. K., and Freed, J. H. (2004) A High-Power 95 GHz Pulsed Electron Spin Resonance Spectrometer. *Rev. Sci. Instrum. 75*, 1194-1208.

63. Earle, K. A., Dzikovski, B., Hofbauer, W., Moscicki, J. K., and Freed, J. H. (2005) High-Frequency ESR at ACERT. *Magn. Reson. Chem. 43*, S256-66.

64. Mchaourab, H. S., Kalai, T., Hideg, K., and Hubbell, W. L. (1999) Motion of Spin-Labeled Side Chains in T4 Lysozyme: Effect of Side Chain Structure. *Biochemistry. 38*, 2947-2955.

65. Jacobsen, K., Oga, S., Hubbell, W. L., and Risse, T. (2005) Determination of the Orientation of T4 Lysozyme Vectorially Bound to a Planar-Supported Lipid Bilayer using Site-Directed Spin Labeling. *Biophys. J. 88*, 4351-4365.

66. Budil, D. E., Sale, K. L., Khairy, K. A., and Fajer, P. G. (2006) Calculating Slow-Motional Electron Paramagnetic Resonance Spectra from Molecular Dynamics using a Diffusion Operator Approach. *J. Phys. Chem. A. 110*, 3703-3713.

67. Tombolato, F., Ferrarini, A., and Freed, J. H. (2006) Modeling the Effects of Structure and Dynamics of the Nitroxide Side Chain on the ESR Spectra of Spin-Labeled Proteins. *J. Phys. Chem. B. 110*, 26260-26271.

68. Sezer, D., Freed, J. H., and Roux, B. (2009) Multifrequency Electron Spin Resonance Spectra of a Spin-Labeled Protein Calculated from Molecular Dynamics Simulations. *J. Am. Chem. Soc. 131*, 2597-2605.

69. Barnes, J. P., and Freed, J. H. (1997) Aqueous Sample Holders for High Frequency Electron Spin Resonance. *Rev. Sci. Instrum. 68*, 2838-2846.

70. Earle, K. A., Budil, D. E., and Freed, J. H. (1993) 250-GHz EPR of Nitroxides in the Slow-Motional Regime: Models of Rotational Diffusion. *J. Phys. Chem. 97*, 13289-13297.

71. Earle, K. A., Moscicki, J. K., Ge, M., Budil, D. E., and Freed, J. H. (1994) 250-GHz Electron Spin Resonance Studies of Polarity Gradients Along the Aliphatic Chains in Phospholipid Membranes. *Biophys. J. 66*, 1213-1221.

72. Budil, D. E.; Earle, K. A.; Lynch, W. B.; Freed, J. H. Electron Paramagnetic Resonance at 1 millimeter Wavelengths. In *Advanced EPR: Applications in Biology and Biochemistry*; Hoff, A., Ed.; Elsevier: Amsterdam, 1989; Chapter 8, pp 307-340.

73. Budil, D. E., Lee, S., Saxena, S., and Freed, J. H. (1996) Nonlinear-Least-Squares Analysis of Slow-Motion EPR Spectra in One and Two Dimensions using a Modified Levenberg-Marquardt Algorithm. *J. Magn. Reson. , Series A. 120*, 155-189.

74. Ge, M., and Freed, J. H. (1993) An Electron Spin Resonance Study of Interactions between Gramicidin A' and Phosphatidylcholine Bilayers. *Biophys. J. 65*, 2106-2123.

75. Mulder, F. A., Mittermaier, A., Hon, B., Dahlquist, F. W., and Kay, L. E. (2001) Studying Excited States of Proteins by NMR Spectroscopy. *Nat. Struct. Biol. 8*, 932-935.

76. Guo, Z., Cascio, D., Hideg, K., and Hubbell, W. L. (2008) Structural Determinants of Nitroxide Motion in Spin-Labeled Proteins: Solvent-Exposed Sites in Helix B of T4 Lysozyme. *Protein Sci. 17*, 228-239.

77. Sezer, D., Freed, J. H., and Roux, B. (2008) Parametrization, Molecular Dynamics Simulation, and Calculation of Electron Spin Resonance Spectra of a Nitroxide Spin Label on a Polyalanine Alpha-Helix. *J. Phys. Chem. B. 112*, 5755-5767.

78. Sezer, D., Freed, J. H., and Roux, B. (2008) Using Markov Models to Simulate Electron Spin Resonance Spectra from Molecular Dynamics Trajectories. *J. Phys. Chem. B. 112*, 11014-11027.

79. Sezer, D., Freed, J. H., and Roux, B. (2008) Simulating Electron Spin Resonance Spectra of Nitroxide Spin Labels from Molecular Dynamics and Stochastic Trajectories. *J. Chem. Phys. 128*, 165106.

80. Dzikovski, B., Tipikin, D., Livshits, V., Earle, K., and Freed, J. (2009) Multifrequency ESR Study of Spin-Labeled Molecules in Inclusion Compounds with Cyclodextrins. *Phys. Chem. Chem. Phys. 11*, 6676-6688.

81. Fleissner, M. R., Cascio, D., and Hubbell, W. L. (2009) Structural Origin of Weakly Ordered Nitroxide Motion in Spin-Labeled Proteins. *Protein Sci. 18*, 893-908.

82. Lavalette, D., Tetreau, C., Tourbez, M., and Blouquit, Y. (1999) Microscopic Viscosity and Rotational Diffusion of Proteins in a Macromolecular Environment. *Biophys. J. 76*, 2744-2751.

83. Timofeev, V. P., and Tsetlin, V. I. (1983) Analysis of Mobility of Protein Side Chains by Spin Label Technique. *European Biophysics Journal. 10*, 93-108.

84. Banks, D. S., and Fradin, C. (2005) Anomalous Diffusion of Proteins due to Molecular Crowding. *Biophys. J. 89*, 2960-2971.

85. Charlton, L. M., Barnes, C. O., Li, C., Orans, J., Young, G. B., and Pielak, G. J. (2008) Residue-Level Interrogation of Macromolecular Crowding Effects on Protein Stability. *J. Am. Chem. Soc. 130*, 6826-6830.

86. Minton, A. P. (2005) Models for Excluded Volume Interaction between an Unfolded Protein and Rigid Macromolecular Cosolutes: Macromolecular Crowding and Protein Stability Revisited. *Biophys. J. 88*, 971-985.

87. Ping, G., Yuan, J. M., Sun, Z., and Wei, Y. (2004) Studies of Effects of Macromolecular Crowding and Confinement on Protein Folding and Protein Stability. *J. Mol. Recognit. 17*, 433-440.

88. Ellis, R. J. (2001) Macromolecular Crowding: An Important but Neglected Aspect of the Intracellular Environment. *Curr. Opin. Struct. Biol. 11*, 114-119.

89. Elcock, A. H. (2003) Atomic-Level Observation of Macromolecular Crowding Effects: Escape of a Protein from the GroEL Cage. *Proc. Natl. Acad. Sci. 100*, 2340-2344.

90. Monterroso, B., and Minton, A. P. (2007) Effects of High Concentration of Inert Cosolutes on the Refolding of an Enzyme. *The Journal of Biological Chemistry. 282*, 33452-33458.

91. Wenner, J. R., and Bloomfield, V. A. (1999) Crowding Effects on EcoRV Kinetics and Binding. *Biophys. J. 77*, 3234-3241.

92. Faber, H. R., and Matthews, B. W. (1990) A Mutant T4 Lysozyme Displays Five Different Crystal Conformations. *Nature. 348*, 263-266.

93. Goto, N. K., Skrynnikov, N. R., Dahlquist, F. W., and Kay, L. E. (2001) What is the Average Conformation of Bacteriophage T4 Lysozyme in Solution? A Domain Orientation Study using Dipolar Couplings Measured by Solution NMR. *J. Mol. Biol. 308*, 745-764.

94. Lopez, C. J., Fleissner, M. R., and Hubbell, W. L. (2009) *Unpublished Work.*

95. Cellitti, J., Llinas, M., Echols, N., Shank, E. A., Gillespie, B., Kwon, E., Crowder, S. M., Dahlquist, F. W., Alber, T., and Marqusee, S. (2007) Exploring Subdomain Cooperativity in T4 Lysozyme I: Structural and Energetic Studies of a Circular Permutant and Protein Fragment. *Protein Sci. 16*, 842-851.

96. Fleissner, M. R., Altenbach, C., and Hubbell, W. L. (2009) *Unpublished Work.*

97. Stagg, L., Zhang, S. Q., Cheung, M. S., and Wittung-Stafshede, P. (2007) Molecular Crowding Enhances Native Structure and Stability of alpha/beta Protein Flavodoxin. *Proc. Natl. Acad. Sci. 104*, 18976-18981.

98. Earle, K. A., Mainalli, L., Sahu, I. D., and Schneider, D. J. (2009) Magnetic Resonance Spectra and Statistical Geometry. *Appl. Magn. Reson. in press*.

99. Ablett, S., Izzard, M. J., and Lillford, P. J. (1992) Differential Scanning Calorimetric Study of Frozen Sucrose and Glycerol Solutions. *J. Chem. Soc. Faraday Trans. 88*, 789-794.

100. Roozen, M. J. G. W., and Hemminga, M. A. (1990) Molecular Motion in Sucrose-Water Mixtures in the Liquid and Glassy State as Studied by Spin Probe ESR. *J. Phys. Chem. 94*, 7326-7329.

101. Savitsky, A., Dubinskii, A. A., Plato, M., Grishin, Y. A., Zimmermann, H., and Mobius, K. (2008) High-Field EPR and ESEEM Investigation of the Nitrogen Quadrupole Interaction of Nitroxide Spin Labels in Disordered Solids: Toward Differentiation between Polarity and Proticity Matrix Effects on Protein Function. *J. Phys. Chem. B. 112*, 9079-9090.

102. Ondar, M. A., Grinberg, O. Y., Dubinskii, A. A., and Lebedev, Y. S. (1985) Study of the Effect of the Medium on the Magnetic-Resonance Parameters of Nitroxyl Radicals by High-Resolution EPR Spectroscopy. *Sov. J. Chem. Phys. 3*, 781-792.

103. Hopkinson, J. M. (1997) *Ph.D. Thesis.* Cornell University, Ithaca, NY.